DESIGN AND GRAYSCALE FABRICATION OF BEAMFANNERS IN A SILICON SUBSTRATE

by

ARTHUR C. ELLIS

A DISSERTATION

Submitted in partial fulfillment of the requirements
for the degree of Doctor of Philosophy in
The Department of Physics
of
The School of Graduate Studies
of
The University of Alabama in Huntsville

HUNTSVILLE, ALABAMA

2001

Copyright by

Arthur C. Ellis

All Rights Reserved

2001

DISSERTATION APPROVAL FORM

Submitted by Arthur C. Ellis in partial fulfillment of the requirements for the degree of Doctor of Philosophy in Physics.

Accepted on behalf of the Faculty of the School of Graduate Studies by the dissertation committee:

____________________________ Committee Chair

____

____

____

____

____

____________________________ Department Chair

____________________________ College Dean

____________________________ Graduate Dean

ABSTRACT
School of Graduate Studies
The University of Alabama in Huntsville

Degree Doctor of Philosophy College/Dept Science/Physics

Name of Candidate Arthur C. Ellis

Title Design and Grayscale Fabrication of Beamfanners in a Silicon Substrate

This dissertation addresses important first steps in the development of a grayscale fabrication process for multiple phase diffractive optical elements (DOE's) in silicon. Specifically, this process was developed through the design, fabrication, and testing of 1-2 and 1-4 beamfanner arrays for 5-micron illumination. The 1-2 beamfanner arrays serve as a test-of-concept and basic developmental step toward the construction of the 1-4 beamfanners.

The beamfanners are 50 microns wide, and have features with dimensions of between 2 and 10 microns. The Iterative Angular Spectrum Approach (IASA) method, developed by Steve Mellin of UAH, and the Boundary Element Method (BEM) are the design and testing tools used to create the beamfanner profiles and predict their performance.

Fabrication of the beamfanners required the techniques of grayscale photolithography and reactive ion etching (RIE). A 2-3-micron feature size 1-4 silicon beamfanner array was fabricated, but the small features and contact photolithographic techniques available prevented its construction to specifications. A second and more successful attempt was made in which both 1-4 and 1-2 beamfanner arrays were fabricated with a 5-micron minimum feature size. Photolithography for the UAH array was contracted to MEMS-Optical of Huntsville, Alabama.

A repeatability study was performed, using statistical techniques, of 14 photoresist arrays and the subsequent RIE process used to etch the arrays in silicon. The variance in selectivity between the 14 processes was far greater than the variance between the individual etched features within each process. Specifically, the ratio of the variance of the selectivities averaged over each of the 14 etch processes to the variance of individual feature selectivities within the processes yielded a significance level below 0.1% by F-test, indicating that good etch-to-etch process repeatability was not attained.

One of the 14 arrays had feature etch-depths close enough to design specifications for optical testing, but 5-micron IR illumination of the 1-4 and 1-2 beamfanners yielded no convincing results of beam splitting in the detector plane 340 microns from the surface of the beamfanner array.

Abstract Approval: Committee Chair ____________________________________

(Date)

Department Chair ____________________________________

Graduate Dean ____________________________________

ACKNOWLEDGMENTS

I would like to thank Dr. Stephen Mellin for his invaluable assistance in the design work for this research. I would also like to thank Dr. Greg Nordin and the UAH diffractive optics group for help and encouragement along the way.

TABLE OF CONTENTS

Page

LIST OF FIGURES...ix

LIST OF TABLES xiv

LIST OF SYMBOLS xv

Chapter 1 INTRODUCTION 1

1.1 IR camera focal plane array 2

1.2 Focus...4

1.3 Organization of Dissertation…………………………………………………………..….5

Chapter 2 BACKGROUND OF GRAYSCALE FABRICATION TECHNIQUES 7

2.1 Grayscale photolithograpy (motivation)…………………………………………………7

2.2 Grayscale mask techniques……………………………………………………………….9

2.3 Direct writing techniques………………………………………………………………11

Chapter 3 MODELLING AND DESIGN OF BEAMFANNER ARRAY AND TEST

ARRAYS...12

3.1 The Iterative Angular Spectrum Algorithm (IASA)……………………………………....12

3.2 The Boundary Element Method (BEM)…………………………………………………...15

3.2.1 Derivation of rigorous boundary integral diffraction theory…………………………16

3.2.2 Application of rigorous diffraction theory to BEM computational procedure…..……32

3.3 Design and positioning of the Nichols and UAH arrays………………………………… 36

3.3.1 Nichols beamfanner array description………………………………………………..42

3.3.2 UAH beamfanner array description…………………………………………………..44

3.4 BEM performance simulation of beamfanners…………………………………………48

3.4.1 Analysis of 1-2 beamfanner irradiance as a function of detector plane position…….48

3.4.2 Diffraction efficiency and signal-to-noise ratio of 1-2 beamfanner irradiance………69

Chapter 4 FABRICATION OF NICHOLS AND UAH BEAMFANNER ARRAYS…………...73
4.1 Development of 2-3-micron lateral feature size beamfanner array fabrication procedure...74
4.1.1 General micro-fabrication procedures……………………………………………...74
4.1.1.1 Photolithography……………………………………………………………74
4.1.1.2 Silicon etch……………………………………………………………………76
4.1.2 Etch selectivity calibration……………………………………………………………78
4.1.3 Resultant fabrication of beamfanner array with 2-3-micron feature sizes……………81
4.1.4 Lessons learned from the first attempt……………………………………………. 83
4.2 Fabrication of UAH array……………………………………………………………………85
4.2.1 MEMS-Optical grayscale photolithography…………………………………………86
4.2.2 UAH array RIE etch…………………………………………………………………..93
Chapter 5 ANALYSIS OF ETCH SELECTIVITY AND REPEATABILITY 94
5.1 Photolithography/etch/selectivity analysis……………………………………………...97
5.2 Process repeatability and trends based on analysis of selectivity as a function of etch process and individual feature attributes…………………………………………………..101
Chapter 6 TESTING OF DEVICES...113
6.1 Alignment procedure for finite apertures and MEMS-Optical photolithography………..113
6.2 IR microscopy testing of the 1-4 beamfanner arrays (Nichols Research)………..……...117
6.3 Comparison of observed beamfanner performance with prediced (BEM) performance for the 1-2 beamfanner arrays………………………………………………………………118
6.4 Fabrication of the integrated focal plane array…………………………………………...121
Chapter 7 CONCLUSION. 123
Appendix A: DOE Fabrication and BEM Analysis Codes….……………………………......125
Appendix B: Statistical Analysis Code used in Chapter 5……………………..……..……...139
REFERENCES..155

LIST OF FIGURES

Figure Page

1.1 Cross-section, top (input), and bottom (output) views of the proposed focal plane array (FPA)……………………………………………………………………………...……………3

2.1 Comparison of binary and grayscale UV resist exposure schemes………………….……….7

2.2 Four gray-level features with rounding of the two highest features…………………...……9

3.1 Equal splitting of amplitude by beamfanners in the detector plane…………………………..14

3.2 Three-dimensional volume and enclosing surface with differential surface area and outward pointing normal vector……………………………………………………………18

3.3 Two-dimensional line integration representing the DOE boundary with a and b as conducting pads defining a finite aperture……………………………………………………22

3.4 Singularities along DOE contour to be integrated……………………………...…………….24

3.5 TE and TM fields at a dielectric interface……………………………………………………27

3.6 Scheme for the spherical illumination of the beamfanner with maximum etch-depth on the incident surface, t, and incident fields sampled over a finite interval, x, with a virtual focus on the focal plane at point P, which is a distance, a, from the incident surface…………………………………………………………………………...…………....38

3.7 Addition of phase levels/etch-depths to fabricate the 1-4 beamfanner from 1-2 beamfanners………………………………………………………………………………..39

3.8 A sixteen lateral feature, 16 phase level DOE, a), is re-sampled, b), to have a selection of 8 phase levels and 4 lateral feature sizes, c). Note that the choice of 4 lateral features reduces the number of available phase levels to 4 in this example…………...……..41

3.9 A view of the Nichols beamfanner array……………………………………...…………...43

3.10 View of the UAH beamfanner array, where scan lengths represent the number of lateral features in the width of a single beamfanner……………………………………...45

3.11 Center-pixel (on-axis) illumination and middle and side-pixel (off-axis) illumination of beamfanner focal plane array……………………………………………………………..47

3.12 One-micron lateral feature size, 256 phase level 1-2 beamfanner (bottom) designed for plane wave illumination with corresponding irradiance pattern in focal plane (top)………………………………………………………………………………………….50

3.13 From top to bottom: irradiance and DOE profile for center, middle, and side pixel 1-2 beamfanners for the 1-micron lateral feature size, 256 phase level case……………….….51

3.14 From top to bottom: irradiance and DOE profile for center, middle, and side pixel 1-2 beamfanners for the 5-micron lateral feature size, 8 phase level case………………….52

3.15 From top to bottom: irradiance and DOE profile for center, middle, and side pixel 1-2 beamfanners for the 5-micron lateral feature size, 16 phase level case……………….…...53

3.16 From top to bottom: irradiance and DOE profile for center, middle, and side pixel 1-2 beamfanners for the 5-micron lateral feature size, 32 phase level case……………….……...54

3.17 From top to bottom: irradiance and DOE profile for center, middle, and side pixel 1-2 beamfanners for the 5-micron lateral feature size, 64 phase level case……………….……...55

3.18 From top to bottom: irradiance and DOE profile for center, middle, and side pixel 1-2 beamfanners for 6-micron lateral feature size, 8 phase level case……………………...56

3.19 From top to bottom: irradiance and DOE profile for center, middle, and side pixel 1-2 beamfanners for 6-micron lateral feature size, 16 phase level case…………………….57

3.20 From top to bottom: irradiance and DOE profile for center, middle, and side pixel 1-2 beamfanners for the 6-micron lateral feature size, 32 phase level case…………...…….58

3.21 From top to bottom: irradiance and DOE profile for center, middle, and side pixel 1-2 beamfanners for 6-micron lateral feature size, 64 phase level case………..………….59

3.22 From top to bottom: irradiance and DOE profile for center, middle, and side pixel 1-2 beamfanners for 7-micron lateral feature size, 8 phase level case……………………..…..60

3.23 From top to bottom: irradiance and DOE profile for center, middle, and side pixel 1-2 beamfanners for 7-micron lateral feature size, 16 phase level case……………………61

3.24 From top to bottom: irradiance and DOE profile for center, middle, and side pixel 1-2 beamfanners for 7-micron lateral feature size, 32 phase level case……………………62

3.25 From top to bottom: irradiance and DOE profile for center, middle, and side pixel 1-2 beamfanners for 7-micron lateral feature size, 64 phase level case…………………..…63

3.26 From top to bottom: irradiance and DOE profile for center, middle, and side pixel 1-2 beamfanners for 10-micron lateral feature size, 8 phase level case……………………64

3.27 From top to bottom: irradiance and DOE profile for center, middle, and side pixel 1-2 beamfanners for 10-micron lateral feature size, 16 phase level case…………………...65

3.28 From top to bottom: irradiance and DOE profile for center, middle, and side pixel 1-2 beamfanners for 10-micron lateral feature size, 32 phase level case…..………..……..66

3.29 From top to bottom: irradiance and DOE profile for the center, middle, and side pixel 1-2 beamfanners for 10-micron lateral feature size, 64 phase level case……….………..67

4.1 Calibration curve submitted to Canyon Materials for the grayscale mask for the Nichols array…………………………………………………………………….………………82

4.2 View of a center-pixel 1-4 beamfanner array with 2-3-micron lateral feature sizes and 256 phase levels in resist (top) and etched in silicon (bottom). Note the blurred features in the resist and the rounded features in the etch which are caused by melted resist features being transferred into the silicon……………………………………………...83

4.3 View of a side-pixel 1-2 beamfanner array with 5-micron lateral feature sizes and 64 phase levels in resist (top) and etched in silicon (bottom)………………………………...88

4.4 View of a corner-pixel 1-4 beamfanner with 5-micron lateral feature sizes and 64 phase levels in resist (top) and etched in silicon (bottom)……………………….………..89

4.5 View of a center-pixel 1-4 beamfanner array with 5-micron lateral feature sizes and 64 phase levels in resist (top) and etched in silicon (bottom)………………………………...90

4.6 View of a side-pixel 1-4 beamfanner array with 5-micron lateral feature sizes and 64 phase levels in resist (top) and etched in silicon (bottom)……………………………..…..91

4.7 View of a middle-pixel 1-4 beamfanner array with 5-micron lateral feature sizes and 64 phase levels in resist (top) and etched in silicon (bottom)……………………………..…..92

5.1 Column of 10-micron lateral feature size 1-2 beamfanners (corresponds to array p5 in Chapter 3, Figure 3.10) measured with a profilometer for each of 14 samples. Profilometry was conducted over cross-sections similar to those shown to the right of the array in the diagram……………………………………………………………...……97

5.2 Plot of residual selectivity error vs. expected selectivity values for the 14 processes………103

5.3 Plot of block residual selectivity error vs. expected selectivity values…………………...…107

5.4 Plot of block residual selectivity error vs. the order in which the processes were performed…………………………………………...…………………………………107

5.5 Plot of block residual selectivity error vs. average feature etch-depth…………...…………108

5.6 Plot of block residual error vs. lateral position on the substrate……………………………109

5.7 Plot of selectivity vs. mean feature etch-depth………………………………...……...….110

5.8 Plot of mean selectivity of each of 40 features vs. lateral position on substrate………...…111

5.9 Profilometer measurement plots of cross-sections of 5 adjacent 1-2 beamfanners for center-pixel (top), middle-pixel (center), and side-pixel (bottom) cases for resist profiles (left column) and etch profiles (right column)……………………………………..112

6.1 Finite aperture masks oriented to an array of 5 adjacent 1-2 beamfanners. A microscope image is shown at the bottom……………………….…………………….....114

6.2 A not-to-scale view of the alignment patterns used to place the finite apertures on the beamfanner array. The Aligncross pattern also aligns to the back-side of the integrated wave plate-polarizer array……………………………………………………….….116

6.3 Configuration for optical testing of 1-4 beamfanners. The lens system the for 1-4 beamfanner illumination was provided by Nichols/CSC.……….…………………...117

6.4 A drawing of the diffraction pattern of a 1-4 beamfanner…………………………………..118

6.5 Optical testing scheme for the 1-2 beamfanners……………………………………………119

6.6 Sub-micron pitting in silicon surface of 1-4 beamfanners…………………………………..120

6.7 Simulated performance of on-axis 1-2 beamfanner with roughness and sidewall rounding…………………………………………………………………………….….121

LIST OF TABLES

Table Page

3.1 Diffraction efficiency of individual 1-2 beamfanners……………………………………..……...70

3.2 Signal-to-noise ratio of individual 1-2 beamfanners…………………………….…………..71

5.1 Center-Pixel Data……………………………………………………………………...…98

5.2 Middle-Pixel Data…………………………………………………...………..………99

5.3 Side-Pixel Data………………………………………………...………..………..……100

LIST OF SYMBOLS

Symbol	Definition
$\vec{A}$	Vector potential (Tesla meters)
$\vec{B}$	Magnetic flux density (Tesla)
c	Free space speed of light (3 x 10^8 meters/second)
$\vec{D}$	Electric displacement (Coulombs/m^2)
$\vec{E}$	Electric Field (Volts/meter)
G	Green's function
$\vec{H}$	Magnetic Field (Amperes/meter)
$\vec{J}$	Electric current density (Amperes/m^2)
$\vec{k}$	Wavevector (m^{-1})
$\hat{n}$	Unit normal vector
$\vec{r}$, $\vec{r}\,'$	Position vectors (m)
$\vec{S}$	Complex Poynting vector (Watts/m^2)
Y	BEM Admittance matrix ($ohms^{-1}$)
Z	BEM Impedance matrix (ohms)
x, y, z	Spatial coordinates (m)
ε	Electric permittivity (Farads/meter)
η_0	Impedance in free space (376.7 ohms)
μ	Magnetic permeability (Henrys/meter)
ρ	Electric volume charge density (Coulombs/m^3)

τ	Fresnel transmission coefficient
ω	Angular frequency of light (s^{-1})

Chapter 1

INTRODUCTION

This dissertation documents the design, grayscale fabrication, and optical testing of both 1-2 and 1-4 beamfanner micro-arrays in a silicon substrate. Originally, the 1-4 beamfanners were intended for use in a focal plane array that was to be part of a real time imaging polarimeter developed by Nichols Research Corporation, now a branch of Computer Sciences Corporation, in Huntsville, Alabama. This did not work out, since the 2-3-micron feature sizes specified by the design proved too difficult to fabricate. However, the beamfanner development at the University of Alabama in Huntsville continued. New designs with feature sizes 5 microns and larger were introduced. An emphasis was placed on developing silicon beamfanners that could be tested against predicted performance by rigorous diffraction techniques and produced with a high degree of process repeatability in the UAH micro-fabrication facility.

First presented below, in Section 1.1, is a description of the Nichols focal plane array and how the 1-4 beamfanner array fits into its design. The Nichols project was the initial motivation for this dissertation, but, as stated before, could not be successfully fabricated. This section is important, however, in that it defines the original purpose for the 1-4 beamfanners. Section 1.2 introduces the general research focus of beamfanner development.

1.1 IR camera focal plane array

The work done for Nichols Research Corporation consists of the attempted design, fabrication, and testing of a 256×256 array of 50-micron square 1-4 beamfanners etched in silicon. The beamfanner array is the first component in a focal plane element for an infrared camera that functions as a real-time imaging polarimeter in the 3.5-5-micron range. Figure 1.1 shows, in descending order, a cross-section, top, and bottom view of this focal plane element. Each beamfanner takes a beam of infrared light from an image point and splits it into four beams. Each beam is then passed through one of four analyzers that function together as a Stokes polarimeter. These analyzers are formed by a wave plate array and a polarizer array.

The second component of this focal plane array, located on the opposite side of the silicon substrate from the beamfanner, is a 256×256 array of form-birefringent wave plate pixels. Each wave plate pixel is oriented to one of the four beams, the beam designated to give information on circular polarization.

A layer of SU8 photoresist acts as a planarizing layer between the wave plate array and the third component, a Molybdenum wire grid polarizer array. The polarizer array is a 256×256 array of pixels with each pixel subdivided into a 2×2 array of polarizers with the appropriate orientations necessary for obtaining a complete Stokes vector description of the image. Often, in this dissertation, a beamfanner detector plane is mentioned. This plane corresponds to the location of the plane that is occupied by the wave plate array and is approximately 340 microns from the surface of the beamfanner array. For a complete description and view of this focal plane array, refer to [1], [2], [3] and Figure 1.1. A detailed analysis of finite-aperture wire grid polarizers, using the Finite Difference Time Domain (FDTD) method [4], [5], [6], [7], [8] is presented in [9]. Applications of imaging polarimetry are discussed in [10].

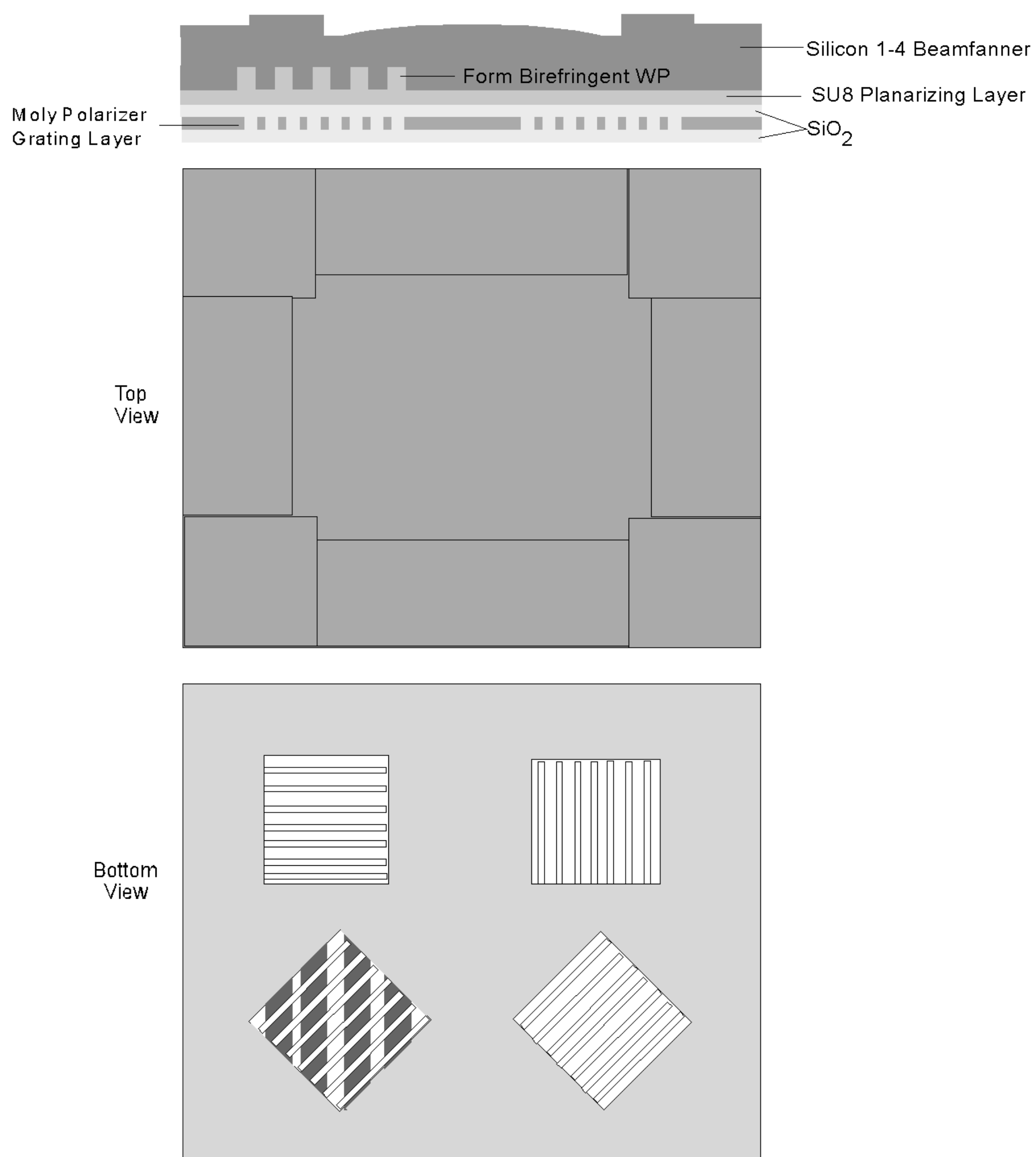

Figure 1.1 Cross-section, top (input), and bottom (output) views of the proposed focal plane array (FPA).

1.2 Focus

The beamfanner arrays present an interesting challenge from the standpoints of design and fabrication. The design of the beamfanner arrays makes use of a unique algorithm developed by Stephen D. Mellin of the University of Alabama in Huntsville that is called the Iterative Angular Spectrum Approach (IASA) [11]. Rigorous electromagnetic analysis, in form of the Boundary Element Method (BEM), is used to analyze design performance [12], [13]. The resulting designs demanded that a silicon device consisting of a large number of phase levels be fabricated. Grayscale photolithography and Reactive Ion Etching supplied the techniques necessary for construction of the beamfanners. The design and fabrication of the 1-4 and 1-2 test beamfanners and the focal plane array beamfanners represent the author's original work. The focus of this dissertation had the ambitious goal of developing a working 1-4 beamfanner array. This did not prove to be possible, but there is other important information to be gained from this research. First of all, the 1-2 test beamfanners were tested, though their actual performance did not match the performance predicted in the design process. Since a large number of beamfanner arrays are fabricated, etch repeatability and etch selectivity, the latter as a function of feature depth, are examined. These items will help develop knowledge and understanding for future efforts using grayscale fabrication methods.

1.3 Organization of dissertation

The second chapter of this dissertation will introduce and describe the various existing techniques used to achieve grayscale photolithography. High Energy Beam Sensitive Glass (HEBS) masks are an option for photoresist exposure, and one was used in the Nichols fabrication attempt. Chrome-on-quartz masks are another possible method. Laser direct writing

and electron beam writing into the photoresist are possible, though much more time consuming methods.

The third chapter will introduce the analytical methods used to design and characterize performance for the 256×256 beamfanner array as well as some test structures designed to mimic the performance of specific areas of the array. The Iterative Angular Spectrum Algorithm (IASA) developed by Stephen Mellin, which is the fundamental tool used in designing the beamfanners, is briefly reviewed. The rigorous diffraction theory of the Boundary Element Method (BEM), and its use in beamfanner design and performance characterization, is presented. The actual design, placement, and predicted performance of the beamfanners are covered.

The fourth chapter describes the methods and processes used in the fabrication of the beamfanners. Two attempts were made to fabricate a beamfanner array. The first, involving the Nichols device previously discussed, used a HEBS mask with 2 and 3-micron square features for contact photolithography. The small feature sizes and the poor quality of the HEBS mask made fabrication of a working device impossible, but the attempt, as well as the lessons learned, are presented. The second attempt, henceforth designated as the UAH array, made use of a proprietary photolithographic process employed by MEMS-Optical of Huntsville, Alabama. Research done to determine the etch selectivity (defined as the ratio of the etch rate of the substrate to the etch rate of the photoresist) needed for beamfanner fabrication was conducted by this author. The final fabrication step employed a reactive-ion-etcher (RIE) to etch the beamfanners in a silicon substrate. This final step was also the author’s effort.

The fifth chapter examines issues of etch repeatability and etch-depth dependent selectivity. Repeatability is a necessary ingredient in a successful micro-fabrication process and often proves elusive no matter how carefully the etching parameters are controlled. Etch parameters have a habit of changing over time, since RIE chamber conditions have a tendency to drift over time. The challenge is to find a set of etch parameters that are robust enough such that there is minimal change over a duration of time necessary to complete a fabrication task.

Selectivity, as previously mentioned, is defined as the ratio of the etch-depth of a feature in silicon to the depth of that same feature in photoresist. A grayscale process yields multiple phase levels, and since different feature depths may exhibit different selectivities for the same set of etching parameters, it is important to quantify these differences. Experimental procedures and statistics are used to control and define this study.

The sixth chapter gives the results of testing that characterize the performance of the beamfanner arrays. Output from the 1-2 beamfanner test arrays is compared directly to the performance predicted by BEM, and a qualitative examination of the 1-4 arrays is presented. A lens system that mimicked the function of the polarimeter camera and an infrared microscope provided by CSC in Huntsville, Alabama was used to obtain these results.

The seventh and final chapter presents overall conclusions and suggestions for relevant future research.

Chapter 2

BACKGROUND OF GRAYSCALE FABRICATION TECHNIQUES

2.1 Grayscale photolithograpy (motivation)

Grayscale photolithography offers a single step alternative to binary micro-fabrication. In a binary fabrication process, photoresist is alternately masked, exposed, developed, and etched. During the exposure, a binary mask either allows exposing UV light to illuminate the photoresist, or it shields the resist entirely. It therefore requires one photolithographic/etching step to produce an element with two phase levels, two steps for four phase levels, three for eight levels, and in general N steps for 2^N phase levels [14].

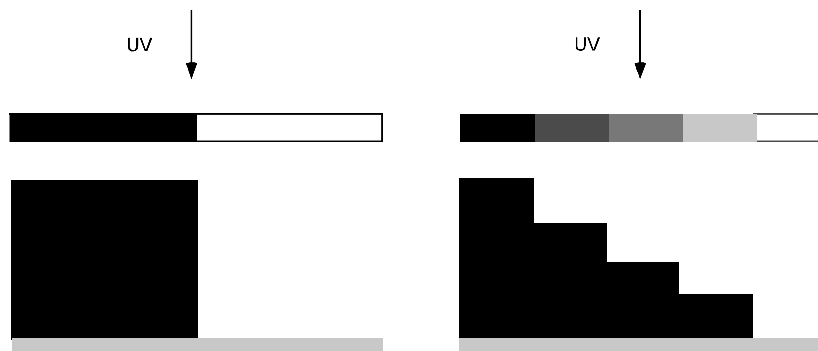

Figure 2.1 Comparison of binary and grayscale UV resist exposure schemes.

Figure 2.1 illustrates both a two level profile, typical of a one-step binary photolithographic process, and a five level profile, typical of a gray-level process. The first scheme, on the left, is often used in the fabrication of gratings with rectangular profiles. This view shows a binary photomask illuminated from above by UV radiation. This will produce a two-level pattern in photoresist upon development. The five level grayscale mask on the right is used to produce, in a single exposure step, a five level structure. This structure would require a three-step exposure process using a binary process.

Often, the addition of more phase levels to closely approximate an analog contour will significantly enhance device performance [15]. It is clear that a device whose successful function depends on a large number of phase levels to approximate a continuous contour will require a many step process costing time and material. It will also be subject to multiple errors due to the mask alignment that accompanies each fabrication step. Typical contact alignment errors can cause lateral deviations up to 0.5 microns [16]. Misalignments can decrease the efficiency of a diffractive optic device by altering the lateral size of a feature from the maximal design specification [17]. Grayscale methods, however, allow for the fabrication of devices with arbitrary numbers of phase levels or even continuous profiles [18] and reduce the number of fabrication steps, and, consequently, the chance for an alignment error, to one. Grayscale lithography allows the exposure of thick (around several tens of micrometers) photoresist layers [19].

Grayscale processes do possess disadvantages. A binary process, especially one that produces evenly spaced features of equal height, such as a grating, allows a single set of exposure, development, and etch parameters to uniformly affect all structures. This does not hold true for a complex multilevel structure, since different feature heights and lateral sizes will not, in general be uniformly processed by a single set of etching parameters. Typical sources of error in grayscale fabrication include photoresist depth errors [20] and rounding of some features during

the etch process. An illustration, typical of the results presented in this dissertation, is seen below in Figure 2.2.

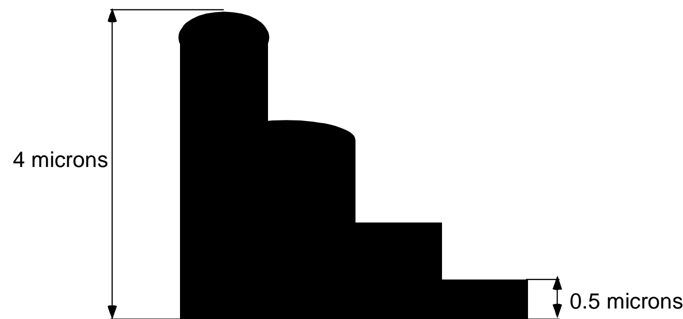

Figure 2.2 Four gray-level features with rounding of the two highest features.

To obtain good feature transfer fidelity during an etch process, it is necessary that the etch process be highly anisotropic simultaneously for all phase levels. This can require a great amount of experimentation to achieve success. In binary fabrication, much work has been done and the processes are well understood. Grayscale processes are more recent in development and less well understood.

2.2 Grayscale mask techniques

In order to achieve gray-level exposures in photoresist, it is necessary to have a mask with varying optical densities, thus allowing a wide variety of exposure energies to transfer to a varying resist profile. Three available types of grayscale masks are the High Energy Beam Sensitive (HEBS) mask [21], [22], the Laser Direct Write (LDW) mask, and the chrome-on-

quartz mask [23]. These masks make use of varying densities of sub-resolution particles in or on the glass to block out exposing radiation to various degrees.

The HEBS mask is made of a low expansion zinc-borosilicate glass, a white crown glass. This glass contains alkali to facilitate ion exchange reactions that make the glass sensitive to high energy beams, electron beams in particular. The ion exchange process is carried out long enough to cause silver ions to diffuse into the glass to a depth of up to 3 microns. This process is conducted at temperatures above 320 degrees centigrade, and silver-alkali-halide containing complex crystals are formed. Chemical reduction of the silver ions in these crystals to produce opaque regions of silver atoms is achieved by exposing the glass to high energy beams, i.e., > 10 kilovolt electron beams. By varying the energy of the electron beams, it is possible to vary the density of the silver particles and, hence, the optical density [24], [25].

The LDW mask [26] is made the same way as the HEBS mask, except that pattern writing on the mask is based on laser exposure heat erasure of the opaque silver particles. LDW glass initially contains a large density of opaque silver particles. The depth of this layer of particles can be varied from 1 to 3 microns. This corresponds to an optical density of between 1.4 and 3 at a wavelength of 436 nm, which is a typical, and often maximal, wavelength for exposing photoresist. A focused laser beam is used to heat erase the silver particles by changing the metal silver back to ionic silver.

Chrome-on-quartz masks are similar to standard binary masks, since chrome makes up the dark field of many such masks. Grayscale masks of this type, however, employ sub-resolution regions of chrome on the quartz mask surface to function as the opaque particles. There are two schemes for realizing the varied exposures typical of grayscale masks. The first uses chromium pixels with different sizes but constant pitch. The second uses constant sizes with varied pitch [27]. The pitch is altered by varying the center-to-center distance between adjacent chrome pixels. These two schemes can also be combined on the same mask. Chrome-on-quartz masks are advantageous because standard binary mask fabrication technologies are easily adapted

to make these masks. The chrome regions are naturally much larger (typically on the order of 0.5 microns square) than the silver atoms described for the HEBS and LDW masks, but non-contact printing using a stepper is a useful option with these masks.

2.3 Direct writing techniques

Direct writing into photoresist with either an electron beam or a laser beam [28] is another common approach to the fabrication of multiple phase level optical elements. Spot sizes for e-beam systems are usually 0.1 microns or larger, and laser direct systems have larger spot sizes on the order of 1-5 microns. After the photoresist is developed, the depth of the local relief structure is proportional to the energy delivered to that area by the e-beam or the laser source. Either the power or the dwell time of the source can be varied to yield different exposure energies. This allows for fabrication of nearly continuous relief structures that approximate the curved topography needed for maximal performance of many optical elements.

There is a major disadvantage to this approach, however. It is a serial process, so each element must be written one at a time. It is far more feasible from the standpoint of efficiency for large area or large volume production to use a mask/exposure scheme rather than direct writing. As is so often true in micro-fabrication, reduction of time and cost is paramount, and the mask/exposure method, if feasible, is far preferable to a serial process.

Chapter 3

MODELLING AND DESIGN OF BEAMFANNER ARRAY AND TEST ARRAYS

The first section of this chapter presents the beamfanner design method, IASA. The second section presents the rigorous diffraction theory, BEM, used to test the beamfanner designs yielded by IASA. The third section describes the specific designs and substrate placement location of the Nichols and UAH beamfanner arrays. Finally, in the fourth section, specific designs and simulations of 1-2 beamfanners are developed for the UAH array. These simulation results will ideally be compared to test results obtained after the fabrication of these beamfanners.

3.1 The Iterative Angular Spectrum Algorithm (IASA)

The design of the beamfanner arrays was accomplished using a modification of the Gerchberg-Saxton Algorithm [29] or the Iterative Fourier Transform Algorithm [30] that was developed by Steve Mellin of the University of Alabama in Huntsville. This algorithm was given the name, Iterative Angular Spectrum Algorithm (IASA). As shown in Steve Mellin's Ph.D. research, IASA is a scalar design method that is useful for creating DOE profiles, and its novelty consists of the addition of evanescent field components from proceeding to succeeding iterations. IASA is computationally more efficient than rigorous design methods and has been shown to be useful for some DOE designs outside the realm of scalar theory. Specifically, a wide range of IASA designs with feature sizes smaller than a wavelength have been shown to test effectively with rigorous vector diffraction theory, provided that the smaller features collectively approximated the contours of larger features to which scalar theory would normally be applied.

A qualitative description of the process used to design the 1-2 beamfanner will now be presented. This 1-2 beamfanner serves as the basis for all other beamfanner designs discussed in this dissertation. For the basis design, a unit amplitude 5-micron plane wave (in free space) is assumed to be normally incident on a finite aperture DOE etched in silicon. The DOE is constrained to split the light equally between two photodetectors in an observation plane in the near field. These photodetectors have a width of 15 microns with a center-to-center spacing of 25 microns. They are located in a plane that is 340 microns from the silicon substrate's surface of incidence. Each silicon beamfanner's surface-of-incidence is bounded by a 50-micron aperture.

Steve Mellin's IASA procedure to yield the 1-2 beamfanner design was commenced by assuming an initial DOE profile of a flat dielectric (air/silicon) interface subdivided into 1-micron lateral feature sizes and bounded by a 50-micron infinitely conducting finite aperture. The transmission function and the field just past the DOE were first calculated. The angular spectrum of this field was determined using a Fast Fourier Transform (FFT) and propagated to observation plane in which the detectors are located. These detectors are 15 microns wide and have a center-to-center spacing of 25 microns. They correspond in position to the polarizer apertures described in the introductory section discussion of the real time polarimeter focal plane array. The field at the observation plane was obtained using an Inverse Fast Fourier Transform (IFFT). The diffraction pattern yielded by this transform was then compared with the ideal case where all of the light is evenly split between the pair of detector apertures. At this point in the process, if the field profile at the observation plane satisfied the conditions for the operation of the 1-2 beamfanner, the calculations could be discontinued. However, if the field profile did not meet these conditions, the field was modified according to constraint criteria. These criteria insisted, as in Figure 3.1, that the field amplitudes were increased at positions in the observation plane corresponding to the locations of the detector apertures, and that the incident light was diffracted such that if either half of the incident beamfanner surface was illuminated, a split intensity profile was yielded in the detector plane.

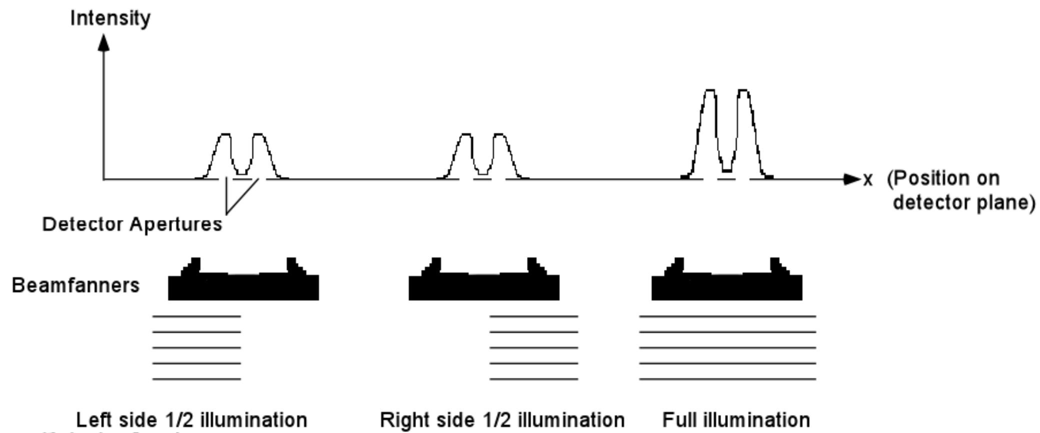

Figure 3.1 Equal splitting of amplitude by beamfanners in the detector plane.

The angular spectrum of this modified field was obtained by FFT and back propagated to the DOE plane of incidence. Evanescent field components from the angular spectrum iteration at the previous plane of incidence were then added to obtain the total angular spectrum. The DOE profile was modified with the condition that it was a phase-only DOE bounded by a finite aperture. At this point, the second iteration can begin by calculating the new transmission function past the DOE, incorporating the evanescent components from the last iteration. This iterative process was repeated until a 1-2 beamfanner device structure profile and image plane field profile were obtained. This structure is shown in Figure 3.13 at the end of this chapter.

It later proved impossible to fabricate beamfanners with 3-micron lateral features, much less 1-micron lateral features. The photolithography and etching processes developed were insufficient to preserve good feature fidelity. It was necessary to redesign the beamfanners with a minimum lateral feature size of 5 microns. The redesign, analysis, fabrication, and testing of these beamfanners will be extensively covered in the third and fourth sections of this chapter.

3.2 The Boundary Element Method (BEM)

IASA provides a means to obtain a beamfanner design, but is not inherently rigorous enough to provide accurate predictions of device performance [31], [32]. Indeed, IASA was tested by employing the Boundary Element Method (BEM). BEM is a rigorous boundary integral method adapted for computer numerical implementation. Boundary integral methods are well suited for the analysis of homogeneous, finite, aperiodic DOE's. Boundary integral methods use the integral form of the wave equation to describe the induced polarization field distribution on the surface of the DOE. Re-radiation from this surface distribution in turn generates a diffracted field that can be determined anywhere in space. Presented here is the basic theory of a boundary integral method as it pertains to aperiodic, finite, homogeneous, open-contour DOE's and its application to the basic 1-2 beamfanner that was developed using IASA. The three-dimensional version of Green's second identity is first derived. This is followed by its reduction to a two-dimensional problem used to handle the geometries of the 1-2 beamfanners. Application of boundary conditions at a dielectric interface are employed to simplify the resulting equations so that the field distributions can be determined at the dielectric interface using the computer adapted BEM method [33]. The adaptation of this boundary integral method to BEM is next presented. This is followed, in the third and fourth sections, by an overview of the design for the first (Nichols) and second (UAH) beamfanner array series and an analysis of 1-2 beamfanners from the UAH array redesigned for greater ease of fabrication with larger lateral feature sizes and fewer phase levels than Mellin's original Nichols array design. Off-axis illumination and spherical convergence of the focused illuminating infrared light are considered in the design. Finally, the 1-2 beamfanner designs are coupled together to form 1-4 beamfanners as required for the design of both the Nichols and UAH 256×256 beamfanner arrays.

3.2.1 Derivation of rigorous boundary integral diffraction theory

The derivation of the necessary boundary integral equations and their adaptation to a computer friendly numerical method is covered next. Assuming linear, homogeneous, isotropic dielectric media, and given Maxwell's equations,

$$\nabla \cdot \vec{E} = \frac{\rho}{\varepsilon} \ ,$$

$$\nabla \times \vec{E} = -\mu \frac{\partial \vec{H}}{\partial t} ,$$

$$\nabla \cdot \vec{H} = 0 ,$$

$$\nabla \times \vec{H} = \vec{J} + \varepsilon \frac{\partial \vec{E}}{\partial t} \ , \qquad (3.1)$$

and assuming time harmonic field dependence using the phase convention $e^{[-j(\vec{k}\cdot\vec{r}-\omega t)]}$, these equations can be expressed as

$$\nabla \cdot \vec{E} = \frac{\rho}{\varepsilon} ,$$

$$\nabla \times \vec{E} = -j\omega\mu\vec{H} ,$$

$$\nabla \cdot \vec{H} = 0 \text{, and}$$

$$\nabla \times \vec{H} = \vec{J} + j\omega\varepsilon\vec{E} , \qquad (3.2)$$

where ρ, ε, μ, and ω are the charge density, permittivity, permeability, and angular frequency of light respectively. The Helmholtz-wave-equations are derived by taking the curl of the second

and fourth expressions in Equation (3.2) and making the appropriate substitutions [34], [35]. They are given below in Equation (3.3).

$$\nabla^2\vec{E} + \omega^2\mu\varepsilon\vec{E} = \frac{1}{\varepsilon}\nabla\rho + j\omega\mu\vec{J} = -\vec{f}(\vec{r}), \text{ and}$$

$$\nabla^2\vec{H} + \omega^2\mu\varepsilon\vec{H} = \nabla\times\vec{J} = -\vec{g}(\vec{r}) \,. \tag{3.3}$$

The expressions $\vec{f}(\vec{r})$ and $\vec{g}(\vec{r})$ are spatially dependent source terms. BEM analysis is simplified if the TE and TM cases are treated separately. This fact, coupled with demands placed on computer memory, made it necessary to consider only the two-dimensional geometry of the 1-2 beamfanner for design and modelling purposes. The TE and TM cases are separable in the two dimensions, and the two-dimensional case requires far less computer memory. With this in mind, the Helmholtz equation for the electric field is applied to the former, and the Helmholtz equation for the magnetic field is used for the latter to obtain a complete solution.

The solution to the dielectric boundary value problem that is applicable to this specific DOE design requires the use of Green's second identity, which is derived below. Given the divergence theorem $\int_V \nabla\cdot\vec{A}dV' = \oiint_S \vec{A}\cdot\hat{n}dS'$ and making the substitutions $\vec{A} = \phi\nabla\psi$, $\nabla\cdot\vec{A} = \nabla\cdot(\phi\nabla\psi) = \phi\nabla^2\psi + \nabla\phi\cdot\nabla\psi$, and $\vec{A}\cdot\hat{n} = (\phi\nabla\psi)\cdot\hat{n} = \phi\frac{\partial\psi}{\partial n}$, where $\hat{n}$ is the unit normal, Green's first identity can be written as

$$\int_V (\phi\nabla^2\psi + \nabla\phi\cdot\nabla\psi)dV' = \oiint_S \phi\frac{\partial\psi}{\partial n}dS' \,. \tag{3.4}$$

Setting $\vec{A} = \psi\nabla\phi$, and performing the same operation as above, the following equation is obtained.

$$\int_V (\psi \nabla^2 \phi + \nabla \phi \cdot \nabla \psi) dV' = \oint\!\!\oint_S \psi \frac{\partial \phi}{\partial n} dS'. \tag{3.5}$$

Subtracting Equation (3.5) from Equation (3.4) yields Green's second identity [36].

$$\int_V (\phi \nabla^2 \psi - \psi \nabla^2 \phi) dV' = \oint\!\!\oint_S (\phi \frac{\partial \psi}{\partial n} - \psi \frac{\partial \phi}{\partial n}) dS'. \tag{3.6}$$

The formalism is now in place for the treatment of the three-dimensional dielectric boundary value problem. Figure 3.2 shows a general geometrical interpretation of this problem, with a volume bounded by a surface in three dimensions. Integrations are performed over the volume enclosed by the surface and also the surface.

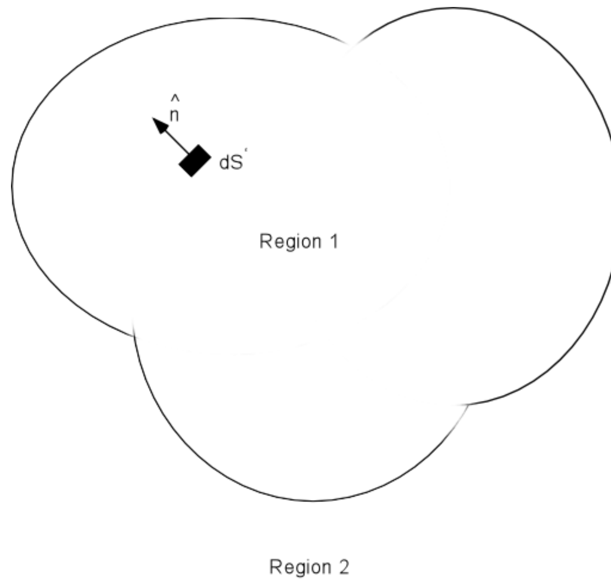

Figure 3.2 Three-dimensional volume and enclosing surface with differential surface area and outward pointing normal vector.

The TE and TM cases, as mentioned before, will be treated separately, since different boundary conditions are imposed on each. The TE and TM orientations will be the y-components of both the electric and magnetic fields. Since the derivations for both are very similar, only the TE case will be presented in detail. Let the TE case be considered such that $\vec{E}_{TE} = E_y \hat{y}$, and substitute E_y for ϕ and G for ψ in Equation (3.6). This gives

$$\int_V (E_y \nabla^2 G - G \nabla^2 E_y) dV' = \oiint_S (E_y \frac{\partial G}{\partial n} - G \frac{\partial E_y}{\partial n}) dS'. \tag{3.7}$$

The Green's function is given by $G(\vec{r}, \vec{r}\,') = \frac{1}{4\pi} \frac{e^{-jk|\vec{r}-\vec{r}\,'|}}{|\vec{r}-\vec{r}\,'|}$. It satisfies the equation,

$$\nabla^2 G(\vec{r}, \vec{r}\,') + k^2 G(\vec{r}, \vec{r}\,') = -\delta(\vec{r} - \vec{r}\,'), \tag{3.8}$$

in which $\delta(\vec{r} - \vec{r}\,')$ is the three-dimensional delta function, and $k = \omega\sqrt{\mu\varepsilon}$. By substituting the Helmholtz wave equation for the electric field, Equation (3.3), and Equation (3.8) into Equation (3.7), this expression is obtained.

$$\int_V [E_y(-\delta(\vec{r} - \vec{r}\,') - k^2 G(\vec{r}, \vec{r}\,')) - G(\vec{r}, \vec{r}\,')(-\vec{f}(\vec{r}\,') - k^2 E_y)] dV' =$$

$$\int_V [-E_y \delta(\vec{r} - \vec{r}\,') + G(\vec{r}, \vec{r}\,') \vec{f}(\vec{r}\,')] dV' = -E_y(\vec{r}) + \int_V G(\vec{r}, \vec{r}\,') \vec{f}(\vec{r}\,') dV'$$

$$= \oiint_S (E_y(\vec{r}\,') \frac{\partial G(\vec{r}, \vec{r}\,')}{\partial n} - G(\vec{r}, \vec{r}\,') \frac{\partial E_y(\vec{r}\,')}{\partial n}) dS'. \tag{3.9}$$

The source and, as a consequence, the incident field are chosen to originate in region 1. The above expression can be further simplified by integrating the product of the Green's function and the source term over the enclosed volume, yielding this boundary integral equation,

$$-E_{yi}(\vec{r}) + E_{inc}(\vec{r})\delta_{i,1} = \oiint_S (E_{yi}(\vec{r}\,')\frac{\partial G_i(\vec{r},\vec{r}\,')}{\partial n} - G_i(\vec{r},\vec{r}\,')\frac{\partial E_{yi}(\vec{r}\,')}{\partial n})dS'. \tag{3.10}$$

The index, i, is equal to 1 for region 1, and 2 for region 2. The Kronecker delta, $\delta_{i,1}$, is equal to 1 in the source region 1 and 0 in region 2. This will yield two equations in two different regions that can be matched at a dielectric interface using boundary conditions imposed by Maxwell's equations. For proof that $E_{inc}(\vec{r})\delta_{i,1} = \int_V G_i(\vec{r},\vec{r}\,')\vec{f}_i(\vec{r}\,')dV'$, recall from Equation (3.3) that $\vec{f}(\vec{r}) = -\frac{1}{\varepsilon}\nabla\rho - j\omega\mu\vec{J}$ in region 1. The incident field can be expressed as

$$\int_V G_i(\vec{r},\vec{r}\,')\vec{f}(\vec{r}\,')dV' = -\frac{1}{\varepsilon}\int_V \nabla'\rho(\vec{r}\,')G_i(\vec{r},\vec{r}\,')dV' - j\omega\mu\int_V \vec{J}(\vec{r})G_i(\vec{r},\vec{r}\,')dV'. \tag{3.11}$$

The Green's function can be considered to be the impulse response of this system and any linear operator acting on the input has the same effect on the output. The del operator may therefore be brought outside the integrand in the first right hand term of Equation (3.11), i.e.,

$$\int_V G_i(\vec{r},\vec{r}\,')\vec{f}(\vec{r}\,')dV' = -\frac{1}{\varepsilon}\nabla\int_V \rho(\vec{r}\,')G_i(\vec{r},\vec{r}\,')dV' - j\omega\mu\int_V \vec{J}(\vec{r})G_i(\vec{r},\vec{r}\,')dV'. \tag{3.12}$$

Classical electrodynamics says that the electric potential, Φ, in terms of the volume charge density, is expressed as

$$\Phi(\vec{r}) = \frac{1}{\varepsilon}\int_V \rho(\vec{r}\,')G(\vec{r},\vec{r}\,')dV', \tag{3.13}$$

and that the vector potential can be expressed as

$$\vec{A}(\vec{r}) = \mu \int_V \vec{J}(\vec{r}\,')G(\vec{r},\vec{r}\,')dV'\,. \tag{3.14}$$

The general expressions for the electric and magnetic fields are

$$\vec{E}(\vec{r},t) = -\nabla\Phi(\vec{r},t) - \frac{\partial \vec{A}(\vec{r},t)}{\partial t}\text{, and}$$

$$\vec{H}(\vec{r},t) = \frac{1}{\mu}\nabla\times\vec{A}(\vec{r},t)\,. \tag{3.15}$$

Assuming time harmonic dependence, these expressions become

$$\vec{E}(\vec{r}) = -\nabla\Phi(\vec{r}) - j\omega\vec{A}(\vec{r})\text{, and}$$

$$\vec{H}(\vec{r},t) = \frac{1}{\mu}\nabla\times\vec{A}(\vec{r})\,. \tag{3.16}$$

It is now possible to express the volume integral of the product of the Green's function and the source term as

$$\int_V \vec{f}(\vec{r}\,')G_i(\vec{r},\vec{r}\,')dV' = -\nabla\Phi(\vec{r}) - j\omega\vec{A}(\vec{r}) = \vec{E}_{inc}(\vec{r})\,. \tag{3.17}$$

A similar argument can be made for the magnetic field, noting that $\vec{g}(\vec{r}) = \nabla\times\vec{J}$, is applicable to the TM case.

$$\int_V G_i(\vec{r},\vec{r}\,')\vec{g}(\vec{r}\,')dV' = \int_V \rho(\vec{r}\,')G_i\left(\vec{r},\vec{r}\,'\right)dV' - j\omega\mu\int_V \vec{J}(\vec{r})G_i(\vec{r},\vec{r}\,')dV'$$

$$= \frac{1}{\mu}\nabla\times\vec{A}(\vec{r}) = \vec{H}_{inc}(\vec{r})\,. \tag{3.18}$$

Design of 1-2 beamfanners simplifies this boundary integral analysis, since the right hand side of Equation (3.10) must be converted into a line integral if solutions separable in TE and TM modes are to be obtained. For the following analysis, the unit normal vector directed outward from region 2 is the negative of the unit normal directed outward from region 1, i.e., $\hat{n}_2 = -\hat{n}_1 = \hat{n}$. Figure 3.3 shows the two-dimensional geometry representative of the design work used to develop the beamfanners.

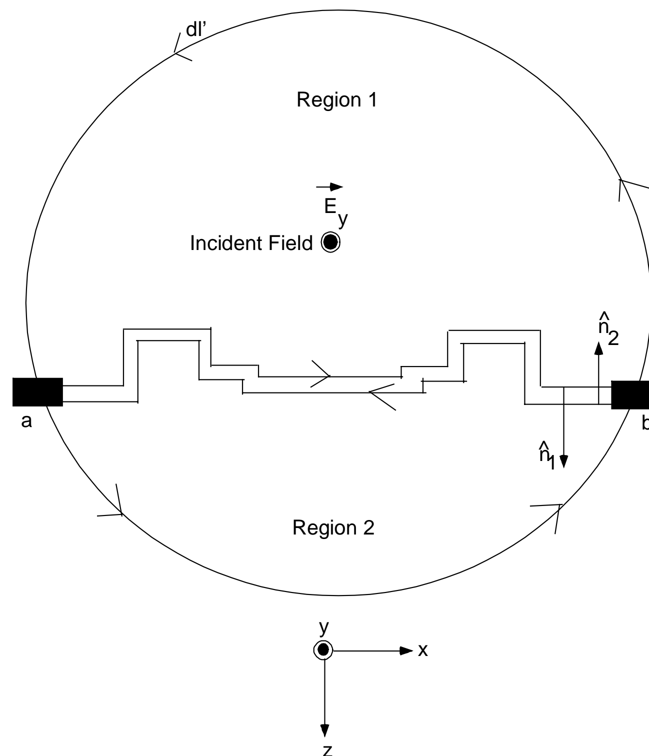

Figure 3.3 Two-dimensional line integration representing the DOE boundary with a and b as conducting pads defining a finite aperture.

From Equation (3.10), expressions for the boundary integral equation can be obtained in regions 1 and 2.

$$E_{y1}(\bar{r}) = E_{inc}(\bar{r}) + \oiint_S (E_{y1}(\bar{r}')\frac{\partial G_1(\bar{r},\bar{r}')}{\partial n} - G_1(\bar{r},\bar{r}')\frac{\partial E_{y1}(\bar{r}')}{\partial n})dS'.$$

$$E_{y2}(\bar{r}) = -\oiint_S (E_{y2}(\bar{r}')\frac{\partial G_2(\bar{r},\bar{r}')}{\partial n} - G_2(\bar{r},\bar{r}')\frac{\partial E_{y2}(\bar{r}')}{\partial n})dS'. \quad (3.19)$$

If the fields and their normal derivatives are assumed to be constant with respect to y', the surface integral may be expressed as $dS' = dy'd\ell'$.

For integration over the y'-coordinate, only the Green's function terms are affected.

$$\int_{-\infty}^{\infty} G_i(\bar{r},\bar{r}')dy' = \int_{-\infty}^{\infty} \frac{e^{-jk_i|\bar{r}-\bar{r}'|}}{4\pi|\bar{r}-\bar{r}'|}dy' = \frac{1}{4j}H_0^{(2)}(k_i|\bar{r}-\bar{r}'|). \quad (3.20)$$

$H_0^{(2)}$ is the zero-order Hankel function of the second kind. The surface normal vector, $\hat{n}$, is now confined to the x-z plane, and the two-dimensional Green's function of Equation (3.20) can be substituted for the three-dimensional Green's functions in the boundary integral expressions of Equation (3.19), yielding

$$E_{y1}(\bar{r}) = E_{inc}(\bar{r}) + \oint_C [E_{y1}(\bar{r}')\frac{\partial G_1(\bar{r},\bar{r}')}{\partial n} - G_1(\bar{r},\bar{r}')\frac{\partial E_{y1}(\bar{r}')}{\partial n}]d\ell', \text{ and}$$

$$E_{y2}(\bar{r}) = -\oint_C [E_{y2}(\bar{r}')\frac{\partial G_2(\bar{r},\bar{r}')}{\partial n} - G_2(\bar{r},\bar{r}')\frac{\partial E_{y2}(\bar{r}')}{\partial n}]d\ell', \quad (3.21)$$

where the two-dimensional Green's function is given in Equation (3.20), and its normal derivative is

$$\frac{\partial G_i(\bar{r},\bar{r}')}{\partial n} = k_i \frac{j}{4} H_1^{(2)}(k_i|\bar{r}-\bar{r}'|)\hat{n}_i \cdot \hat{r}\text{, and} \tag{3.22}$$

$$\hat{r} = \frac{\bar{r}-\bar{r}'}{|\bar{r}-\bar{r}'|}.$$

The contour, C, is the two-dimensional boundary of the DOE shown in Figure 3.3. For this case of a finite aperture DOE, it is necessary to perform the integration only along the boundary bounded by the finite aperture bordered by the conducting pads that are labeled a and b.

The Green's functions are singular at points on the boundary where $\bar{r} = \bar{r}'$, and caution must be exercised when the integrals of Equation (3.21) are evaluated. The singularities are mastered by considering a small circular contour of radius $\in$, as shown in Figure 3.4.

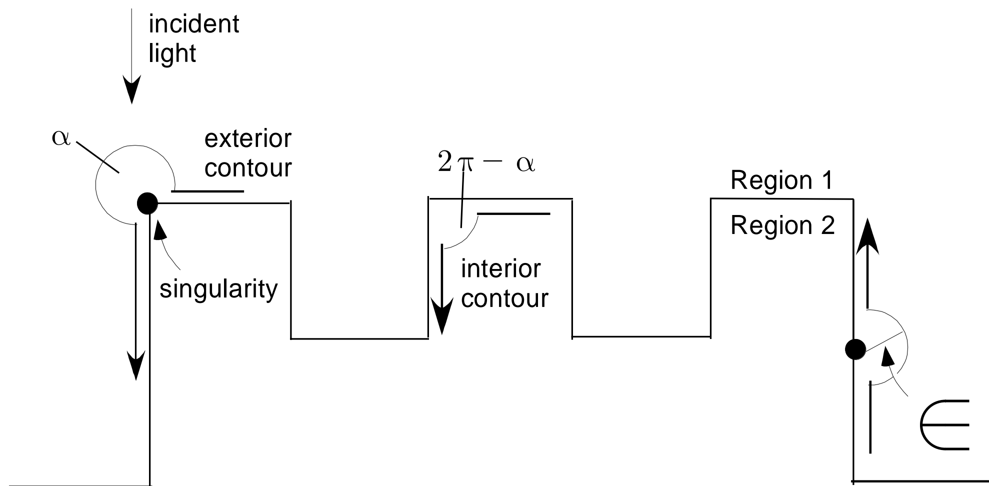

Figure 3.4 Singularities along DOE contour to be integrated.

Consider the following integral equation.

$$\oint_C E_{yi}(\vec{r}\,')\frac{\partial G_i(\vec{r},\vec{r}\,')}{\partial n}d\ell' =$$

$$\oint_{Cauchy} E_{yi}(\vec{r}\,')\frac{\partial G_i(\vec{r},\vec{r}\,')}{\partial n}d\ell' + \lim_{\in\to 0}\int_{-\frac{\alpha}{2}}^{\frac{\alpha}{2}} [E_{yi}(\vec{r}\,')\frac{\partial G_i(\vec{r},\vec{r}\,')}{\partial n} \in d\theta\,. \quad (3.23)$$

The Cauchy term integrates the large contour, and the second term on the right integrates the small contour that surrounds the singularity on the boundary of the DOE. $\in = \lim_{\vec{r}\to\vec{r}\,'}\left|\vec{r}-\vec{r}\,'\right|$ and α is the exterior angle at a singular boundary point. To evaluate the second term on the right in Equation (3.23), the small argument approximations for the relevant Hankel's functions are used. These are

$$H_0^{(2)}(\in) \approx 1 - j\frac{2}{\pi}\ln(\frac{\gamma\in}{2}), \text{ and} \quad (3.24)$$

$$H_1^{(2)}(\in) \approx \frac{\in}{2} + j\frac{2}{\pi\in}\,. \quad (3.25)$$

These equations are valid as $\in \to 0$. Euler's constant, γ, is equal to 1.781. Substituting Equations (3.24) and (3.25) for the Green's functions and their normal derivatives in Equation (3.21) allows the following integral operations,

$$\oint_C G_2(\vec{r},\vec{r}\,')\frac{\partial E_{y2}(\vec{r}\,')}{\partial n}d\ell\,' =$$

$$\oint_{Cauchy} G_2(\vec{r},\vec{r}\,')\frac{\partial E_{y2}(\vec{r}\,')}{\partial n}d\ell\,' + \lim_{\in\to 0}\int_{-\frac{\alpha}{2}}^{\frac{\alpha}{2}}[1 - j\frac{2}{\pi}\ln(\frac{\gamma k_2 \in}{2})]\frac{\partial E_{y2}(\vec{r}\,')}{\partial n}\in d\theta\,. \tag{3.26}$$

Here, α is the exterior angle at a boundary point as shown in Figure 3.4. Since $\lim_{\in\to 0}\in\ln(\in) = 0$, the far right hand integral goes to zero, yielding the following expression,

$$\oint_C G_2(\vec{r},\vec{r}\,')\frac{\partial E_{y2}(\vec{r}\,')}{\partial n}d\ell\,' = \oint_{Cauchy} G_2(\vec{r},\vec{r}\,')\frac{\partial E_{y2}(\vec{r}\,')}{\partial n}d\ell\,'\,. \tag{3.27}$$

The integral containing the normal derivative of the Green's function and the electric field is next evaluated,

$$\oint_C E(\vec{r}\,')_{y2}\frac{\partial G_2(\vec{r},\vec{r}\,')}{\partial n}d\ell\,' =$$

$$\oint_{Cauchy} E(\vec{r}\,')_{y2}\frac{\partial G_2(\vec{r},\vec{r}\,')}{\partial n}d\ell\,' + \frac{jk_2}{4}(\hat{n}\cdot\hat{r})\lim_{\in\to 0}\int_{-\frac{\alpha}{2}}^{\frac{\alpha}{2}} E_{y2}(\vec{r}\,')[\frac{k_2\in}{2} + j\frac{2}{\pi k_2\in}]\in d\theta\,. \tag{3.28}$$

Keeping in mind that the term $(\hat{n}\cdot\hat{r})$ is equal to 1 over the circular arc enclosing the singularity, the expression above can be reduced to this equation,

$$\oint_C E(\vec{r}\,')_{y2}\frac{\partial G_2(\vec{r},\vec{r}\,')}{\partial n}d\ell\,' = \oint_{Cauchy} E(\vec{r}\,')_{y2}\frac{\partial G_2(\vec{r},\vec{r}\,')}{\partial n}d\ell\,' - \vec{E}_{y2}(\vec{r})\frac{\alpha}{2\pi}\,. \tag{3.29}$$

The expressions in Equations (3.27) and (3.29) can be inserted into the expressions of Equation (3.21) to obtain these equations for the scattered fields at a point on the DOE boundary.

$$E_{y1}(\bar{r}_b)\left(\frac{\alpha}{2\pi}\right) = E_{inc}(\bar{r}_b) + \oint_{Cauchy}[E_{y1}(\bar{r}\,')\frac{\partial G_1(\bar{r},\bar{r}\,')}{\partial n} - G_1(\bar{r},\bar{r}\,')\frac{\partial E_{y1}(\bar{r}\,')}{\partial n}]d\ell\,'\,. \quad (3.30)$$

$$E_{y2}(\bar{r}_b)\left(1-\frac{\alpha}{2\pi}\right) = -\oint_{Cauchy}[E_{y2}(\bar{r}\,')\frac{\partial G_2(\bar{r},\bar{r}\,')}{\partial n} - G_2(\bar{r},\bar{r}\,')\frac{\partial E_{y2}(\bar{r}\,')}{\partial n}]d\ell\,'\,. \quad (3.31)$$

Now that two expressions exist for the fields at the DOE boundary, which for the beamfanner designs is an air/silicon interface, it is possible to use boundary conditions derived from Maxwell's equations to eliminate two unknowns from the set of Equations (3.30) and (3.31). Figure 3.5 shows the fields at the interface between regions 1 and 2.

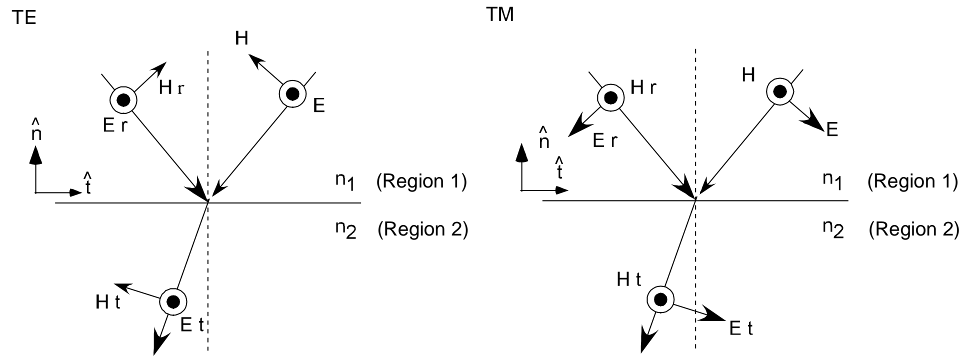

Figure 3.5 TE and TM fields at a dielectric interface.

The relevant boundary conditions for this analysis can be obtained from Maxwell's curl equations. They state that

$$\hat{n}\times(\vec{E}_2-\vec{E}_1)=0 \text{ and} \tag{3.32}$$

$$\hat{n}\times(\vec{H}_2-\vec{H}_1)=0. \tag{3.33}$$

It follows from Equation (3.32) that for the TE case, $E_{y1}=E_{y2}$. For the normal derivatives, it is useful to present a pair of vector identities,

$$\vec{a}\times(\vec{b}\times\vec{c})=(\vec{a}\cdot\vec{c})\vec{b}-(\vec{a}\cdot\vec{b})\vec{c} \text{ and} \tag{3.34}$$

$$\vec{a}\cdot(\vec{b}\times\vec{c})=\vec{b}\cdot(\vec{c}\times\vec{a})=\vec{c}\cdot(\vec{a}\times\vec{b}). \tag{3.35}$$

The electric fields take the form $\vec{E}=E_y\hat{y}=\left|\vec{E}\right|e^{-j(\vec{k}\cdot\vec{r})}\hat{y}$, and the gradient can be expressed as $\nabla E_y=-j\vec{k}E_y=-j(\vec{k}\cdot\hat{t})E_y\hat{t}-j(\vec{k}\cdot\hat{n})E_y\hat{n}$ in which $\hat{t}$ and $\hat{n}$ are the tangential and normal unit vectors with respect to the interface. Using the time harmonic Maxwell curl equation for the electric field, $\nabla\times\vec{E}=-j\omega\mu\vec{H}=-j\vec{k}\times\vec{E}$, and the vector identity of Equation (3.34), the wave vector can be solved as a function of the fields,

$$\vec{k}=\frac{\omega\mu}{(\vec{E}\cdot\vec{E})}\vec{E}\times\vec{H}. \tag{3.36}$$

Substituting this expression for the wave vector into the expression for the gradient of the field gives

$$\nabla E_y=-\frac{jE_y\omega\mu}{(\vec{E}\cdot\vec{E})}[((\vec{E}\times\vec{H})\cdot\hat{t})\hat{t}+((\vec{E}\times\vec{H})\cdot\hat{n})\hat{n}]. \tag{3.37}$$

By taking the dot product of the unit normal vector with the gradient of the electric field and applying the second vector identity, Equation (3.35), this relationship is obtained,

$$\hat{n}\cdot\nabla E_y = -j\omega\mu(\hat{y}\times\vec{H})\cdot\hat{n} = -j\omega\mu\hat{y}\cdot(\vec{H}\times\hat{n}) = j\omega\mu\hat{y}\cdot(\hat{n}\times\vec{H})\,. \tag{3.38}$$

Note that $\vec{E}\cdot\vec{E} = E_y E_y$. The vector, $\hat{n}$, is the unit normal pointing outward from region 1. Thus, for region 1, it can be seen that $\hat{n}\cdot\nabla E_{y1} = j\omega\mu\hat{y}\cdot(\hat{n}\times\vec{H}_1)$, and for region 2, $\hat{n}\cdot\nabla E_{y2} = j\omega\mu\hat{y}\cdot(\hat{n}\times\vec{H}_2)$. Assuming $\mu_1 = \mu_2$, subtracting the expression for region 2 from region 1 yields the boundary condition of Equation (3.33), $\hat{n}\times(\vec{H}_2 - \vec{H}_1) = 0$. It can therefore be said that $\hat{n}\cdot\nabla E_{y1} = \hat{n}\cdot\nabla E_{y2}$, or

$$\frac{\partial E_{y1}}{\partial n} = \frac{\partial E_{y2}}{\partial n}\,. \tag{3.39}$$

For the TM case, first note that $\hat{n}\times(\vec{H}_2 - \vec{H}_1) = 0$, $H_{y1} = H_{y2}$ at the interface. For the normal derivative, an analysis similar to that for the TE case is used. Taking $\vec{H} = H_y\hat{y} = \left|\vec{H}\right| e^{-j(\vec{k}\cdot\vec{r})}\hat{y}$, it can be seen that $\nabla H_y = -j\vec{k}H_y = -j(\vec{k}\cdot\hat{t})H_y\hat{t} - j(\vec{k}\cdot\hat{n})H_y\hat{n}$. Again, assuming time harmonic Maxwell's equations and the vector identity of Equation (3.34), the wave vector can be solved in terms of the fields, $\nabla\times\vec{H} = j\omega\varepsilon\vec{E} = -j\vec{k}\times\vec{H}$. By crossing both sides of the equation with the magnetic field, using Equation (3.34), and solving for the wave vector, this expression is obtained,

$$\vec{k} = \frac{\omega\varepsilon}{(\vec{H}\cdot\vec{H})}\vec{E}\times\vec{H}\,. \tag{3.40}$$

Using a similar argument similar to that for the TE case, the gradient and normal derivative for the TM magnetic field is solved.

$$\nabla H_y = -\frac{jH_y\omega\varepsilon}{(\vec{H}\cdot\vec{H})}[((\vec{E}\times\vec{H})\cdot\hat{t})\hat{t} + ((\vec{E}\times\vec{H})\cdot\hat{n})\hat{n}],$$

$$\nabla H_y = -\frac{jH_y\omega\varepsilon}{(\vec{H}\cdot\vec{H})}[\vec{H}\cdot(\hat{t}\times\vec{E})\hat{t} + \vec{H}\cdot(\hat{n}\times\vec{E})\hat{n}], \text{ and}$$

$$\hat{n}\cdot\nabla H_y = \frac{-j\omega\varepsilon H_y}{(\vec{H}\cdot\vec{H})}\vec{H}\cdot(\hat{n}\times\vec{E}) = -j\omega\varepsilon\hat{y}\cdot(\hat{n}\times\vec{E}). \quad (3.41)$$

Since $\hat{n}\times(\vec{E}_2 - \vec{E}_1) = 0$ at the interface, and $\varepsilon = \varepsilon_0 n_i^2$, where n_i are the indices of refraction of the indexed dielectric media, the normal derivatives have this relationship,

$$\frac{1}{n_1^2}\frac{\partial H_{y1}}{\partial n} = \frac{1}{n_2^2}\frac{\partial H_{y2}}{\partial n}. \quad (3.42)$$

Equations (3.39) and (3.42), along with the continuity of the fields across the boundary between regions 1 and 2, allow the integral equations for the TE fields at the surface of the boundary to be expressed as follows,

$$E_y(\vec{r}_b)\left(\frac{\alpha}{2\pi}\right) = E_{inc}(\vec{r}) + \oint_{Cauchy}[E_y(\vec{r}\,')\frac{\partial G_1(\vec{r},\vec{r}\,')}{\partial n} - G_1(\vec{r},\vec{r}\,')\frac{\partial E_y(\vec{r}\,')}{\partial n}]d\ell' \text{ and} \quad (3.43)$$

$$E_y(\vec{r}_b)\left(1-\frac{\alpha}{2\pi}\right) + \oint_{Cauchy}[E_y(\vec{r}\,')\frac{\partial G_2(\vec{r},\vec{r}\,')}{\partial n} - G_2(\vec{r},\vec{r}\,')\frac{\partial E_y(\vec{r}\,')}{\partial n}]d\ell' = 0. \quad (3.44)$$

For the TM case these expressions are used.

$$H_y(\vec{r}_b)\left(\frac{\alpha}{2\pi}\right) = H_{inc}(\vec{r}) + \oint_{Cauchy}[H_y(\vec{r}\,')\frac{\partial G_1(\vec{r},\vec{r}\,')}{\partial n} - n_1^2 G_1(\vec{r},\vec{r}\,')\frac{\partial H'_y(\vec{r}\,')}{\partial n}]d\ell' \text{ and} \quad (3.45)$$

$$H_y(\bar{r}_b)\left(1-\frac{\alpha}{2\pi}\right)+\oint_{Cauchy}[H_y(\bar{r}')\frac{\partial G_2(\bar{r},\bar{r}')}{\partial n}-n_2^2 G_2(\bar{r},\bar{r}')\frac{\partial H'_y(\bar{r}')}{\partial n}]d\ell'=0. \tag{3.46}$$

In Equations (3.45) and (3.46), this substitution for the normal derivatives at the boundary has been made.

$$\frac{\partial H'_y(\bar{r}')}{\partial n}=\frac{1}{n_1^2}\frac{\partial H_{y1}(\bar{r}')}{\partial n}=\frac{1}{n_2^2}\frac{\partial H_{y2}(\bar{r}')}{\partial n}.$$

The primed position coordinates denote an integration along the DOE contour/ dielectric interface, with the condition, $\bar{r}'=\bar{r}_b$, denoting a singular point on the boundary. $E_{inc}(\bar{r})$ and $H_{inc}(\bar{r})$ must be known at the boundary. Finding the fields everywhere in space requires that the fields and their normal derivatives be solved at the boundary and subsequently re-inserted into the following integral equations, general for all space, as functions of the primed coordinates.

$$E_{y1}(\bar{r})=E_{inc}(\bar{r})+\oint_C[E_{y1}(\bar{r}')\frac{\partial G_1(\bar{r},\bar{r}')}{\partial n}-G_1(\bar{r},\bar{r}')\frac{\partial E_{y1}(\bar{r}')}{\partial n}]d\ell',$$

$$E_{y2}(\bar{r})=-\oint_C[E_{y2}(\bar{r}')\frac{\partial G_2(\bar{r},\bar{r}')}{\partial n}-G_2(\bar{r},\bar{r}')\frac{\partial E_{y2}(\bar{r}')}{\partial n}]d\ell',$$

$$H_{y1}(\bar{r})=H_{inc}(\bar{r})+\oint_C[H_{y1}(\bar{r}')\frac{\partial G_1(\bar{r},\bar{r}')}{\partial n}-G_1(\bar{r},\bar{r}')\frac{\partial H_{y1}(\bar{r}')}{\partial n}]d\ell', \text{ and}$$

$$H_{y2}(\bar{r})=-\oint_C[H_{y2}(\bar{r}')\frac{\partial G_2(\bar{r},\bar{r}')}{\partial n}-G_2(\bar{r},\bar{r}')\frac{\partial H_{y2}(\bar{r}')}{\partial n}]d\ell'. \tag{3.47}$$

Maxwell's equations can be used to calculate the other field components, i.e., the H_x and H_z components for the TE case and the E_x and E_z components for the TM case.

3.2.2 Application of rigorous diffraction theory to BEM computational procedure

Determination of the fields and their normal derivatives requires numerical techniques, since analytical solutions only exist for a limited number of problems. It is necessary, therefore, to present the numerical method, BEM, that was used to predict the performance of the 1-2 beamfanners. This method is implemented by dividing the DOE boundary into segmented intervals. These intervals have indexed field and normal derivative values that serve as basis states for the total field solution along the DOE boundary. The procedure outlined below, also known as the point co-location method, couples every point on the DOE contour with each and every other point on the contour through the Green's functions and their normal derivatives.

N sample points are taken along the interface such that the TE and TM fields and their normal derivatives can be expressed as the sum of two products of an amplitude and interpolation function.

$$E_y[r'(\xi)] = \sum_{n=1}^{N} \hat{E}_{yn}(\xi) = \sum_{n=1}^{N} \hat{E}_n \phi_1(\xi) + \hat{E}_{n+1}\phi_2(\xi) \,,$$

$$\frac{\partial E_y[r'(\xi)]}{\partial n} = \sum_{n=1}^{N} \hat{Q}_{yn}(\xi) = \sum_{n=1}^{N} \hat{Q}_n \phi_1(\xi) + \hat{Q}_{n+1}\phi_2(\xi) \,,$$

$$H_y[r'(\xi)] = \sum_{n=1}^{N} \hat{H}_{yn}(\xi) = \sum_{n=1}^{N} \hat{H}_n \phi_1(\xi) + \hat{H}_{n+1}\phi_2(\xi) \text{ , and}$$

$$\frac{\partial H'_y[r'(\xi)]}{\partial n} = \sum_{n=1}^{N} \hat{R}_{yn}(\xi) = \sum_{n=1}^{N} \hat{R}_n \phi_1(\xi) + \hat{R}_{n+1}\phi_2(\xi) \,. \tag{3.48}$$

The two linear interpolation functions in Equation (3.48) are next defined as

$$\phi_1 = \frac{1-\xi}{2} \text{ and}$$

$$\phi_2 = \frac{1+\xi}{2}. \quad (3.49)$$

The variable ξ is defined over the interval [-1,1]. The interpolation functions of Equation (3.49) allow a coordinate transformation that enables the field amplitudes at the sampled points to be uncoupled from the integrals of Equation (3.47) [37]. The position coordinates along the boundary transform in this manner.

$$\hat{x}_n(\xi) = x_n\phi_1(\xi) + x_{n+1}\phi_2(\xi) \text{ and}$$

$$\hat{z}_n(\xi) = z_n\phi_1(\xi) + z_{n+1}\phi_2(\xi). \quad (3.50)$$

x_n , x_{n+1}, z_n, and z_{n+1} represent adjacent sample points on the DOE boundary, and $\hat{x}_n(\xi)$ and $\hat{z}_n(\xi)$ are interpolated coordinate values between the sample points. The sample indices, n, not to be confused with refractive indices, are numbered in a sequential counterclockwise fashion along the boundary. It is possible to characterize Equation (3.47) as two equations in 2N unknowns for both the TE and TM cases. To generate the necessary 2N equations for the 2N unknowns, an inner product between both sides of Equation (3.47) is taken with a set of N weighting functions. These weighting functions are Dirac-delta functions.

$$\delta_m = \delta[\vec{r}_b(\xi) - \vec{r}\,'_m] = 1,\ \vec{r}_b(\xi) = \vec{r}\,'_m$$
$$= 0, \text{ otherwise.}$$

The vectors, $\vec{r}\,'_m$, form a set of N position vectors along the DOE contour. With the field amplitudes uncoupled from integrands, and the proper number of equations and unknowns,

Equations (3.43), (3.44), (3.45), and (3.46) can be put in the form of a matrix equation for the TE and TM cases . They take the following form,

$$\begin{bmatrix} \text{Coupling} \\ \text{Matrix} \end{bmatrix}_{nm} \begin{bmatrix} \text{Output} \\ \text{Vector} \end{bmatrix}_{m} = \begin{bmatrix} \text{Input} \\ \text{Vector} \end{bmatrix}_{m} . \tag{3.51}$$

Specifically, this equation looks like

$$\text{TE} \rightarrow \begin{bmatrix} Z1_{n,m} & Y1_{n,m} \\ Z2_{n,m} & -Y2_{n,m} \end{bmatrix} \begin{bmatrix} E_{ym} \\ Q_{ym} \end{bmatrix} = \begin{bmatrix} E_m^{inc} \\ 0 \end{bmatrix} \text{ and} \tag{3.52}$$

$$\text{TM} \rightarrow \begin{bmatrix} Z1_{n,m} & n_1^2 Y1_{n,m} \\ Z2_{n,m} & -n_2^2 Y2_{n,m} \end{bmatrix} \begin{bmatrix} H_{ym} \\ R_{ym} \end{bmatrix} = \begin{bmatrix} H_m^{inc} \\ 0 \end{bmatrix} . \tag{3.53}$$

In these matrix representations, the n index represents an interpolated point, and the m indexes all sample points along the boundary that act on n. The incident fields must be known at the sample points along the boundary. To avoid confusion between indexed points and indices of refraction for the TM case, Equation (3.53), n_1 and n_2 are the indices of refraction for media 1 and 2 respectively. The Y and Z expressions are N×N matrices, which are concatenated to form the 2N×2N coupling matrix. The input and output vectors are of dimension 1×2N, where N is the number of sample points along the DOE contour. H_{ym} and R_{ym} are both 1×N vectors that are concatenated to form the 1×2N output vector. H_m^{inc} and the 1×N null vector similarly form the 1×2N input vector. To solve for the output vector, it is straightforward to perform a matrix inversion on a computer with MATLAB software for the following expression,

$$\begin{bmatrix}\text{Coupling}\\ \text{Matrix}\end{bmatrix}_{nm}^{-1}\begin{bmatrix}\text{Input}\\ \text{Vector}\end{bmatrix}_{m}=\begin{bmatrix}\text{Output}\\ \text{Vector}\end{bmatrix}_{m}. \tag{3.54}$$

The Y and Z matrices, which are the uncoupled field representations of Equations (3.43), (3.44), (3.45), and (3.46), are given next.

$$Z1=\left(\frac{\alpha}{2\pi}\right)\delta_{mn}$$

$$-\int_{-1}^{1}\left\{\frac{\Delta l_n}{2}\phi_1(\xi)\frac{\partial G_1[\vec{r}\,'(\hat{x}_n,\hat{y}_n),\vec{r}_m]}{\partial n}+\frac{\Delta l_{n-1}}{2}\phi_2(\xi)\frac{\partial G_1[\vec{r}\,'(\hat{x}_{n-1},\hat{y}_{n-1}),\vec{r}_m]}{\partial n}\right\}d\xi, \tag{3.55}$$

$$Y1=\int_{-1}^{1}\left\{\frac{\Delta l_n}{2}\phi_1(\xi)G_1[\vec{r}\,'(\hat{x}_n,\hat{y}_n),\vec{r}_m]+\frac{\Delta l_{n-1}}{2}\phi_2(\xi)G_1[\vec{r}\,'(\hat{x}_{n-1},\hat{y}_{n-1}),\vec{r}_m]\right\}d\xi, \tag{3.56}$$

$$Z2=\left(1-\frac{\alpha}{2\pi}\right)\delta_{mn}$$

$$+\int_{-1}^{1}\left\{\frac{\Delta l_n}{2}\phi_1(\xi)\frac{\partial G_2[\vec{r}\,'(\hat{x}_n,\hat{y}_n),\vec{r}_m]}{\partial n}+\frac{\Delta l_{n-1}}{2}\phi_2(\xi)\frac{\partial G_2[\vec{r}\,'(\hat{x}_{n-1},\hat{y}_{n-1}),\vec{r}_m]}{\partial n}\right\}d\xi, \text{ and} \tag{3.57}$$

$$Y2=\int_{-1}^{1}\left\{\frac{\Delta l_n}{2}\phi_1(\xi)G_2[\vec{r}\,'(\hat{x}_n,\hat{y}_n),\vec{r}_m]+\frac{\Delta l_{n-1}}{2}\phi_2(\xi)G_2[\vec{r}\,'(\hat{x}_{n-1},\hat{y}_{n-1}),\vec{r}_m]\right\}d\xi. \tag{3.58}$$

Here, Δl_n is the length of the corresponding nth line segment on the contour between sample points and $d\xi=\frac{2d\ell'}{\Delta l_n}$. For the purpose of numerical integration of Equations (3.55), (3.56), (3.57), and (3.58), the ξ interval is divided into a finite number of evenly spaced points. A greater number of sample and interval points yield solutions of greater accuracy. Once the matrix inversion is performed, and solutions for the fields and their normal derivatives at the boundary

are obtained, these solutions become the surface distribution terms from which the fields in all space can be calculated using Equation (3.47) [38].

3.3 Design and positioning of the Nichols and UAH arrays

Two beamfanner designs were developed. The first, a 1-4 beamfanner array, was to be integrated with the IR camera focal plane array for Nichols Research Corporation. It proved impossible to successfully fabricate but did possess value in terms of useful experience gained in the fabrication attempt. The second, the UAH array, was redesigned with larger feature sizes in an effort to allow for greater ease of fabrication both from the standpoint of photolithography and the subsequent reactive ion etching process. The UAH array consists not only of a 256×256 1-4 beamfanner array similar to the original Nichols design, but it has, in addition, a group of 1-2 beamfanner arrays. These later arrays serve as a test of concept, since the IASA and BEM techniques were used to design 1-2 beamfanners. In addition to the 1-2 beamfanner arrays, there is a set of small 5×5 1-4 beamfanner arrays that correspond to specific positions on the large 256×256 array. The smaller sets of arrays have the added advantage of being easy to test with an IR lens system and camera, since they correspond to known positions in the large array, which would otherwise be difficult to locate.

Computer code for design and testing of the beamfanner arrays was written in Matlab. The codes employed for the design of the beamfanner arrays were named ‘doe_fab’ and ‘dvcmskrd’. ‘Doe_fab’, given in Appendix A, was written and subsequently often modified by Steve Mellin. It served in the design of both the Nichols and UAH arrays. ‘Dvcmskred’ was written by this author and was used in conjunction with ‘Doe_fab’ to design the UAH array. Both codes organized etch-depth data so that Canyon Materials and MEMS Optical could fabricate the requested grayscale masks. ‘BEM_off_axis’, given in Appendix A, is the name of

the program written by Steve Mellin to test the beamfanner designs. The output of this program can be viewed in Figures 3.13-3.28. 'Snr2d' is the program written by Mellin and this author to calculate diffraction efficiency and signal-to-noise ratio as presented later in Tables 3.1 and 3.2.

The Nichols array was to be integrated with the IR camera focal plane array being developed in conjunction with Nichols Research Corporation. It was developed by Steve Mellin using IASA, tested with BEM, and generalized to a three-dimensional 1-4 beamfanner design. The first step was to develop a working 1-2 beamfanner design with 256 phase levels, equally spaced, and lateral feature sizes with an area of 1 square micron. This design was done with the scalar algorithm, IASA, to develop a DOE profile for the case of on-axis plane wave illumination. This profile was then tested with the rigorous method, BEM. TE, TM, and scalar plots of the irradiance in the detector plane are in extremely good agreement, as shown in Figure 3.11. One of the advantages of IASA, mentioned previously in the first section of this chapter, is that it is more computationally efficient than rigorous methods. As mentioned previously, IASA seems to test very well with rigorous theory such as BEM and FDTD analysis for some cases [39].

When the desired diffraction pattern was confirmed with BEM, the design of the beamfanner was modified so that the lateral feature sizes were a combination of 2-micron and 3-micron square regions. This was necessary since Canyon Materials, who supplied the grayscale HEBS mask, could not form mask regions with areas smaller than 2 square microns. The modified design was re-evaluated with BEM and found to be satisfactory.

In addition, the design had to take into account the combined effects off-axis illumination and converging spherical illumination. For the diffracted IR light to be directed into the polarizer apertures described in the introduction, a modification of the basic plane wave design was necessary. This modification required that the converging spherical wave fronts be flattened, and it also required that the direction of propagation be turned parallel to the optical axis. Tilt and curvature were built into the beamfanner design to satisfy these requirements. Figure 3.7 illustrates the illumination of a DOE surface using a converging spherical wave. Note that the

input side of the DOE/beamfanner surface, which consists of the etched features of the beamfanner, is not the point of focus. Rather, the output side of the beamfanner serves as the focal and detector plane, and a wave front of finite spatial extent is sampled over the input side.

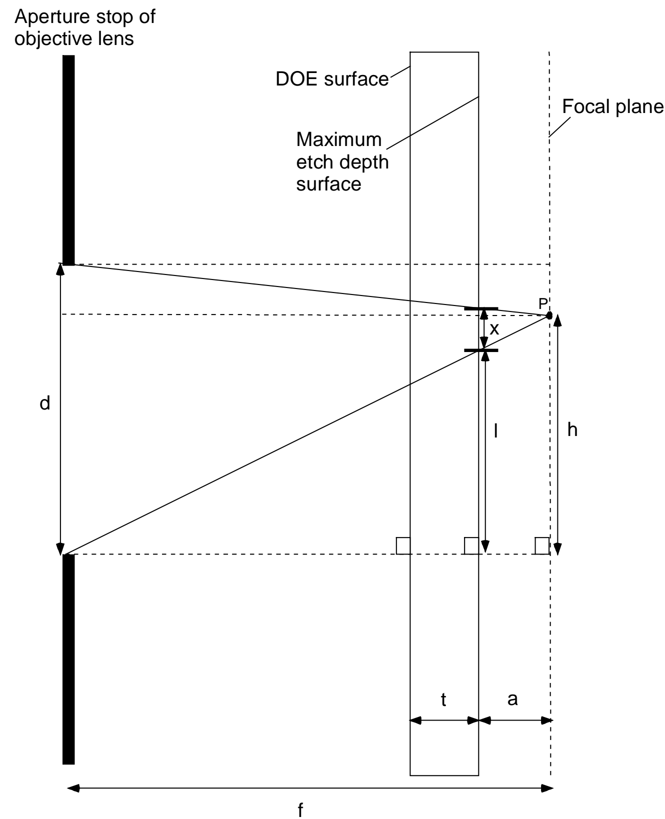

Figure 3.6 Scheme for the spherical illumination of the beamfanner with maximum etch-depth on the incident surface, t, and incident fields sampled over a finite interval, x, with a virtual focus on the focal plane at point P, which is a distance, a, from the incident surface.

For each of 128 individual 1-2 beamfanners, progressively corresponding to points representing on-axis illumination outward to a distance 6.4 mm off-axis, a corresponding adjustment for tilt and curvature had to be added to the plane wave DOE design shown later in Figure 3.12.

Since the scalar method, IASA, yielded effective 1-2 beamfanner designs, 1-4 beamfanners were generated by cross-feature depth addition of the 1-2 beamfanners. This represents an outer product of feature phases, and is demonstrated in Figure 3.7.

1-2 Beamfanner Etch Levels (Gray)

	E1	E2	E3	E4	E5	E6
E1	E1+E1	E2+E1	E3+E1	E4+E1	E5+E1	E6+E1
E2	E1+E2	E2+E2	E3+E2	E4+E2	E5+E2	E6+E2
E3	E1+E3	E2+E3	E3+E3	E4+E3	E5+E3	E6+E3
E4	E1+E4	E2+E4	E3+E4	E4+E4	E5+E4	E6+E4
E5	E1+E5	E2+E5	E3+E5	E4+E5	E5+E5	E6+E5
E6	E1+E6	E2+E6	E3+E6	E4+E6	E5+E6	E6+E6

1-4 Beamfanner Etch Levels (White)

Figure 3.7 Addition of phase levels/etch-depths to fabricate the 1-4 beamfanner from 1-2 beamfanners.

Note that Figure 3.7, which is a simplified but direct analog to the lower right hand corner of the 1-4 beamfanner array, is a three-dimensional 6×6 feature array generated from a 6×1 two-dimensional feature array. The development of the 1-4 beamfanner design appears to assume

that the Fresnel approximation is valid, and orthogonal field solutions are separable [40], [41]. This is not truly the case, since this approximation requires features to be much larger than the wavelength of the incident light. Time constraints and computer memory issues required that this design shortcut be taken.

Mellin's 2-3-micron feature design yields a quadrant dimension of 2944×2944 features, which represents 23×1 features per individual 1-2 beamfanner and 23×23 features per individual 1-4 beamfanner. The other three quadrants are easily generated. The upper right is reflection-symmetric to the lower right about a horizontal axis, and the upper left and lower left are reflection-symmetric to the upper right and lower right about a vertical axis. The latter 5-micron feature design by this author has a quadrant size of 1280×1280 features, with 10×1 features per individual 1-2 beamfanner and 10×10 features per individual 1-4 beamfanner.

Two possible approaches can be considered for the design of beamfanners with larger lateral feature sizes, fewer phase levels, or both. The first is to run the IASA algorithm, using larger lateral feature sizes and a reduced number of phase levels, followed by rigorous performance testing using BEM. Since this technique was already employed to develop an optimal 1-micron feature size, 256 phase level design for the 1-2 beamfanners, it made sense to modify this design directly through a second approach. This second approach is a partition and phase level re-sampling technique. It is accomplished by finding the average of the depths for adjacent smaller features over a desired larger lateral feature extent in the basic 1-2 beamfanner design. This is shown pictorially in Figure 3.8.

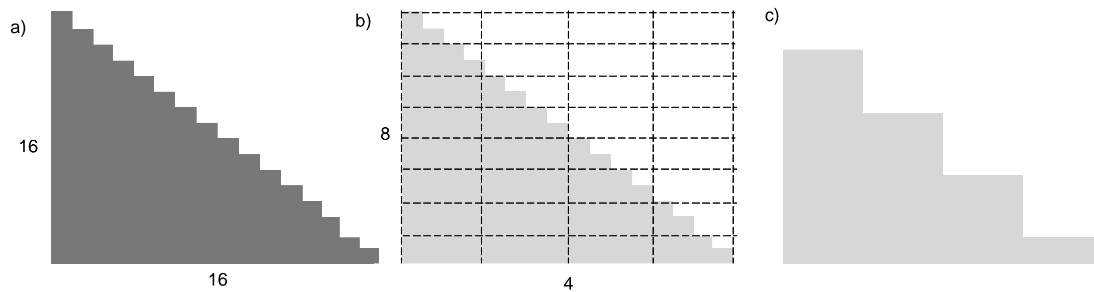

Figure 3.8 A sixteen lateral feature, 16 phase level DOE, a), is re-sampled, b), to have a selection of 8 phase levels and 4 lateral feature sizes, c). Note that the choice of 4 lateral features reduces the number of available phase levels to 4 in this example.

This average is then rounded to the nearest depth allowed in a reduced number of evenly spaced phase level values. Figure 3.8 illustrates this process for a DOE profile with 16 lateral partitions and 16 phase levels that is converted to a profile with 4 lateral partitions and 8 phase levels. This is a simplification of what was done with the 50 lateral partition, 256 phase level DOE that represents the basic design for an individual 1-2 beamfanner. There is a tradeoff between larger feature sizes and device performance, since smaller feature sizes better approximate the smooth contours of an ideal device. After the beamfanner was redesigned, BEM was used to determine if the diffracted intensity pattern exhibited the desired beam splitting characteristics. This method was used to design the 2-3-micron feature, 256 phase level beamfanner array for Nichols, and it was later used to design beamfanner arrays with 8, 16, 32, and 64 phase levels in combination with lateral feature sizes of 5, 6, 7, and 10 microns for the UAH array.

Designing and constructing beamfanners with larger features permits the exploration of two important avenues of research. First of all, it is possible to compare performance of the larger feature devices with the smaller feature devices. Secondly, the larger features allow easier measurements of etch-depth with the use of a profilometer. These two items can yield important information whether or not the 1-4 beamfanner focal plane array tests successfully. If the

1-4 arrays won't work, the 1-2 arrays might yet possibly perform well enough to yield good test results, and can be compared as a function of their lateral feature sizes and phase quantization. Reliable etch-depth measurements are necessary to determine the repeatability of the fabrication process and how etch selectivity is dependent on etch-depth.

3.3.1 Nichols beamfanner array description

Both the Nichols beamfanner array, where the photolithographic process is achieved with contact exposure through a HEBS mask manufactured by Canyon Materials in San Diego, California, and the UAH beamfanner array, where the photolithography is a proprietary process of MEMS-Optical in Huntsville, Alabama, have as their centerpiece a 256×256 1-4 beamfanner array. The Nichols version of this main array, as mentioned previously, has 2-3-micron lateral feature sizes. This array is the focal plane element to be integrated with the infrared camera system. The centers of these 12.8 mm square arrays are both located at the midpoint of the horizontal axis shared by a pair of alignment marks. These alignment marks are designed both to align other focal plane elements, the polarizer arrays and the waveplate arrays, to the beamfanner arrays. In the case of the UAH array, there are also marks, described in Chapter 6, designed to align a mask in a stepper to the silicon substrate during the photolithographic process.

The Nichols array also has five sets of 5×5 arrays that between them possess features that correspond to all 256 possible phase levels/etch-depths. These arrays are in a row directly below the focal plane array. All 25 beamfanners in each individual set are duplicates. Adjacent to each 5×5 array is a single beamfanner that is a duplicate of the individual beamfanners in the 5×5 array. These smaller arrays and individual beamfanners could have served as test cases for beamfanner performance if the fabrication had been successful. They did, however, yield insight that led to the development of modifications later employed in the UAH array, since it was easy to examine the effects of photolithographic and etching processes on the feature fidelity of these

smaller, isolated, stand-alone arrays. These modifications will be covered later. The Nichols array also has twenty seven 0.2×0.8 mm rectangular pads corresponding to phase level 0 (shallowest etch/highest optical density) through phase level 250 in increments of 10, plus level 255 (deepest etch/lowest optical density). They are arranged in a row above the focal plane array. These pads are useful for etch selectivity calibration. The configuration of the Nichols array is presented below in Figure 3.9.

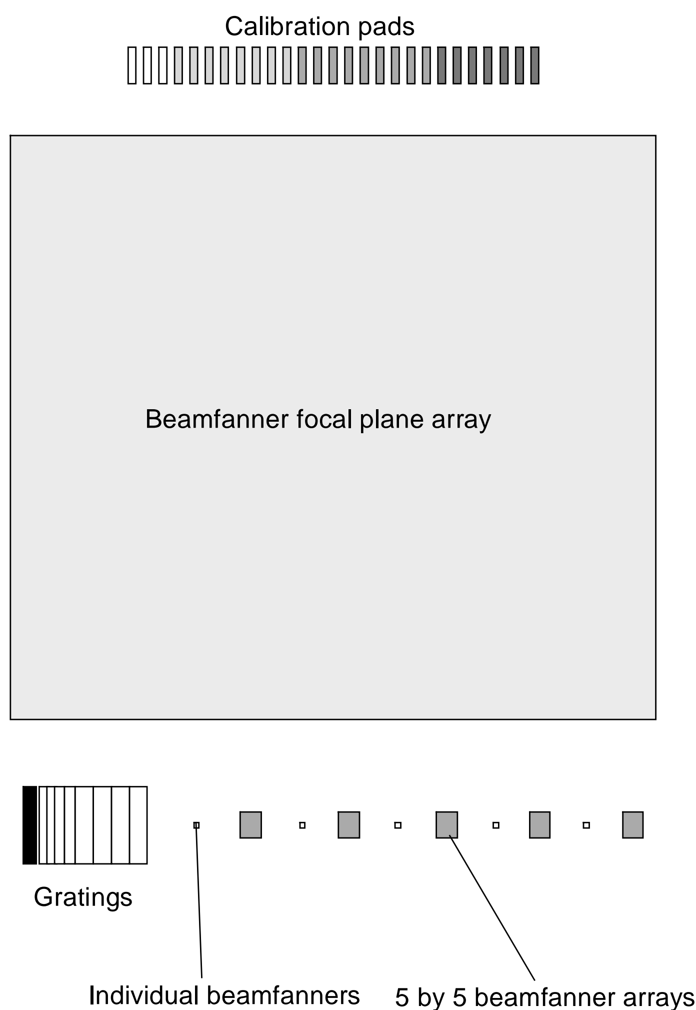

Figure 3.9 A view of the Nichols beamfanner array.

Although this first array was developed using a calibration curve relating optical densities to etch-depths from pads on a test HEBS mask, it was deemed prudent to have a set of pads more closely spaced in optical density for future calibrations. There are also gratings, in groups of 4, with spatial periods of 10, 20, 50, 100, and 400 microns. They are positioned at the end of the row of the smaller 1-4 beamfanner arrays. As with the small beamfanner arrays, it was possible to draw conclusions regarding the fidelity of photolithographic and etching processes from their effects on the small step features of these gratings.

3.3.2 UAH beamfanner array description

The UAH array has, as mentioned, the main 256×256 array, but it has been modified with lateral feature sizes of 5 square microns and 64 phase levels/etch-depths. Beneath the left half of the main array are located 64 5×5 arrays of 1-4 beamfanners. To the right of the main array are located 48 1×5 1-2 beamfanner arrays. As can be seen in Figure 3.10, the 1-4 5×5 arrays are grouped in 4×4 squares.

Each of the 16 5×5 1-4 beamfanner arrays in these squares correspond to a specific lateral feature size and number of possible phase levels/etch-depths. The first through fourth columns of 5×5 arrays have 5, 6, 7, and 10 square micron lateral feature sizes respectively. The first through fourth rows have 8, 16, 32, and 64 phase levels respectively. Each of these squares corresponds to one of four pixels on the main array. Columns c1, c2, c3, and c4 correspond to the center-pixel of the main array. Columns m1, m2, m3, and m4 correspond to the middle-pixel of the main array. Columns s1, s2, s3, and s4 correspond to the side-pixels of the main array. Columns co1, co2, co3, and co4 correspond to the corner pixel of the main array. The center-pixel has its left and bottom sides aligned to the vertical and horizontal axes of the main array respectively. The middle-pixel has its right side aligned to the vertical axis 3.2 mm from the center and bottom to

the horizontal axis of the main array. The side-pixel has its right side aligned to the right side of the main array and bottom aligned to the horizontal axis. The corner pixel is located at the lower right hand corner of the main array.

The group of 1-2 beamfanner arrays are divided into 3 4×4 rectangles of 1×5 1-2 beamfanner arrays. As can be seen in Figure 3.10, the top 4×4 rectangle represents the center- pixel, the middle 4×4 rectangle represents the middle-pixel, and the bottom 4×4 rectangle represents the side-pixel.

Figure 3.10 View of the UAH beamfanner array, where scan lengths represent the number of lateral features in the width of a single beamfanner.

Columns p10, p8, p7, and p5 correspond to 5, 6, 7, and 8-micron horizontal feature sizes (the 1-2 beamfanners each span 300 microns in the vertical direction). Like the 1-4 beamfanner arrays, the first through fourth rows in each 4×4 rectangle represent cases of 8, 16. 32, and 64 phase levels/etch-depths. The individual 1-2 beamfanners are adjacently grouped into 1×5 arrays for the purpose of examining optical cross talk during testing. Since the 1-2 beamfanners are modeled with the assumption of cylindrically converging illumination, the 750-micron vertical dimension was incorporated in the design.

As stated before, the purpose of the larger feature sizes is to yield a beamfanner where the photolithographic and etch processes are able to transfer these features with a high level of fidelity, i.e., the 2-3-micron feature size design proved impossible to fabricate as even a reasonable approximation of the design parameters with available tools and methods. The 2-3-micron features could not be patterned into photoresist without diffractive blurring of the feature edges, and the etch process further deteriorated the fidelity of these features through edge rounding. However, the higher fidelity sought in the UAH array, based on larger feature sizes, comes at a cost in device performance. Device performance will be discussed in the final section. Details of the photolithographic and etch processes will be covered in the next chapter.

The 1-2 beamfanners, as previously mentioned, provide the only accurate means by which to test the actual device performance against the performance predicted by BEM. The original 2-3-micron feature size design did not include 1-2 beamfanners, but the 5-micron-plus feature size design of the second beamfanner array series includes 48 1×5 arrays of 1-2 beamfanners. These 48 are divided into three sets of 16 with each set representing an on-axis pixel, a pixel located midway between the on-axis pixel and side of the main array, and a side-pixel. Again, there are sixteen arrays, since each corresponds to one of sixteen possible combinations of phase levels/lateral feature sizes. Note that the corresponding 1-4 beamfanners,

center, middle, and side, were generated from the addition of the center 1-2 beamfanner design with the center, middle, and side 1-2 beamfanner designs respectively.

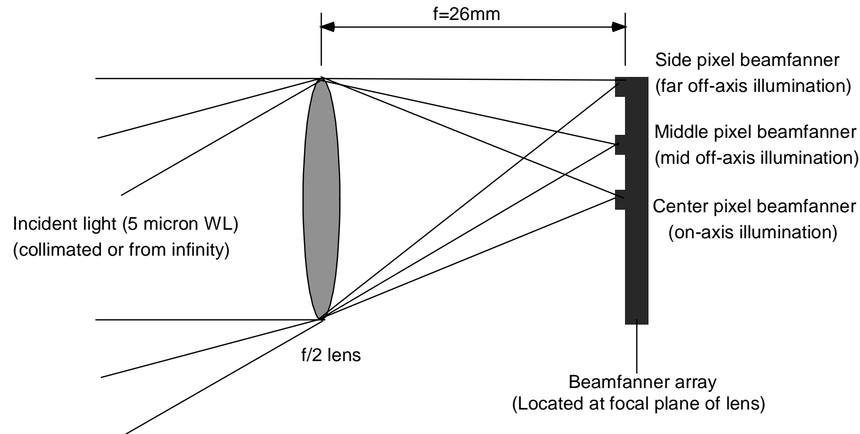

Figure 3.11 Center-pixel (on-axis) illumination and middle and side-pixel (off-axis) illumination of beamfanner focal plane array.

As shown in Figure 3.11, these 1-2 beamfanners were designed for illumination by 5-micron light through a cylindrical f/2 lens with a focal length of 26 millimeters. The long axis of the beamfanners must be aligned parallel to the long axis of the cylindrical lens, and these axes face out of the page in Figure 3.11.

The choice of center, middle, and side-pixel cases is motivated by a need to examine the performance of beamfanners over a wide range of positions while at the same time keeping the number of case studies to a minimum. Center, middle, and side cases offer the advantage of examining performance over the horizontal width of a two-dimensional analog of the main beamfanner array. The three cases and their predicted performance, as well as trends in performance, are examined in the next section. Keep in mind that these cases are ideal designs,

and fabrication to within the exact specification of the designs is difficult, though not as much so as for the 2-3-micron feature size arrays.

3.4 BEM performance simulation of beamfanners

For the purposes of beamfanner analysis, there are two important factors that must be addressed. First of all, an ideal 1-2 beamfanner will divide light evenly between two intensity maxima. Figures 3.12-3.29 in Section 3.4.1 address this issue. Secondly, an ideal 1-2 beamfanner will direct all of the light into both of the desired 15-micron apertures that are spaced 25 microns center-to-center about the middle of the beamfanner. Tables 3.1 and 3.2 quantify this property in terms of a diffraction efficiency and signal-to-noise ratio defined in Section 3.4.2.

3.4.1 Analysis of 1-2 beamfanner irradiance as a function of detector plane position

The actual symmetry of the beam splitting about the center of the beamfanners is of paramount importance, since they are intended to split the incoming radiation into two separate and equal beams. Since TE and TM illumination were examined separately for the BEM analysis, separate plots of these polarizations can yield insight into whether or not they produce similar flux profiles in the detector plane.

The closest approximation of an ideal device, Figure 3.12, comes very close to achieving these two conditions, according to BEM. The 2-3-micron lateral feature sizes of Mellin's design also demonstrate advantageous performance according to BEM analysis. Figure 3.12, it should be noted, is the case for 1-micron features, 256 phase levels, and plane wave illumination. Figure 3.13 also considers 1-micron features and 256 phase levels, but shows device profiles and performance for center, middle, and side-pixel cases, where off-axis spherical illumination is

considered. These cases also come very close to achieving the flux symmetry condition and balance between the TE and TM detector plane irradiance.

Next presented are the plotted results of BEM analysis on the 48 1-2 beamfanners that have been redesigned with larger lateral feature sizes and fewer etch-depths/phase levels. They correspond to the arrays in columns p10, p8, p7, and p5 in Figure 3.10. Beamfanner design profile and irradiance plots for the 1-2 beamfanners on the UAH array, given in Figures 3.14 through 3.29, are given below. Figures 3.14-3.17 show the 5-micron lateral feature size case, Figures 3.18-3.21 show the 6-micron lateral feature size case, Figures 3.22-3.25 show the 7-micron lateral feature size case, and Figures 3.26-3.29 show the 10-micron lateral feature size case. Each group of four contains the 8, 16, 32, and 64 phase level subset of the specific lateral feature size case. On each individual figure, from top to bottom, the center-pixel, middle-pixel, and side-pixel cases are plotted. The plots on the left of each diagram show the irradiance, or the Poynting flux, defined as $\bar{S} = \mathrm{Re}(\bar{E} \times \bar{H})$, as a function of position in the detector plane. As mentioned previously, this detector plane is located 340 microns from the beamfanner, with its x=0 position corresponding to the x=0 position on the plot of the beamfanner profile to the right. The plots on the right are the actual 1-2 beamfanner design profiles as they would appear ideally etched in silicon.

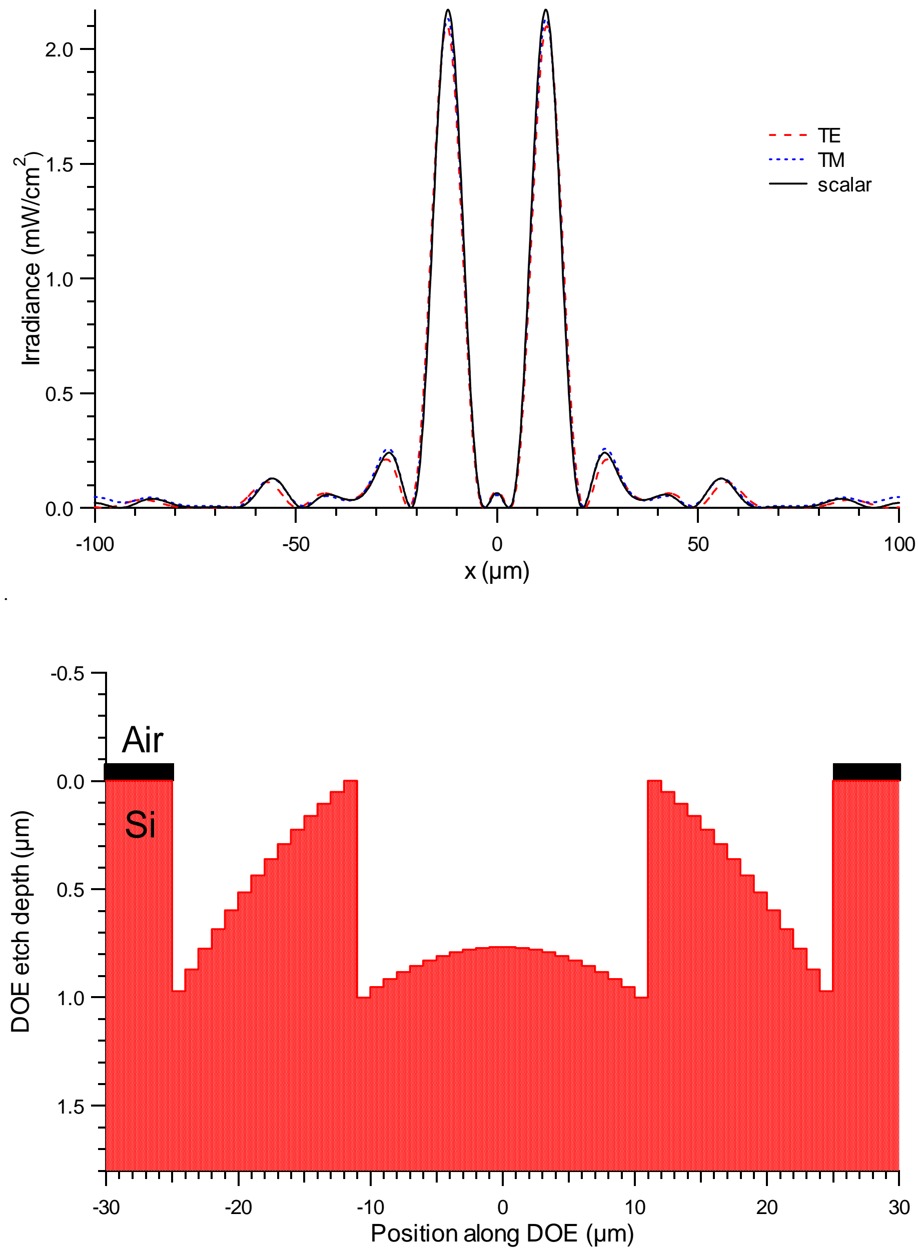

Figure 3.12 One-micron lateral feature size, 256 phase level 1-2 beamfanner (bottom) designed for plane wave illumination with corresponding irradiance pattern in focal plane (top).

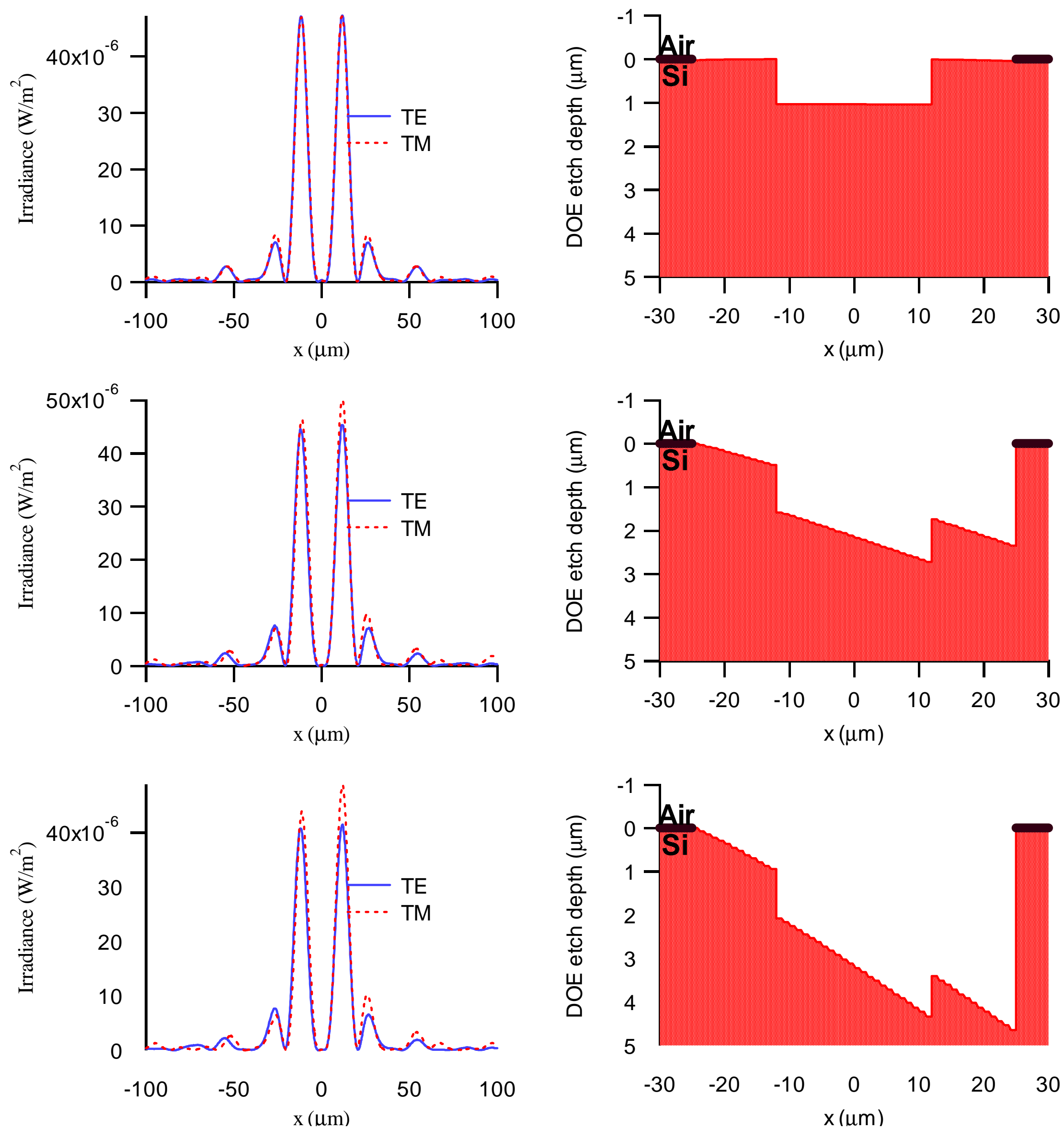

Figure 3.13 From top to bottom: irradiance and DOE profile for center, middle, and side-pixel 1-2 beamfanners for the 1-micron lateral feature size, 256 phase level case.

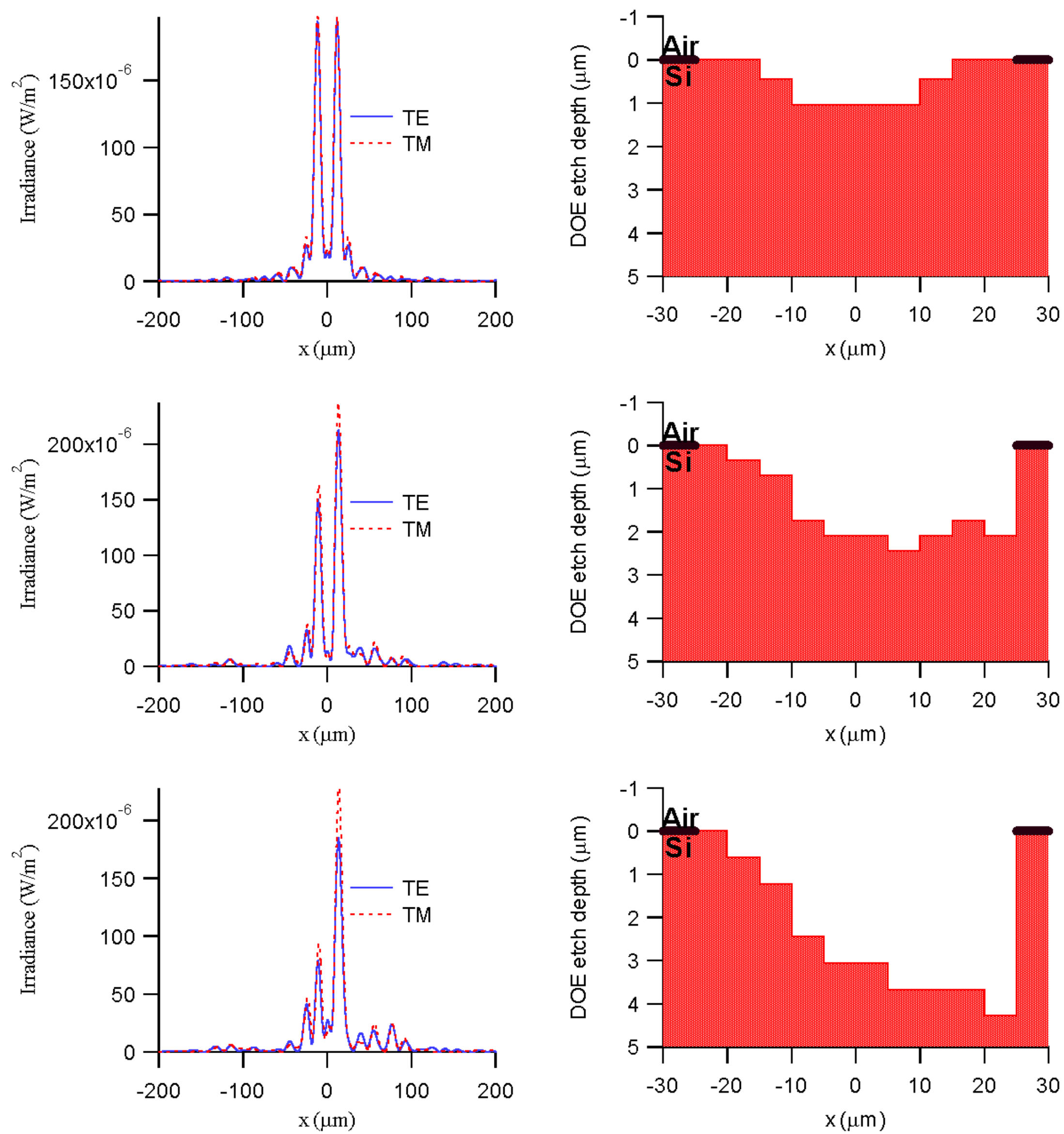

Figure 3.14 From top to bottom: irradiance and DOE profile for center, middle, and side-pixel 1-2 beamfanners for the 5-micron lateral feature size, 8 phase level case.

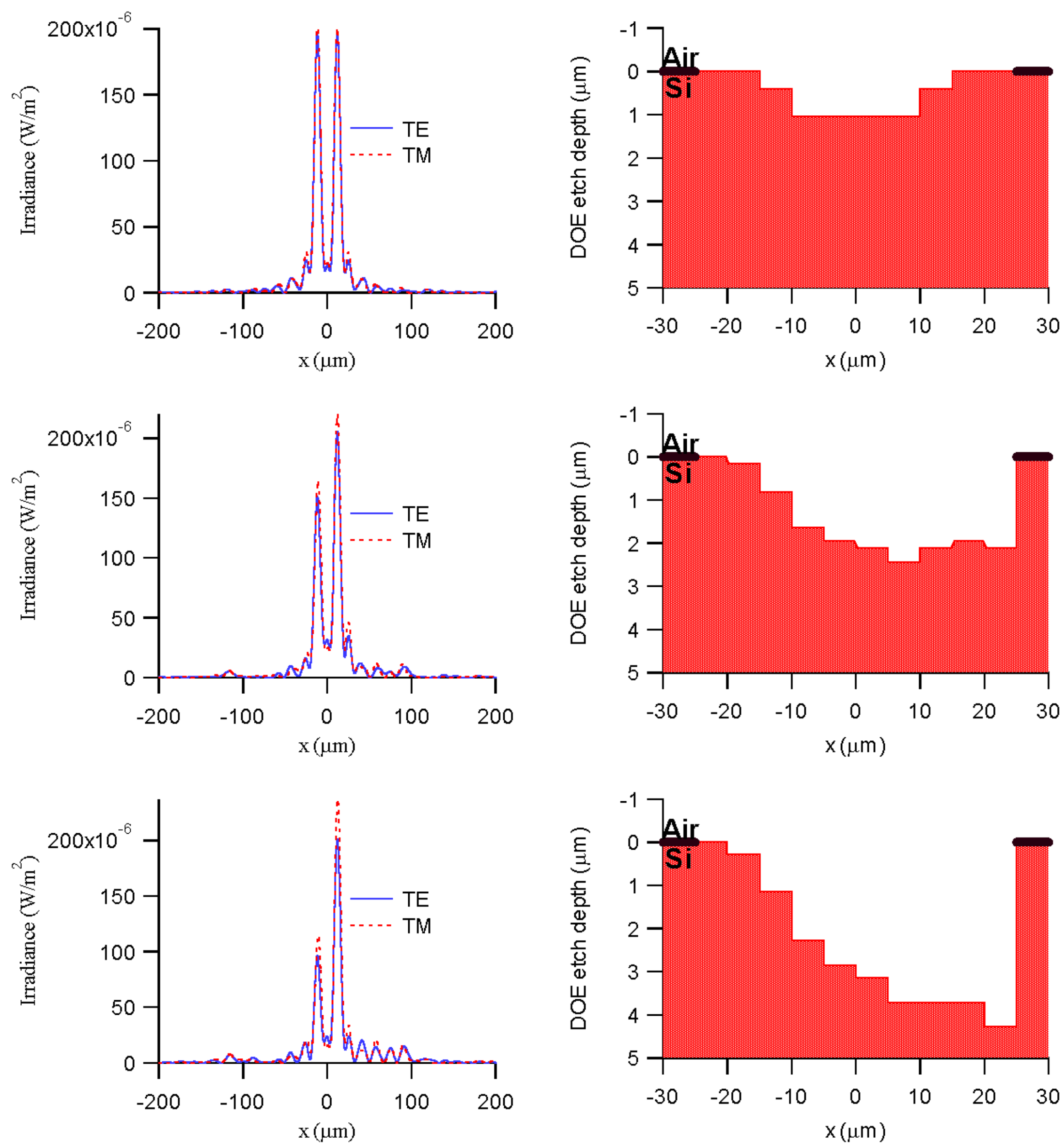

Figure 3.15 From top to bottom: irradiance and DOE profile for center, middle, and side-pixel 1-2 beamfanners for the 5-micron lateral feature size, 16 phase level case.

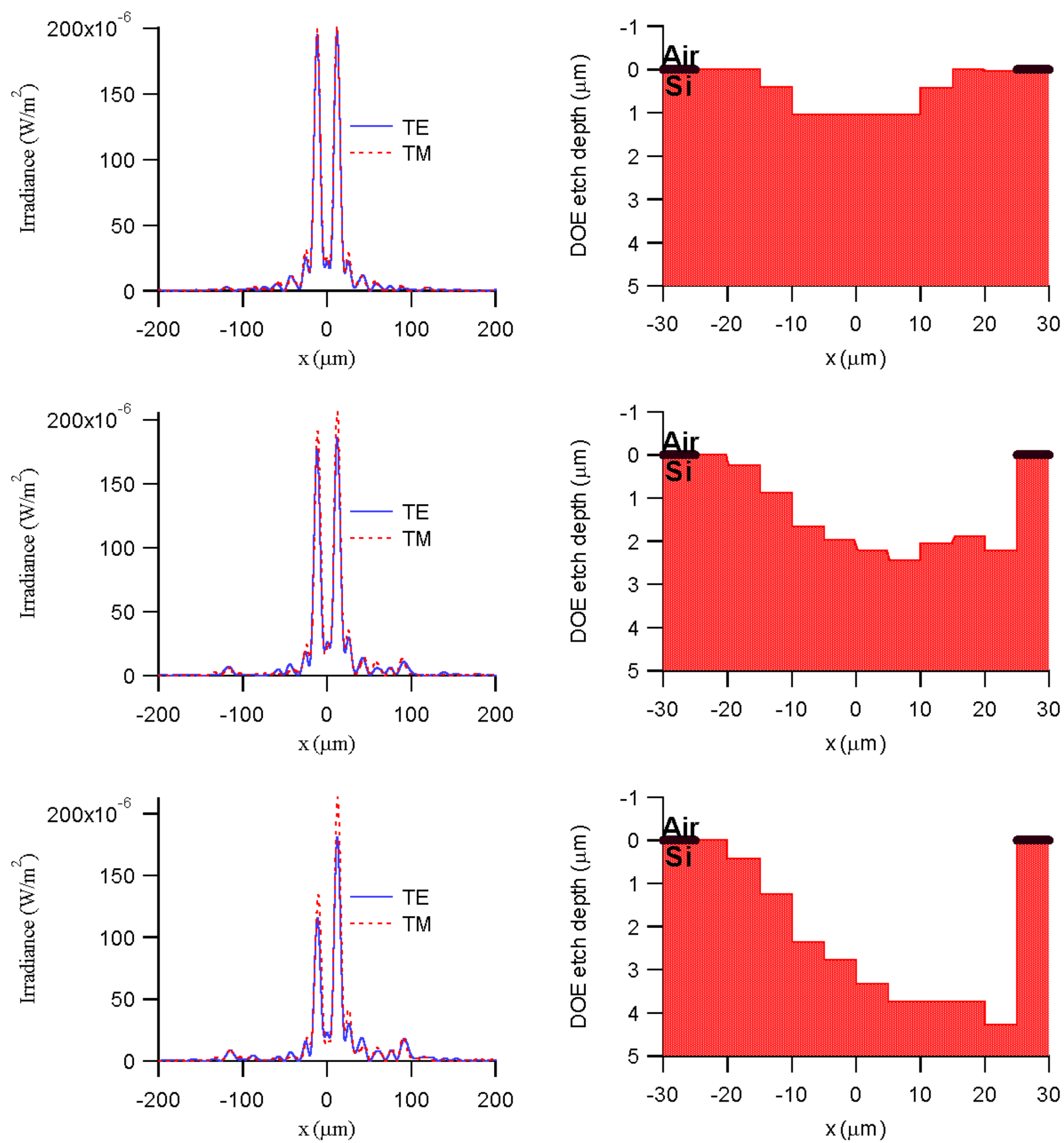

Figure 3.16 From top to bottom: irradiance and DOE profile for center, middle, and side-pixel 1-2 beamfanners for the 5-micron lateral feature size, 32 phase level case.

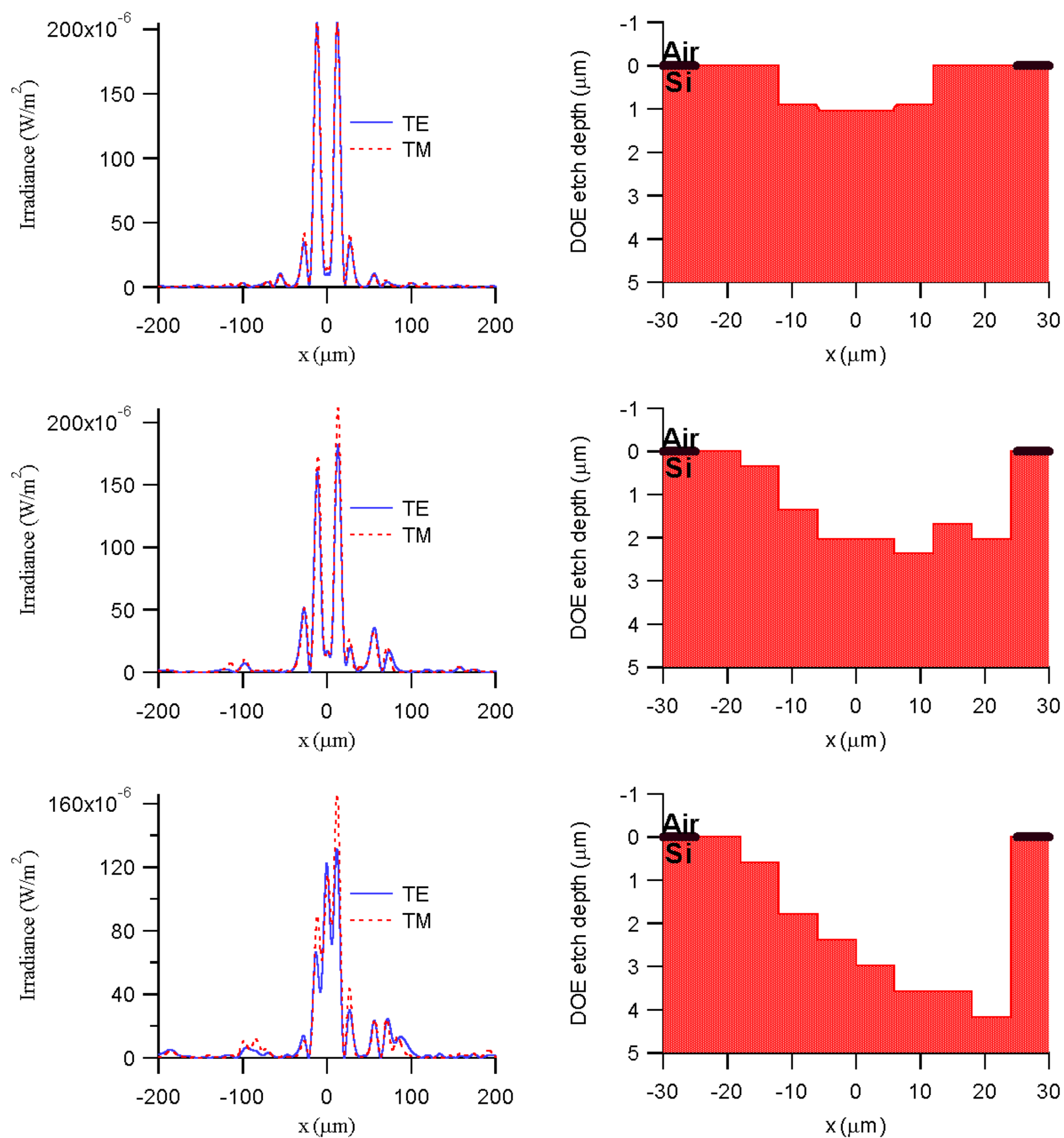

Figure 3.17 From top to bottom: irradiance and DOE profile for center, middle, and side-pixel 1-2 beamfanners for the 5-micron lateral feature size, 64 phase level case.

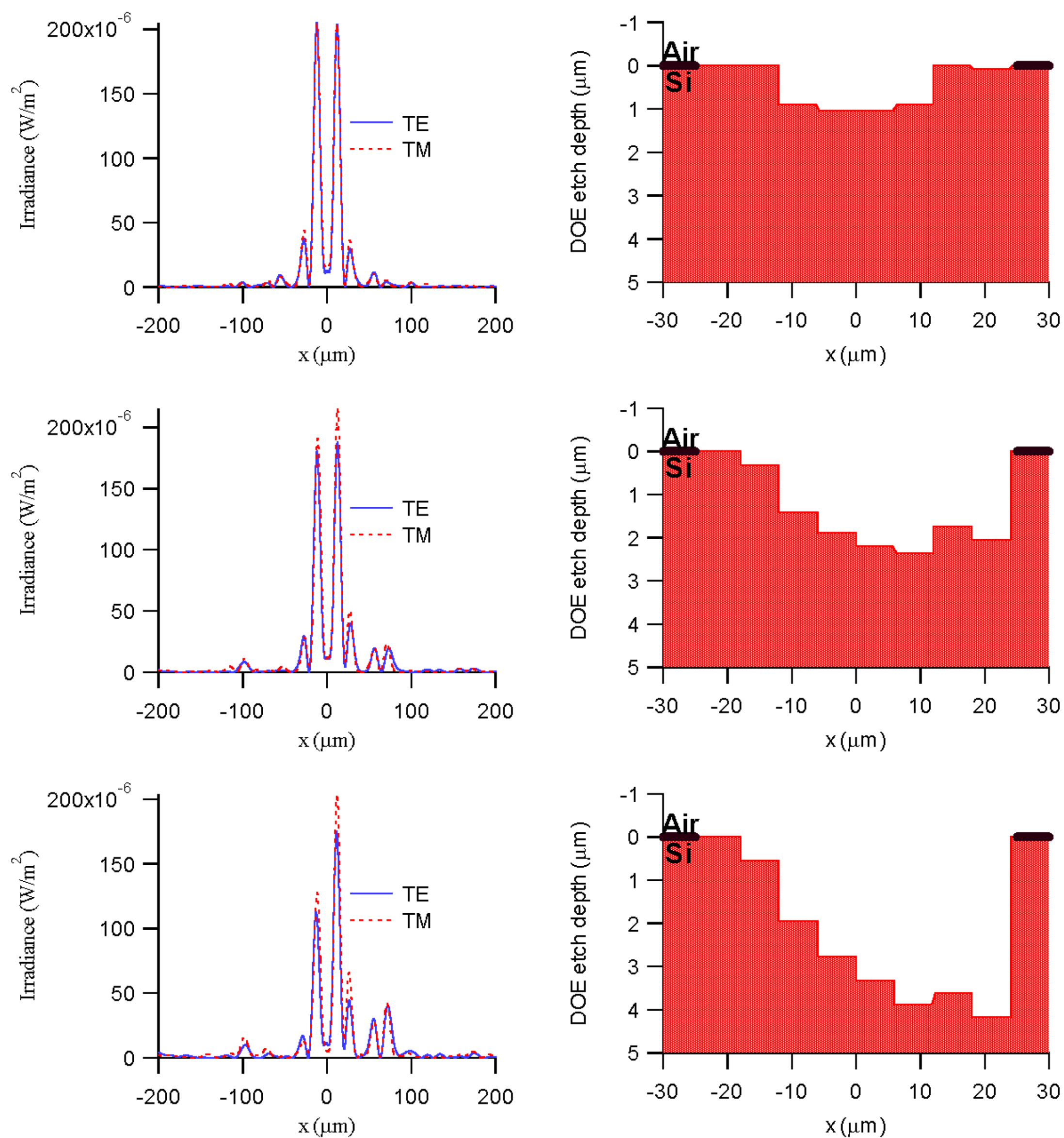

Figure 3.18 From top to bottom: irradiance and DOE profile for center, middle, and side-pixel 1-2 beamfanners for 6-micron lateral feature size, 8 phase level case.

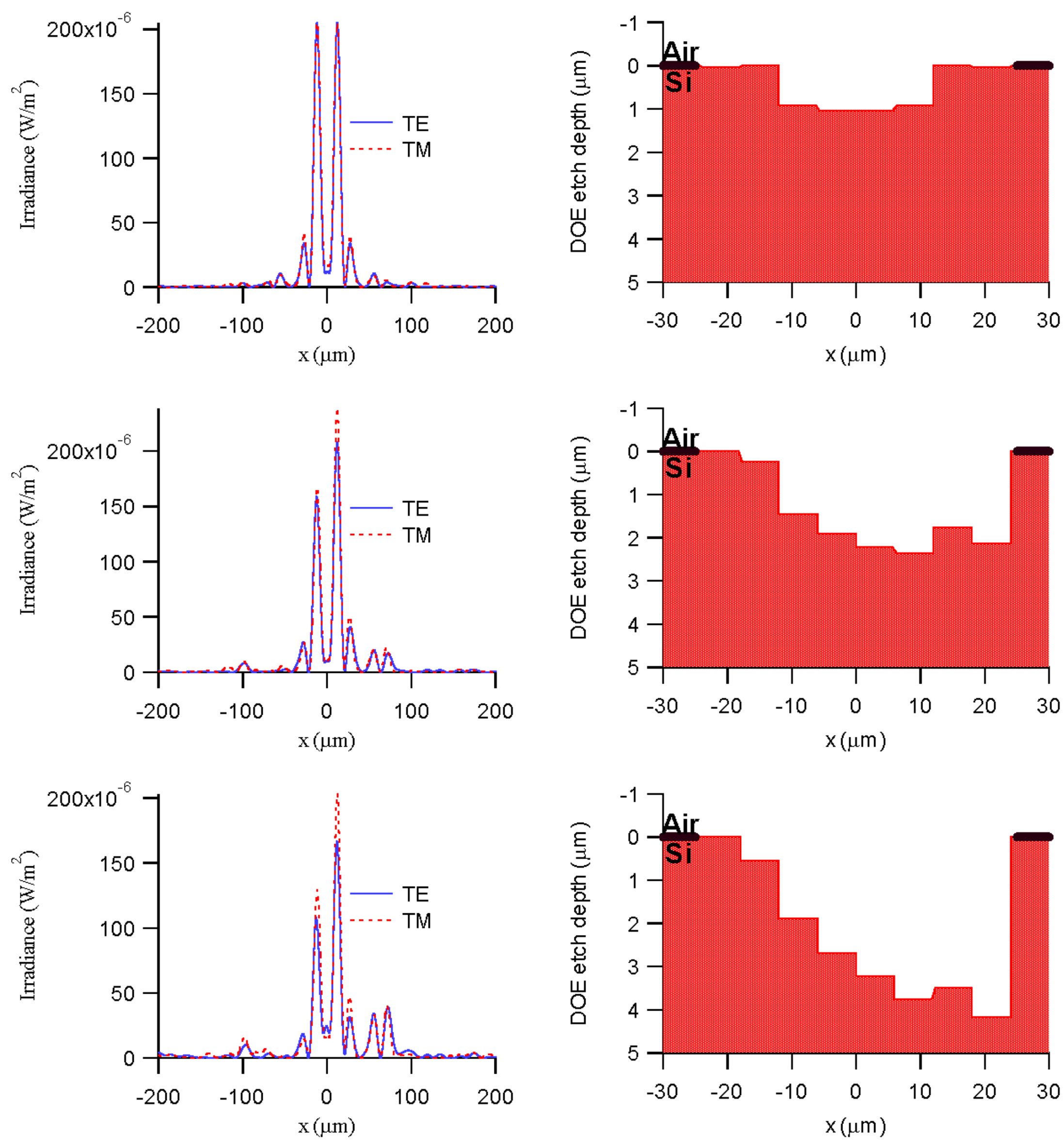

Figure 3.19 From top to bottom: irradiance and DOE profile for center, middle, and side-pixel 1-2 beamfanners for 6-micron lateral feature size, 16 phase level case.

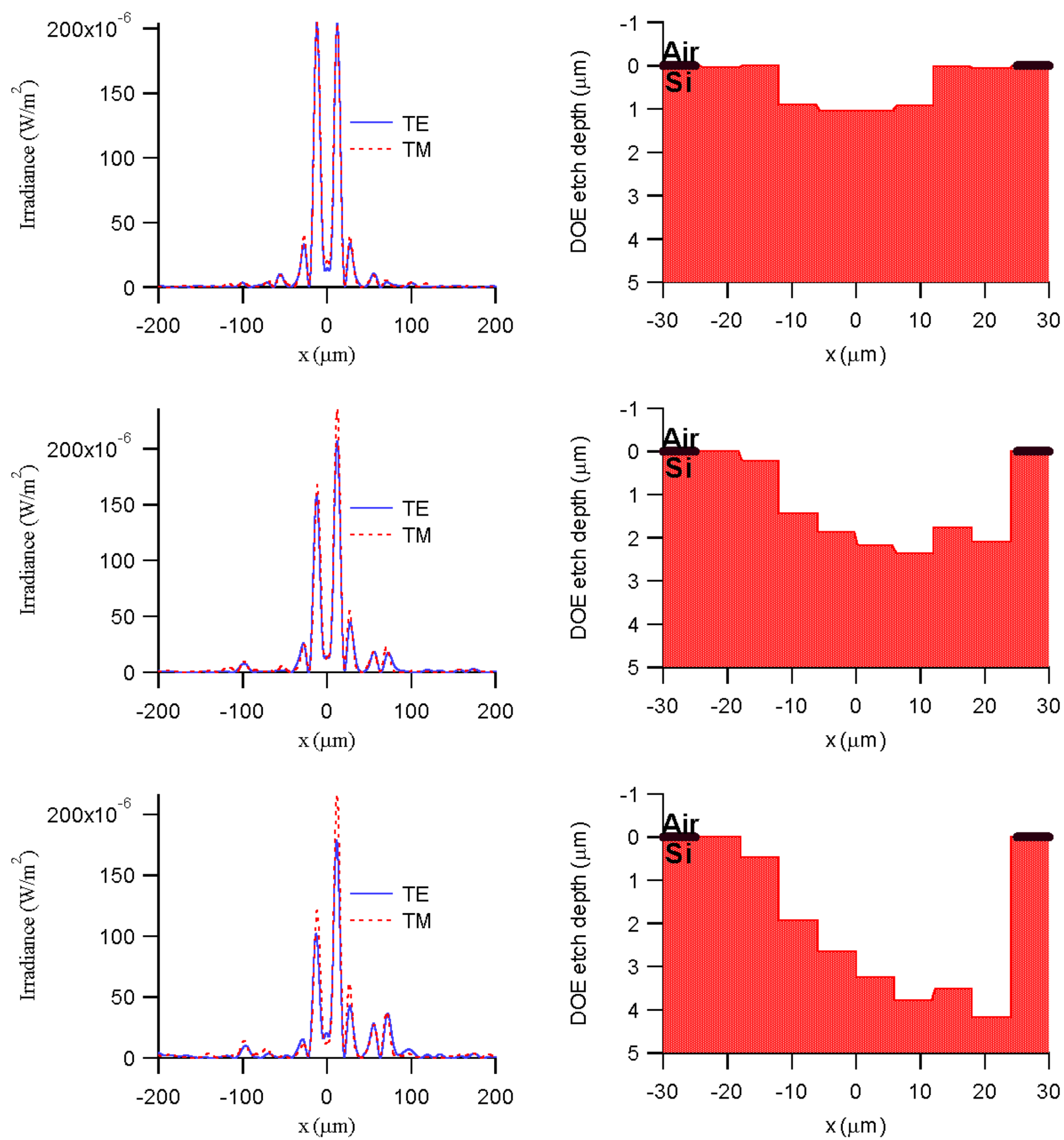

Figure 3.20 From top to bottom: irradiance and DOE profile for center, middle, and side-pixel 1-2 beamfanners for 6-micron lateral feature size, 32 phase level case.

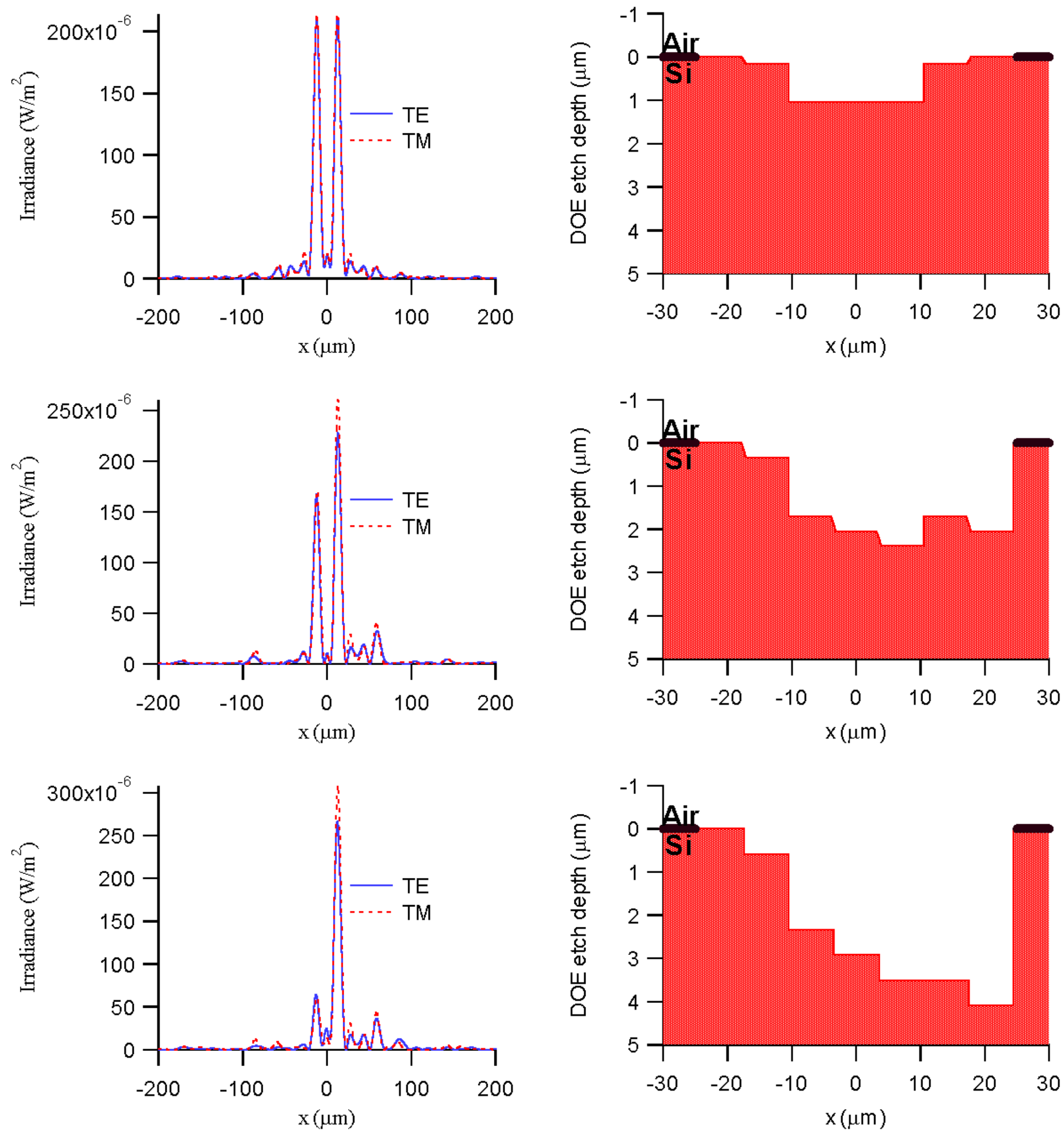

Figure 3.21 From top to bottom: irradiance and DOE profile for center, middle, and side-pixel 1-2 beamfanners for 6-micron lateral feature size, 64 phase level case.

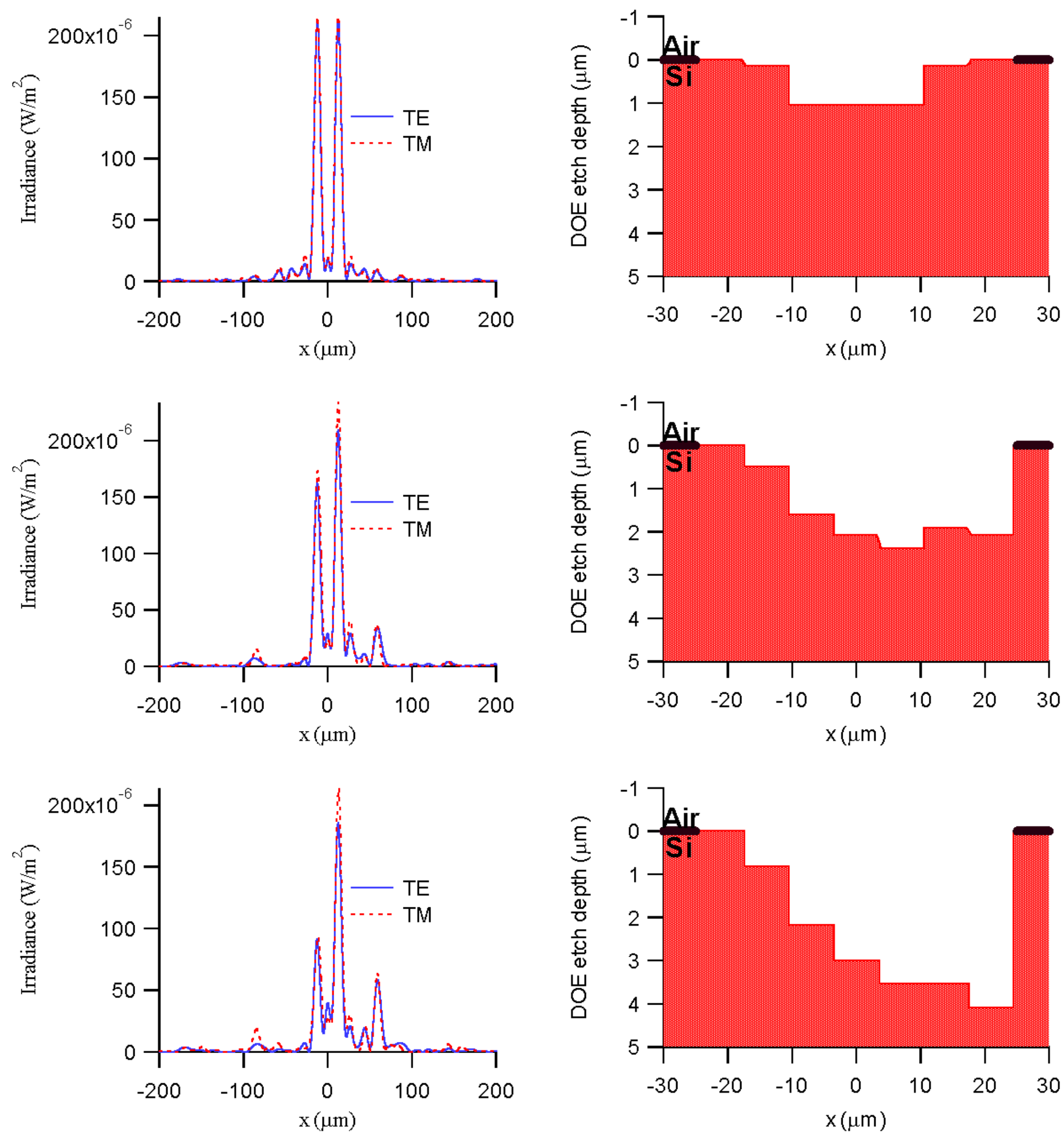

Figure 3.22 From top to bottom: irradiance and DOE profile for center, middle, and side-pixel 1-2 beamfanners for 7-micron lateral feature size, 8 phase level case.

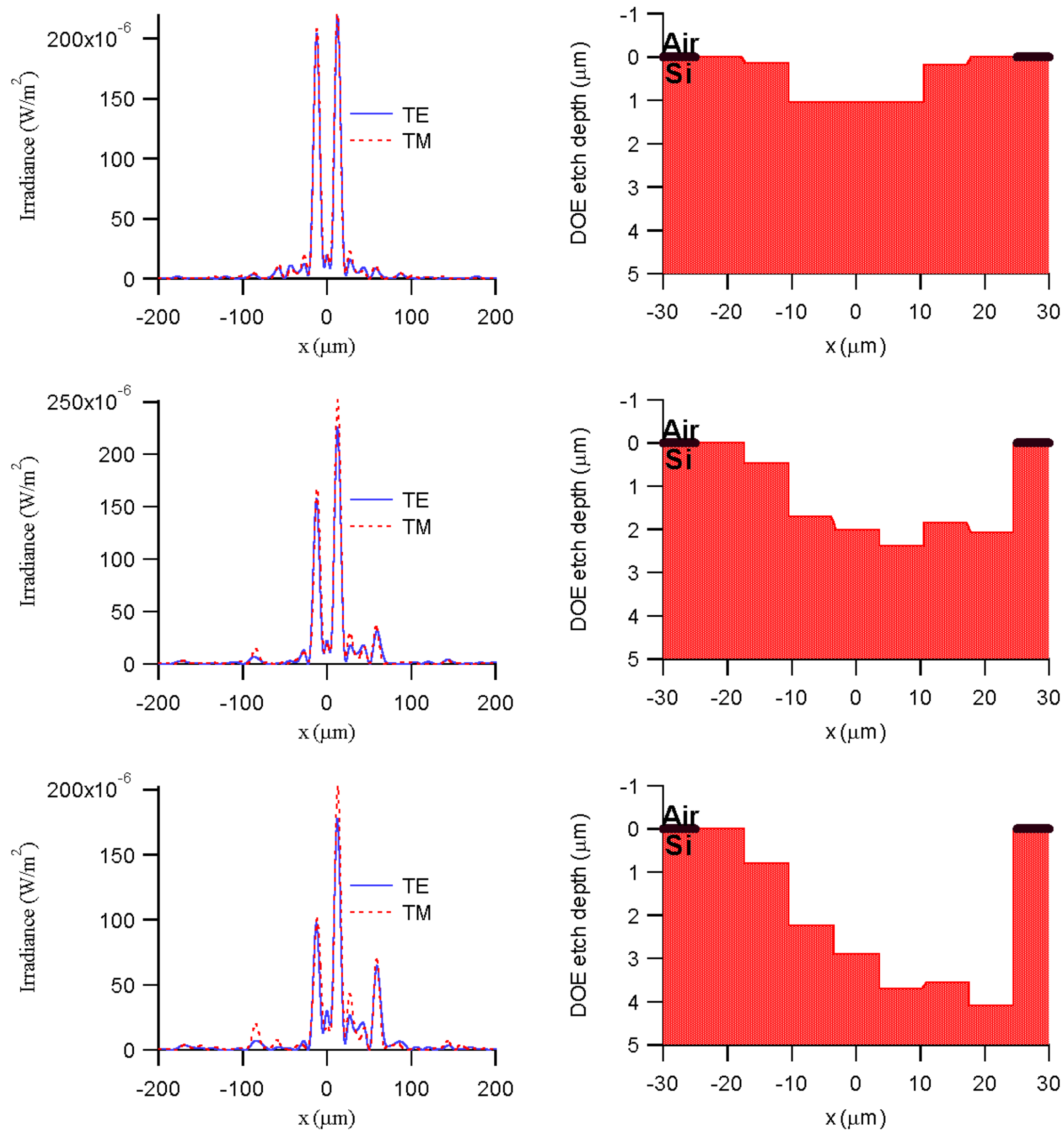

Figure 3.23 From top to bottom: irradiance and DOE profile for center, middle, and side-pixel 1-2 beamfanners for 7-micron lateral feature size, 16 phase level case.

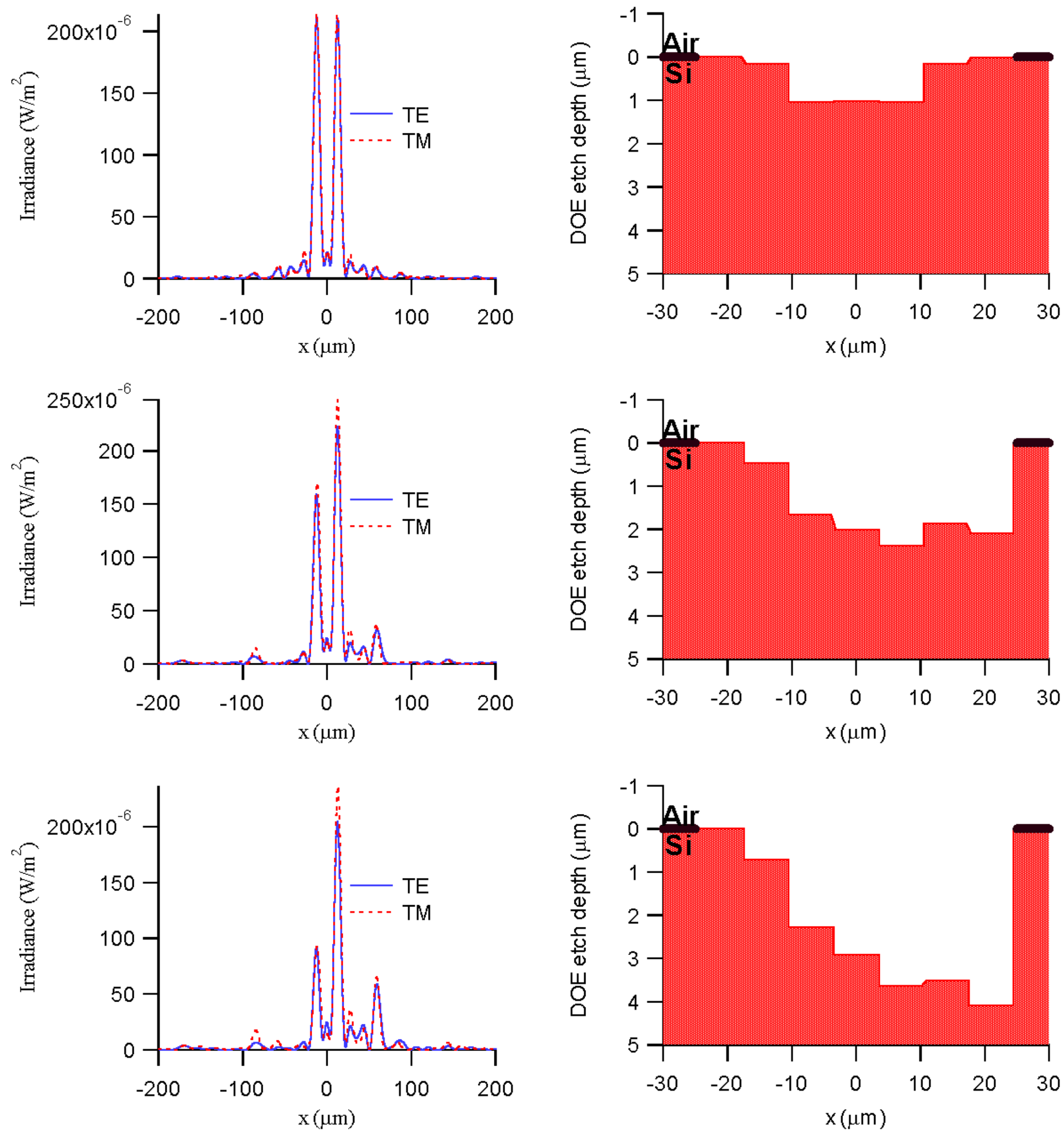

Figure 3.24 From top to bottom: irradiance and DOE profile for center, middle, and side-pixel 1-2 beamfanners for 7-micron lateral feature size, 32 phase level case.

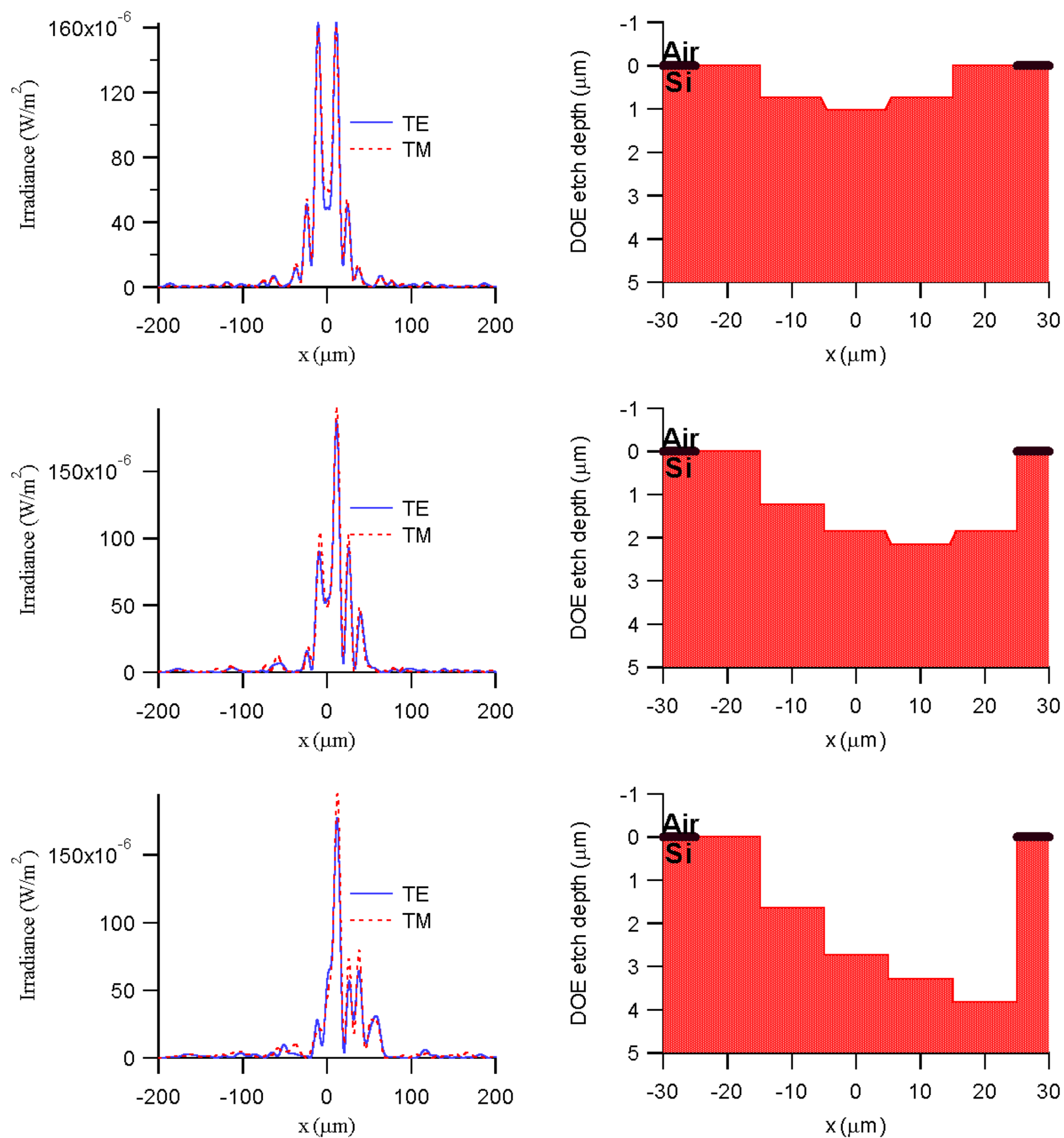

Figure 3.25 From top to bottom: irradiance and DOE profile for center, middle, and side-pixel 1-2 beamfanners for 7-micron lateral feature size, 64 phase level case.

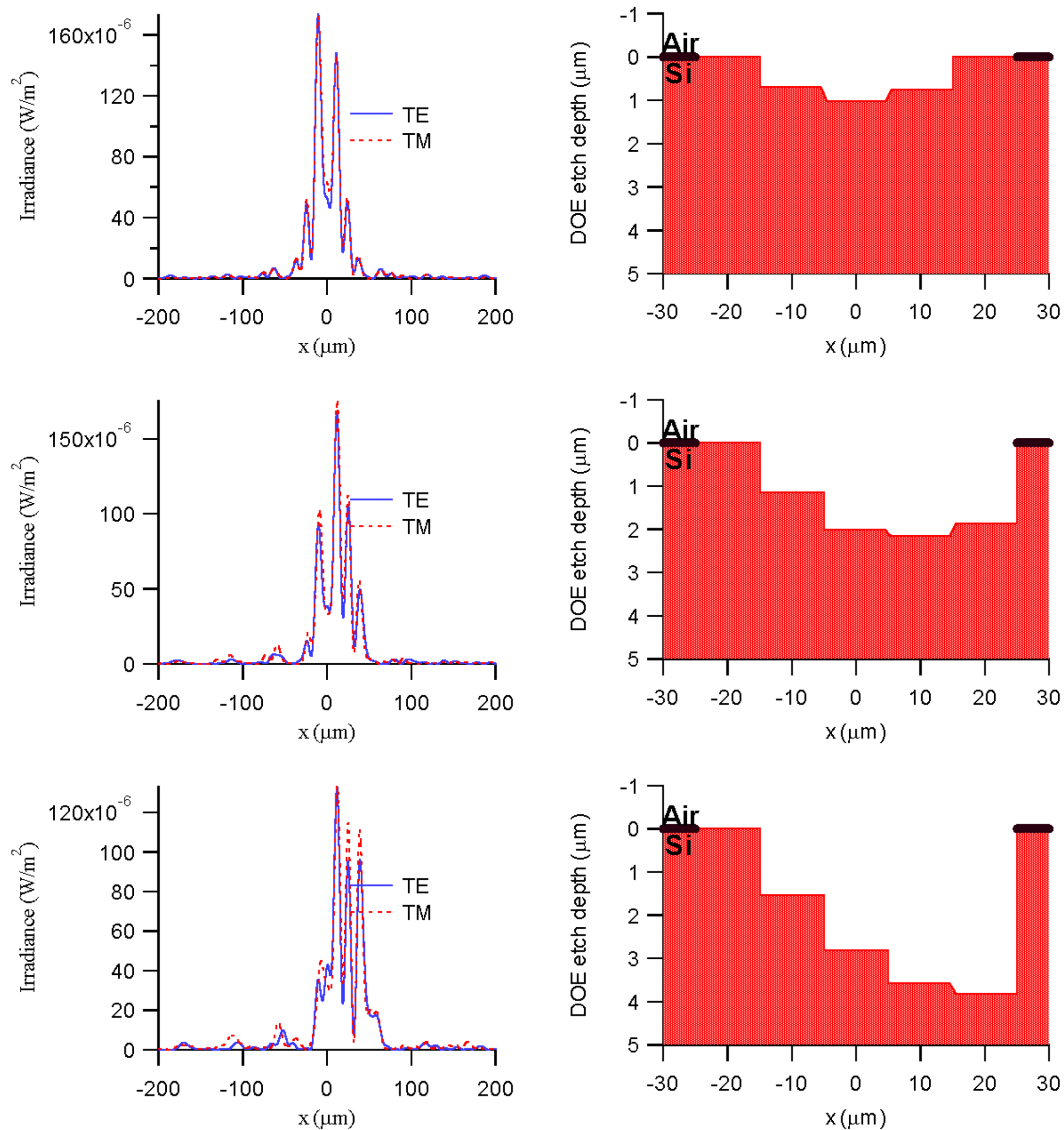

Figure 3.26 From top to bottom: irradiance and DOE profile for center, middle, and side-pixel 1-2 beamfanners for 10-micron lateral feature size, 8 phase level case.

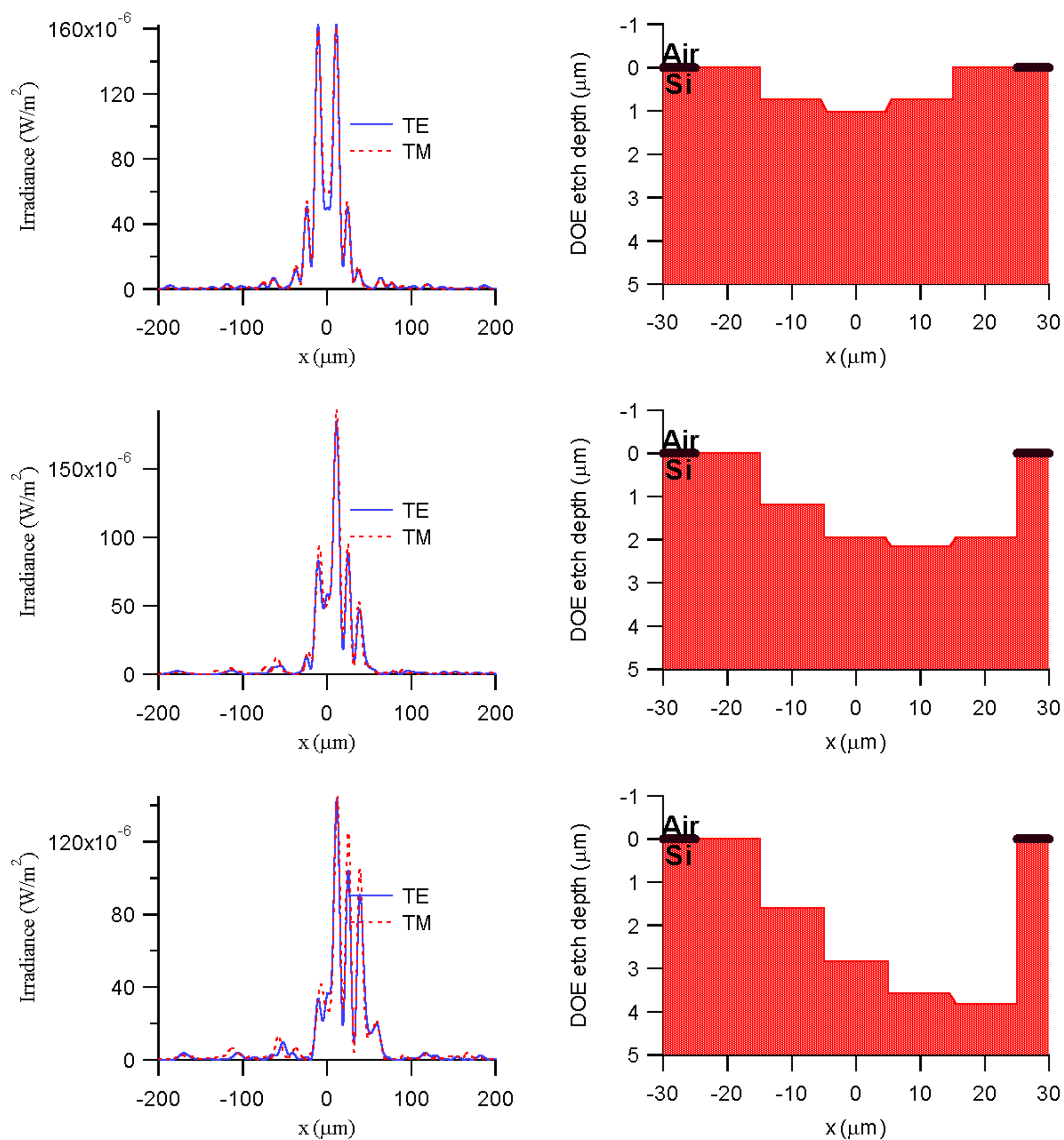

Figure 3.27 From top to bottom: irradiance and DOE profile for center, middle, and side-pixel 1-2 beamfanners for 10-micron lateral feature size, 16 phase level case.

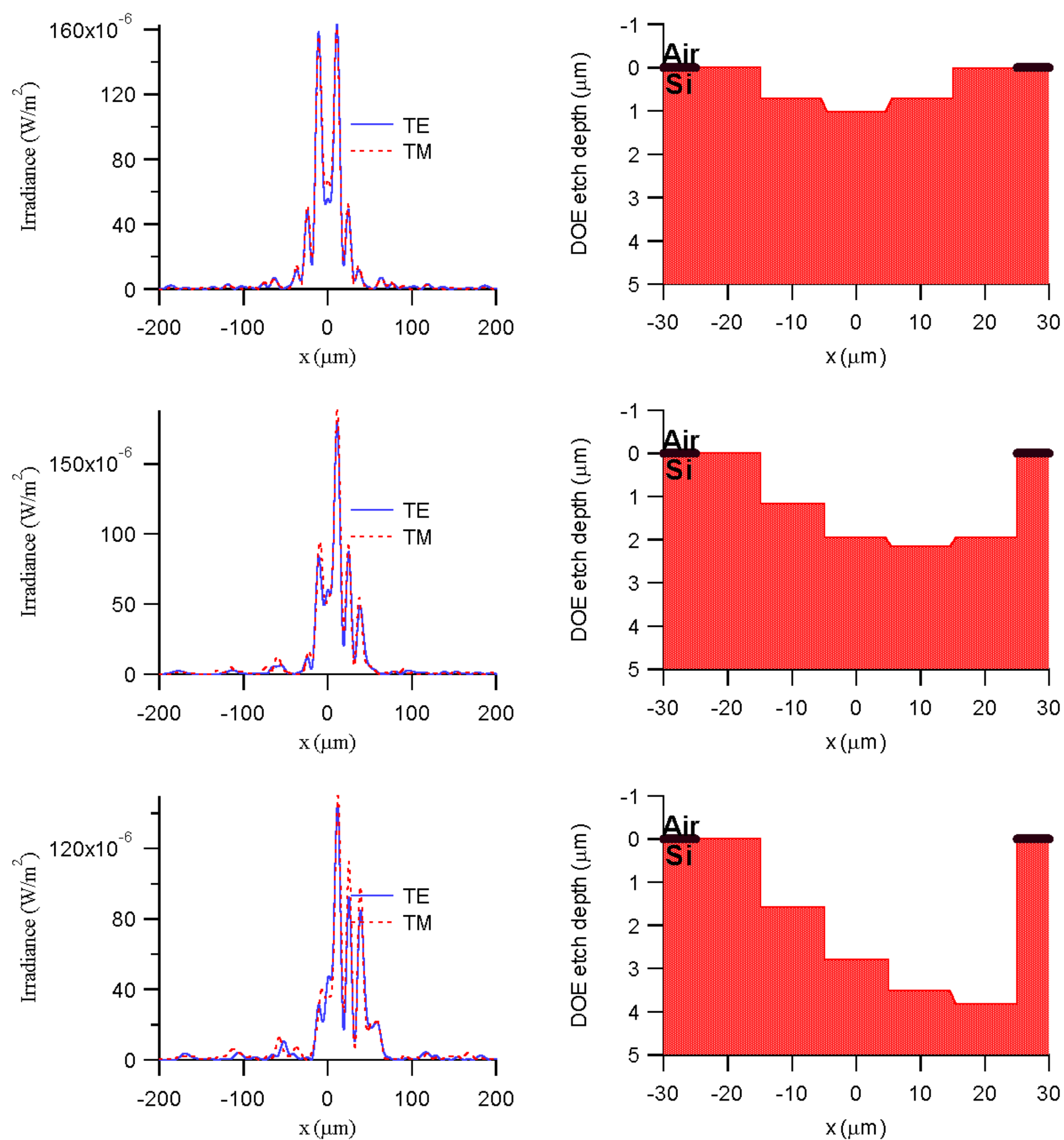

Figure 3.28 From top to bottom: irradiance and DOE profile for center, middle, and side-pixel 1-2 beamfanners for 10-micron lateral feature size, 32 phase level case.

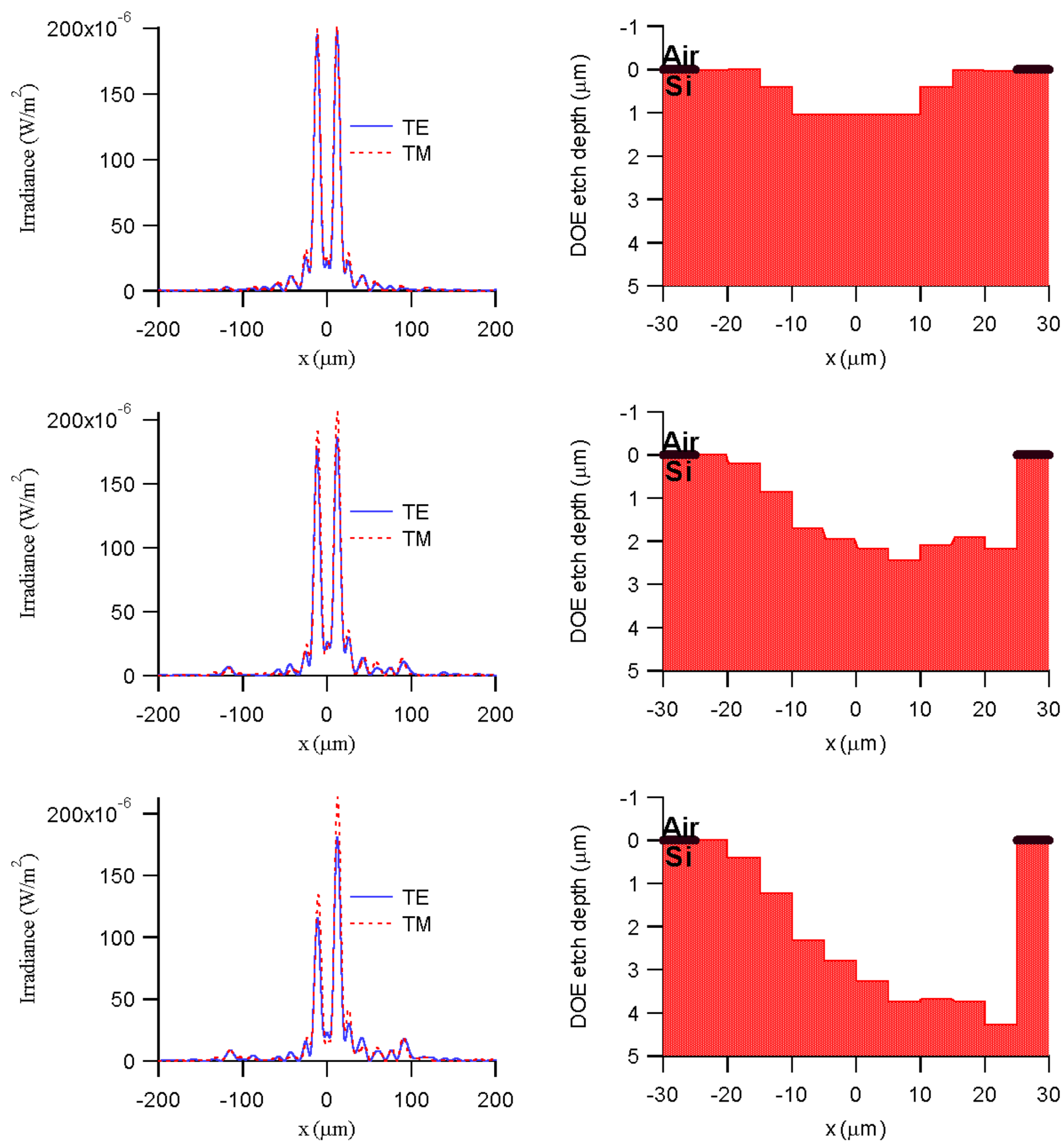

Figure 3.29 From top to bottom: irradiance and DOE profile for center, middle, and side-pixel 1-2 beamfanners for 10-micron lateral feature size, 64 phase level case.

A variety of observations can be made from these plots. First of all, it should be stated that the on-axis case (center-pixel) has either a symmetric or very nearly symmetric irradiance distribution about the center of the detector plane. The 10-micron lateral feature size case has more flux located interior to the detector regions than other center-pixel cases. This would seem to be due to the shallow trough in the bottom of the 10-micron lateral feature size design. The center-pixel designs with slight asymmetries are due to the slightly asymmetric designs of the beamfanner profiles. This was an artifact of the lateral feature size re-sampling technique discussed earlier.

Examination of the far off-axis case (side-pixel) shows up the weakness of the larger feature sizes. There is not a single case that does not demonstrate flux asymmetry, but the cases with 5-micron lateral feature sizes and 32 and 64 phase levels hold some hope. The 6-micron lateral feature size, 16, 32, and 64 phase level cases may perhaps be useful, but for these off-axis cases there is considerable flux in the detector plane well outside the 50-micron wide region that corresponds to the position meant for illumination. In an IR camera focal plane element, this would yield unwanted cross-talk. These are the best cases, and it is clear from examination of all plots that flux asymmetry and cross-talk will increase as illumination goes further off-axis. Flux symmetry shows some improvement with increased phase quantization. Increased phase quantization allows the design a better chance of selecting phase levels closer to the levels prescribed by the original 256 phase level design. These plots suggest that with 16-plus phase levels, it is possible to get very similar flux symmetry characteristics.

Larger lateral partitions yield cases with more flux located outside the two 15-micron wide detector regions. More TM flux gets transmitted than TE flux as illumination progresses further off-axis. The TE and TM fluxes both exhibit similar degrees of symmetry/asymmetry, however. Most important is the fact that neither TE nor TM flux is disproportionately small with respect to the other. An imaging polarimeter is only useful if both modes are present.

3.4.2 Diffraction efficiency and signal-to-noise ratio of 1-2 beamfanner irradiance

Table 3.1 and Table 3.2 give the predicted diffraction efficiency and signal-to-noise ratio of the 48 1-2 beamfanners. These are quantitative measures of beamfanner performance and are important, because it is necessary to have most of the power transferred through the photo-detector apertures rather than outside the apertures, where it can contribute to cross-talk between individual beamfanners. The actual quantity determined in the detector plane is the Poynting flux, or irradiance, given by

$$\vec{S} = \mathrm{Re}(\vec{E} \times \vec{H}), \tag{3.59}$$

and diffraction efficiency and signal-to-noise ratio are defined as

$$\frac{\vec{S}_d}{\vec{S}_{tot}} = \mathrm{DE} \tag{3.60}$$

and

$$\frac{\vec{S}_d}{\vec{S}_{od}} = \mathrm{SNR} \tag{3.61}$$

respectively. $\vec{S}_d$, $\vec{S}_{tot}$, and $\vec{S}_{od}$ represent the flux through the detector apertures, the total flux across the 50-micron field of the detector plane, and flux outside the detectors respectively.

Table 3.1 Diffraction efficiency of individual 1-2 beamfanners

5μ feature size	8 phase levels	16 phase levels	32 phase levels	64 phase levels
Center-pixel	0.87	0.87	0.87	0.87
Middle-pixel	0.82	0.84	0.85	0.84
Side-pixel	0.78	0.78	0.79	0.80

6μ feature size	8 phase levels	16 phase levels	32 phase levels	64 phase levels
Center-pixel	0.89	0.88	0.88	0.89
Middle-pixel	0.80	0.85	0.84	0.84
Side-pixel	0.74	0.78	0.77	0.77

7μ feature size	8 phase levels	16 phase levels	32 phase levels	64 phase levels
Center-pixel	0.86	0.86	0.86	0.86
Middle-pixel	0.81	0.82	0.81	0.81
Side-pixel	0.76	0.70	0.66	0.69

10μ feature size	8 phase levels	16 phase levels	32 phase levels	64 phase levels
Center-pixel	0.85	0.85	0.85	0.85
Middle-pixel	0.77	0.75	0.76	0.76
Side-pixel	0.59	0.50	0.51	0.52

Table 3.2 Signal-to-noise ratio of individual 1-2 beamfanners

5μ feature size	8 phase levels	16 phase levels	32 phase levels	64 phase levels
Center-pixel	6.83	6.82	6.83	6.92
Middle-pixel	4.51	5.25	5.68	5.12
Side-pixel	3.62	3.64	3.87	3.99

6μ feature size	8 phase levels	16 phase levels	32 phase levels	64 phase levels
Center-pixel	7.98	7.60	7.65	7.72
Middle-pixel	4.10	5.46	5.23	5.36
Side-pixel	2.81	3.49	3.33	3.41

7μ feature size	8 phase levels	16 ph.ase levels	32 ph.ase levels	64 phase levels
Center-pixel	6.34	6.33	6.31	6.28
Middle-pixel	4.19	4.59	4.33	4.38
Side-pixel	3.18	2.37	1.98	2.24

10μ feature size	8 phase levels	16 phase levels	32 phase levels	64 phase levels
Center-pixel	5.55	5.50	5.54	5.52
Middle-pixel	3.31	2.99	3.19	3.12
Side-pixel	1.41	0.99	1.05	1.10

The diffraction efficiency and signal-to-noise ratio values of Tables 3.1 and 3.2 are presented in terms of the sum of TE and TM flux rather than treating them separately. Some important information can be obtained from these tables. First of all, the diffraction efficiency and signal-to-noise ratio both decrease as illumination is directed further off-axis. The 1-micron lateral feature design does not demonstrate such severe degradation, but the larger feature sizes make far off-axis performance very poor.

The center-pixels are acceptable, with the 5-micron, and especially the 6-micron lateral feature size cases yielding an excellent center-pixel flux. The 7-micron and 10-micron lateral feature size beamfanners have good diffraction efficiency and signal to noise ratio as well, since the larger feature size designs closely approximate the ideal design.

As a basic trend, signal-to-noise ratio and diffraction efficiency are functions of lateral feature size, with larger feature sizes yielding decreased flux through the detector apertures. The 5-6-micron cases are close enough to be a tossup, however.

For the case of BEM-predicted design performance, it can be concluded that the 5-6-micron lateral feature sizes cases, with 16 or more phase levels, hold the best hope for constructing viable 1-2 beamfanners, since they split the light more evenly and possess greater diffraction efficiency and signal-to-noise ratio as defined in Equations (3.60) and (3.61). Whether they can be generalized to viable 1-4 beamfanners through the etch-depth addition previously discussed is another matter. In any event, the case of far off-axis illumination is very problematic. Perhaps larger feature sizes will necessitate smaller beamfanner arrays that don't catch the far off-axis illuminating light.

Chapter 4

FABRICATION OF NICHOLS AND UAH BEAMFANNER ARRAYS

There are three main steps involved in the fabrication of a DOE, using HEBS grayscale techniques, which are applicable to the Nichols array. First, an etch-depth vs. optical density calibration curve must be developed. This is accomplished using a grayscale test mask with a wide range of optical densities to expose photoresist that has been spun on top of a material of which the DOE will be composed. For this research, the material is silicon. This photoresist is then soft-baked and developed with an alkali-based chemical. A reactive-ion-etch is performed, and a measurement of the optical density vs. etch-depth in silicon is obtained. The second step is to use the optical density vs. etch-depth curve generated from this measurement to design a grayscale mask with the appropriate optical densities that correspond to the etch-depths of the planned DOE. This is accomplished in conjunction with companies that can fabricate such masks. Finally, as in the first step, the DOE grayscale mask is used to pattern photoresist on a silicon substrate. This is etched to produce the desired DOE. Section 4.1 will present the specifics of this process for the fabrication of the Nichols array.

For the production of the UAH array, the photolithography process was contracted to MEMS-Optical, of Huntsville, Alabama, so the etch process was the only step performed by this author in the fabrication of the array. Details of this will be presented in Section 4.2.

4.1 Development of 2-3-micron lateral feature size beamfanner array fabrication procedure

This section will present an overview of basic microfabrication techniques followed by their application to the production of the Nichols beamfanner array. Lessons learned from this effort are examined at the end of this section.

4.1.1 General micro-fabrication procedures

At the outset of this research, with corporate deadlines to navigate, it was necessary to research all aspects of micro-fabrication in a quick but thorough manner. This involved learning techniques such as spinning thin films of photoresist on three-inch diameter silicon wafers, patterning this photoresist with a mask aligner/UV exposure system, developing the photoresist pattern, and finally etching the pattern into the silicon itself. Ideally, when searching for the ideal set of parameters for a fabrication process, it is beneficial to have enough time and equipment to handle a search that covers a large parameter space. For the case of the first array series, however, it turned out that although much work was done, and many lessons were learned, the actual product itself was a disappointment. A brief discussion of the fabrication process, with focus on photolithography and etching, will next be presented.

4.1.1.1 Photolithography

The photolithographic process begins by spinning photoresist on a substrate with a spinner. This spinner typically has a vacuum chuck connected by a shaft to an electric motor. This motor can typically reach speeds of up to 10,000 rpm. Depending on the viscosity of the photoresist, it is often advisable to gradually ramp the speed of the centrifuge to a final desired rate. A higher rate will spin a thinner coat of photoresist. The photoresist, consisting of Novelac

resin and solvents, is a polymeric substance that must be baked after coating in order to harden the resin through removal of the solvents. This can be done on a hotplate or in a convection oven and is referred to as a soft-bake.

After the soft-bake, the photoresist is patterned by UV exposure through a mask followed by development in an alkali solution. A certain amount of UV energy is necessary to achieve an ideal exposure, and this energy is simply the power output of the exposure system multiplied by a certain time interval. As a general rule, the UAH lab keeps the exposure power constant and varies the exposure times for different photoresist thickness requirements. Experimentation is necessary to determine a proper developer solution and development time. For the case of grating structures in positive resist, under-developed ridge profiles are characterized by thick bases and thin tops. An over developed profile is characterized by ridges that are thinner than intended and sometimes washed out on top.

It is critical to develop a photolithographic process that yields profiles that can be etched successfully. As mentioned in the second chapter, grayscale processes add to the difficulty, since there are features with many different heights and widths. Different feature heights and feature widths etch in differing manners, so often it is difficult to find a set of etch parameters that will properly handle a given photolithographic profile. It is essential to coordinate a photolithographic profile with an etch process during the calibration stage that will yield the proper final DOE profile.

After exposure and development, depending on the fabrication goals, a second bake may or may not be required. For the work presented here, the second bake, known as the hard-bake, turned out to be disadvantageous for reasons presented in the next section.

4.1.1.2 Silicon etch

Although there is a large amount of literature dealing with silicon etching, it was difficult to find useful literature dedicated to grayscale silicon etching. It became clear, however, that in order to etch photoresist on silicon, sulfur hexafluoride would be necessary to etch the silicon, while molecular diatomic oxygen would be required to etch the photoresist. In a reactive ion etch, sulfur hexafluoride yields free negative fluorine ions that bond with silicon atoms and form a volatile gas that is removed via vacuum pump. The molecular oxygen likewise is dissembled into ions that react with the polymeric photoresist. The etch rates for the photoresist and silicon are in general different, and the ratio of the etch rate of silicon to the etch rate of photoresist, as mentioned previously, is defined as the selectivity. There was also the possibility of using triflouromethane to passivate the sidewalls of the etched features, thus increasing the degree of etch anisotropy. The etch chemistry for the first array series employed trifluoromethane along with oxygen and sulfur hexafluoride. The trifluoromethane actually bonds with the silicon sidewalls forming a protective polymeric layer that prevents undercutting of the sidewalls. Trifluoromethane, which is an excellent etching gas for silicon dioxide, also bonds with the molecular oxygen, and this causes a reduction in the etch rate of the photoresist. Chlorine bearing gases can also be employed for silicon etching [42], but were unavailable in the UAH lab. The only options available for a photoresist/silicon etch, in fact, were sulfur hexafluoride, oxygen, and trifluoromethane. Chlorine gas is highly toxic, and it is absolutely necessary to have a safe disposal system for the gas. Of interest for future research would be the incorporation of argon [43] and helium gas to promote etch anisotropy, since time and schedule did not present this opportunity.

Aside from etch chemistry, which is dictated by controlling flow rates of the fore-mentioned gases into the RIE chamber, there are other important parameters that must be controlled. The chamber pressure is one parameter, and in general a low chamber pressure yields

a slower etch rate with greater anisotropy. Another parameter is the RF power, which controls the kinetic energy of the ions in the chamber. The goal of achieving ideal etch parameters is based on finding an advantageous interplay between gas flow rates, chamber pressure, and RF power. A combination of these factors must be found that yields the desired selectivity, while at the same time producing an anisotropic etch that can be achieved in the shortest time possible.

Another important consideration is process repeatability. This requires that all relevant parameters involved in a fabrication process are known and kept constant when producing multiple DOEs. This requires a fabrication environment that has as little particulate and chemical contamination as possible, and at UAH this environment is a class 1000 clean room. Process repeatability also requires the upkeep of careful logs that account for all process parameters. The RIE chamber must be reverted to the initial conditions that existed prior to the last like etch process. This is especially important when an etch follows a previous etch with a different chemistry. If that previous process, for example, is an oxygen and trifluormethane etch of photoresist on silicon dioxide, and the current process is a photoresist on silicon etch using oxygen and sulfur hexafluoride, care must be taken to remove residual potential reactants that could drastically alter the silicon etch. The author achieved this with frequent oxygen descum processes coupled with frequent cathode wipe-downs. An oxygen descum removes polymer residue in the chamber, and cleaning the cathode removes residual carbon.

There are other more subtle factors involved in achieving a successful etch result. The placement of DOE samples inside the chamber, as well as the number of samples, can be critical. The DOE samples themselves are reactants, and the quantity as well as surface exposure can influence the etch results. The DOEs rest in contact with the chamber cathode, and the temperature of this cathode, as well as the residual etch products on the cathode and inside of the chamber walls, can affect etch results.

4.1.2 Etch selectivity calibration

The Nichols array, as mentioned before, was generated using a HEBS mask purchased from Canyon Materials in San Diego, California. Before this, Canyon Materials provided a calibration mask for the determination of the etch-depth vs. optical density curve, which will be examined in this section. The calibration mask had 50 sets of .02×.08 mm rectangular pads with optical densities ranging form 0 to 2.0 for the wavelength of 365 nm. These 50 sets were actually divided into two groups of 25, with one group being written with a 20 KV electron beam, and the second group being written with a 30 KV electron beam. The calibration mask also had gratings with features as small as 5 microns across. These allowed the user to prepare a fabrication process capable of constructing DOEs with features of this dimension. Optical density is a measure of the degree of opacity [44]. It is defined as

$$\mathrm{OD} = -\log_{10} \mathrm{T} . \tag{4.1}$$

The variable T is the transmission coefficient of the specific region of the mask with the corresponding optical density. Positive photoresists, such as Shipley Microposit 1805, 1811, and 1827 and Shipley Microposit STR 1045 and 1075, and OCG 825, were all employed by the author in the research leading to the development of the calibration process. 1805, 1811, and 1827 are low viscosity photoresists, and they spin out into thinner coatings than the 1045, 1075, and the 825. As a consequence, the 1045, 1075, and 825 can be etched with a combination of parameters that yield deeper etch-depths with lower selectivities.

Higher optical densities yield higher features, or shallower feature top surface depths, upon positive photoresist development. This is due to the fact that positive photoresists dissolve easily after exposure to UV light and development in chemicals such as Microposit 351 and Microposit MF 319, and lower optical densities transmit more UV power into the photoresist

upon exposure than higher optical densities. As an analogy, lower optical densities dig a deeper hole, upon development, in the photoresist. Shipley Microposit STR 1045 was the photoresist that was eventually adopted after many trials, since it could be etched at a selectivity that yielded better feature fidelity than the other photoresists mentioned.

A brief description of the calibration process will now be presented. The first attempts at a successful process used 1805 and 1811 photoresists. Although the photolithography yielded reasonable feature fidelity, etch selectivities of 10-20 were impossible to achieve. This required the adoption of some thicker resists, and 1045 and 1075 allowed a range of selectivities between 1 and 2. The thicker resists presented a new set of challenges. The thicker patterned regions of this resist tended to melt during the etching process, and the only remedy for this was performing a longer soft-bake than was recommended in the material data sheets supplied by the resist manufacturers.

The 1075 resist, which was the thickest employed, not only had a tendency to melt, but it actually burned. When etched, a mangled, rough pattern was left in the silicon where this resist had been etched away. At the outset, there was some confusion as to the reason for this roughness. The author, after consulting with other researchers performing similar fabrication processes, believed it to be related to a need to hydrate the resist after development. To this end, DOE samples were immersed in water for hours, and even days, prior to etching. There seemed to be some evidence that this improved the etch process by yielding DOEs with less surface roughness, but there was not enough evidence to conclude the existence of a direct correlation between hydration and reduced roughness. As with the melting, the only successful way to eliminate the burning was to increase the soft-bake time by as much as 3 times the duration recommended in the data sheets.

It should also be noted that the hard-bake step was not viable for the thicker resists, since it would actually warp the resist profile by melting the higher features. After development, a de-

ionized water rinse, and a nitrogen gas blow-dry, the DOE was ready to be placed in the RIE chamber for etching.

The RIE etching step was by far the most time consuming and as a consequence was the main limiting factor that hampered a thorough research of a very large parameter space. Etching through 9 microns of silicon with a flow-rate ratio of oxygen and sulfur hexafluoride at pressures and powers that allowed for reasonable feature fidelity generally took between 1 and 3 hours. This, coupled with the fact that the author was not the only user of the fabrication equipment, made it difficult to run a sufficient matrix of process variations and therefore impossible to develop a convincingly repeatable fabrication process within Nichols Research time constraints. A tentative calibration recipe was, however, developed and submitted to Canyon Materials for DOE mask fabrication. The photolithographic process for this recipe called for a spin coating of 1045 resist at 1560 rpm for 40 seconds on a SCS centrifuge (Serial # 995-39-6). This was followed by a 45 second soft-bake at 90 degrees centigrade. This was followed by UV exposure on an AB-M Mask Aligner (Serial # 17491) at an intensity of 20 milliwatts per square centimeter for 42.5 seconds. The photoresist was developed in MF 319 developer for 2 minutes. The RIE etch process was accomplished with a Plasmatherm 790 RIE (Serial # PTI78202F). The etch process, based on a combination of gases advocated in [45] and [46], used flow rates of 18 sccm/2 sccm/20 sccm of sulfur hexafluoride/oxygen/trifluoromethane respectively. RF power was set at 175 Watts and the chamber pressure was maintained at 15 millitorr. The etch time was 150 minutes.

This process yielded the curve of Figure 4.1 seen below. The pad etch-depths in the silicon test wafers were measured using a Taylor Hobson Talystep profilometer. Figure 4.1 is presented as phase level as a function of optical density, with the highest phase level (256) being the highest etched feature in the silicon (9.3 microns above the deepest etch), and the lowest phase level (0) being the maximum etch-depth, or lowest feature (0 microns).

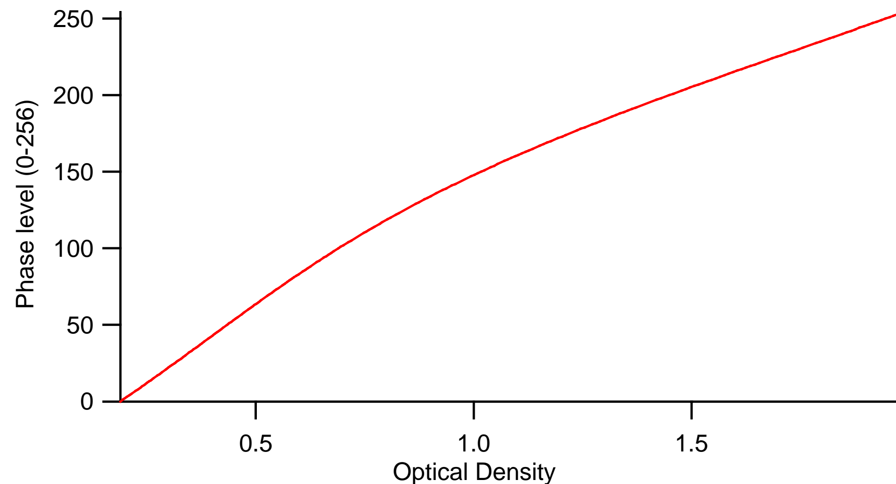

Figure 4.1 Calibration curve submitted to Canyon Materials for the grayscale mask for the Nichols array.

This calibration data was used to process the data files sent to Canyon Materials, who in turn fabricated the HEBS grayscale mask used for the photolithography of the Nichols array. Unfortunately, this mask had a serious flaw. Darker features, written in the HEBS glass with the 30 KV electron beam, had a regrettable tendency to bleed outside the boundaries of the square 2-3-micron regions that represented the individual DOE features. This alone made it impossible to fabricate the first beamfanner array to design specifications. It should also be mentioned that since the calibration mask did not have 2-3-micron square features, it was not possible to develop a process, prior to ordering the DOE mask, that was capable of testing photolithographic fidelity of such features.

4.1.3 Resultant fabrication of beamfanner array with 2-3-micron feature sizes

Despite having some admittedly difficult fabrication hurdles as a result of the blurred-feature HEBS DOE mask, an attempt to use the calibration recipe to fabricate the first

beamfanner array was made. Photolithography yielded patterns that not only suffered from the HEBS mask flaw, but the pattern features were simply too small for successful resolution in the mask aligner system. Producing a 2-3-micron square feature imprinted in resist using contact photolithographic techniques was certainly very ambitious. It also turned out that the calibration process recipe was not repeatable. This author was never able to achieve the exact etch-depths of the calibration curve submitted to Canyon Materials. The top photograph of Figure 4.2, on the next page, shows images, taken with a JEOL scanning electron microscope, of typical examples of beamfanners patterned in photoresist. Note the lack of feature fidelity in the photolithography picture and the rounding in the etch picture below. The etched beamfanners, shown in the bottom photograph in Figure 4.2, are a dramatic example of a melted photoresist pattern transferred into silicon. It was around this time that Nichols Research lost interest in the hardware fabrication approach to the beamfanner component of the IR camera focal plane array and began to concentrate on finding a solution using software to process the image.

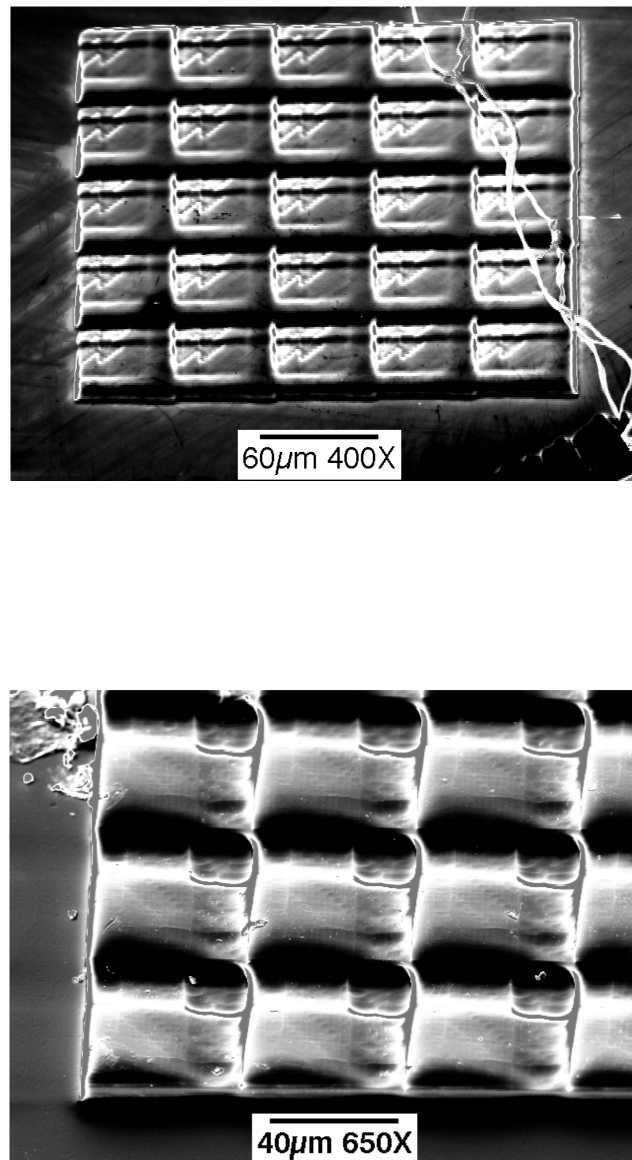

Figure 4.2 View of a center-pixel 1-4 beamfanner array with 2-3-micron lateral feature sizes and 256 phase levels in resist (top) and etched in silicon (bottom). Note the blurred features in the resist and the rounded features in the etch which are caused by melted resist features being transferred into the silicon.

4.1.4 Lessons learned from the first attempt

Although the first array series was unsuccessful from the standpoint of fabrication, it yielded some important lessons applicable for future grayscale fabrication attempts. These

lessons were carried over into the considerations in design and fabrication of the second beamfanner array series.

When developing any DOE with small features, it is easy to design a highly efficient structure. After all, the design phase allows one to make features any size and any shape desired. As a general rule, smaller features allow greater DOE efficiency. Trouble arises when such fine features cannot be fabricated with good fidelity. If the design personnel and the fabrication personnel don't both understand the limits of fabrication capability, and a design gets hardwired due to time constraints, it is possible to end up with an impossible fabrication task. This author was certainly new to grayscale fabrication and many micro-fabrication techniques in general. The beamfanner project was known to be ambitious before it was started, and as a consequence there was an accepted risk involved. In this light, perhaps, the Nichols array was a case of doing the best job possible with the amount of experience and time involved. It is clear, however, that design personnel and fabrication personnel need to have a good understanding of each other's work. The UAH array was designed and tested by the author with assistance from the designer of the Nichols array. The research presented in Chapter 3 is a result of this collaboration, and it is safe to say that both the design side and the fabrication side gained a greater understanding and developed a more useful approach toward creating a working beamfanner array.

Another lesson learned was that one needs to know the capabilities of vendors that supply items used in the fabrication process. The HEBS DOE mask, with its blurred features at high optical densities, is a good example. Even though the higher optical densities blurred outside the feature boundaries, the lower optical densities formed well-defined feature boundaries. If this had been known before hand, the calibration process could have been performed with a search of parameter spaces promoting higher selectivities and, hence, thinner resists. This would have permitted a calibration curve with a lower range of optical densities. This may not have mattered, since initial trials indicated it was difficult to get good etches with selectivities above 1.5, but the knowledge would have at least enabled a decision to find and alternate vendor for the grayscale

DOE mask. It can definitely be said that Canyon Materials should consider putting small square features, perhaps 1-2 microns wide, on its calibration mask. Canyon Materials should also have been more forthcoming about the limits of its own mask fabrication process.

Other lessons, some of which were mentioned before, involved details of the fabrication process. One was the avoidance of photoresist melting and burning. Silicon etches are exothermic processes and consequently produce a fair amount of heat. Although MEMS-Optical performed the photolithography for the UAH array, some calibration work was done with thick photoresists in order determine the necessary feature heights for their photolithography. In order to prevent OCG 825 photoresist from melting and burning, a 4-minute soft-bake was required. This soft-bake is actually twice as long as recommended by the OCG 825 photoresist data sheet. Another important and valuable lesson was the idea of keeping the etch chemistry as simple as possible. Rather than three gases, only sulfur hexafluoride and oxygen were used to etch the second array series. Fewer variables/parameters in a fabrication process are conducive to better repeatability, and, as mentioned before, the trifluoromethane had a tendency to combine with the oxygen and reduce the resist etch rate. Instead of being etched away, the resist would just melt and burn. Finally, it was found that much lower RF power settings during etching gave rise to much better feature fidelity post etch. It transpired that by reducing the power to a third of its original setting, 175 Watts down to 50 Watts, improved feature fidelity was obtained.

4.2 Fabrication of UAH array

This section describes the process used in the production of the UAH beamfanner array. MEMS-Optical photolithography and the author’s etch process are covered.

4.2.1 MEMS-Optical grayscale photolithography

For the second array series, it was decided to contract a local company, MEMS-Optical, to perform the photolithography. This author's efforts at contact lithography with high feature fidelity were not yielding fruit, and MEMS-Optical was quite confident in its ability to achieve grayscale photolithography with lateral features as small as 3 square microns. Design specifications for the second array series required a minimum lateral feature dimension of 5 microns, since the author was confident of finding an etch process yielding good feature fidelity for this size.

Prior to submitting the array design to MEMS-Optical, fabrication trials were conducted with OCG 825 photoresist in an effort to obtain an etch selectivity curve for submission to MEMS-Optical. This was necessary, since the data sent to MEMS-Optical was given in terms of feature depths in silicon, and MEMS-Optical was performing photolithography without etching the silicon. Unfortunately, the best mask the author had for any kind of calibration was the HEBS beamfanner mask with its 27 rectangular pads. It should also be mentioned that since the MEMS-Optical photolithographic process was a company secret, it was not possible to actually use their resist and resist spinning/curing process for calibration. A process using the 825 resist was found that yielded a selectivity of around 1.3-1.4. MEMS-Optical was not enthusiastic about this, since their photolithographic process suffered less from diffractive blurring effects, which render poor feature fidelity, if their photoresist feature profile was thinner rather than thicker. The author's recommended maximum photolith feature height/etch-depth was 6 microns, and MEMS-Optical expressed dismay, as they were hoping for a depth of 2.5-3 microns for good photolithographic feature fidelity. It proved impossible, however, to achieve selectivities of 2.5-3 with good feature fidelity during the calibration research at UAH, and the author had to insist on the taller features.

The MEMS-Optical photolithographic process, since it is proprietary, cannot be described in great detail. It differs, however, significantly from the photolithography performed

by the author at UAH. Rather than using a contact mask aligner to expose the resist, MEMS-Optical uses a stepper. This is a device that illuminates the mask and then reduces the field of the mask with an intermediate set of optics located between the mask and the resist-coated substrate. The mask was aligned to a pair of crosses with 5-micron wide bars to the left and right of the silicon wafers supplied by the author. These marks were oriented +/- 3 centimeters horizontally from the center of the focal plane array. Each silicon wafer was coated with about 14 microns of resist, and the regions exposed to the UV light were developed. This left a pattern in the resist corresponding to the UAH beamfanner array.

The differences in the MEMS-Optical photolithographic process and the Nichols process were significant enough to render previous calibration efforts approximate at best. First of all, the Nichols photolithography left a photoresist device profile surrounded by an exposed silicon surface. The MEMS-Optical process left the device profile surrounded by a thick layer of resist. This is a significant difference in terms of etch chemistry, since exposed photoresist will use more oxygen while exposed silicon will use more sulfur hexafluoride during the RIE etching process. Secondly, the presence of more photoresist reduced the heat produced by the sulfur hexafluoride/silicon reaction, and this had the benefit of reducing the effects of melting and burning. This in turn helped yield greater post-etch feature fidelity. In the final analysis, even though accurate calibration was not possible before MEMS-Optical constructed the grayscale mask, post production etch calibration of their high quality photolithography allowed the development of an etch process that yielded reasonable results discussed in Section 4.6.

Presented in Figures 4.3 through 4.7, on the following pages, are SEM images of a variety of beamfanners from the MEMS-Optical photolithography and the resulting etched products. Profilometry and SEM imaging provide a combination of tools useful in evaluating how well fabrication has approximated design.

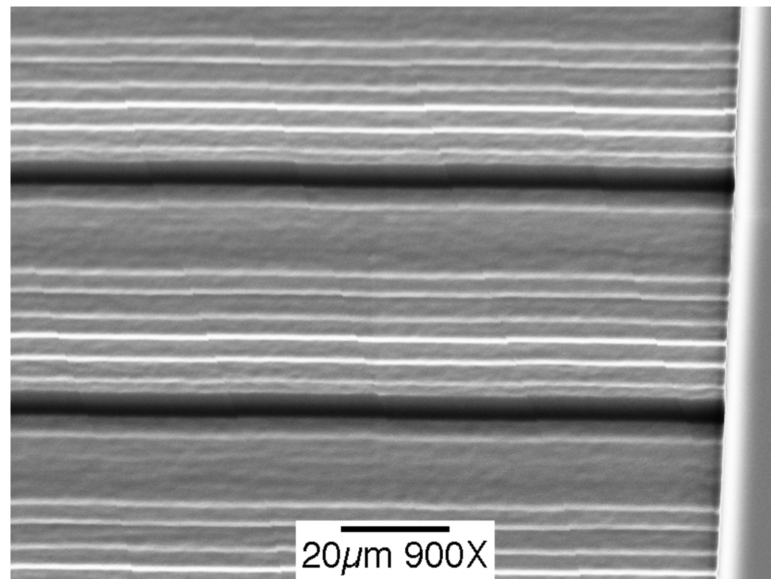

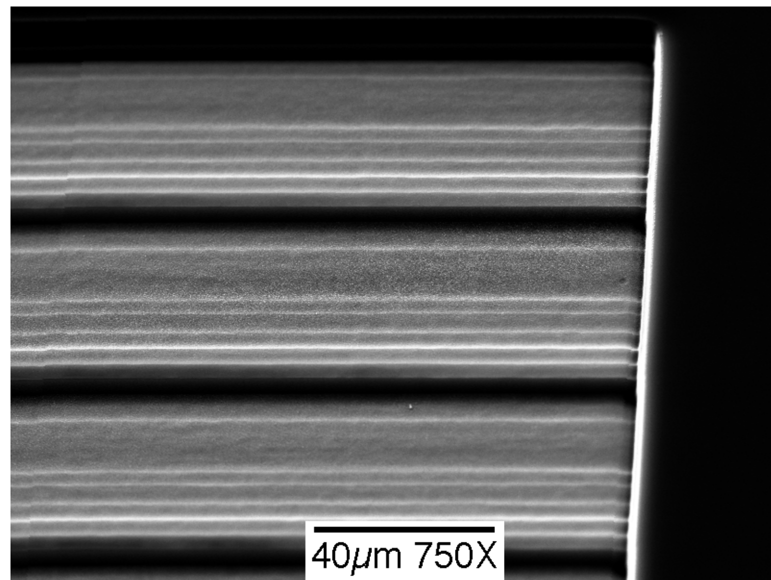

Figure 4.3 View of a side-pixel 1-2 beamfanner array with 5-micron lateral feature sizes and 64 phase levels in resist (top) and etched in silicon (bottom).

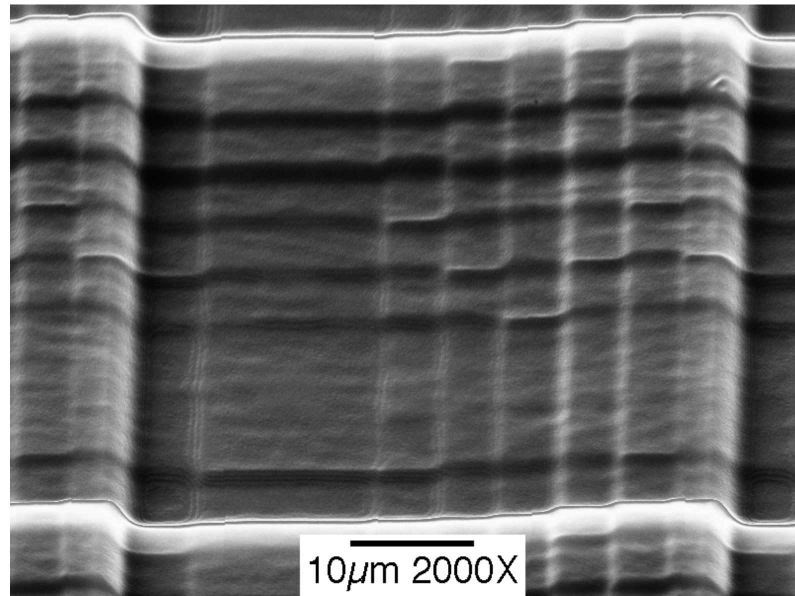

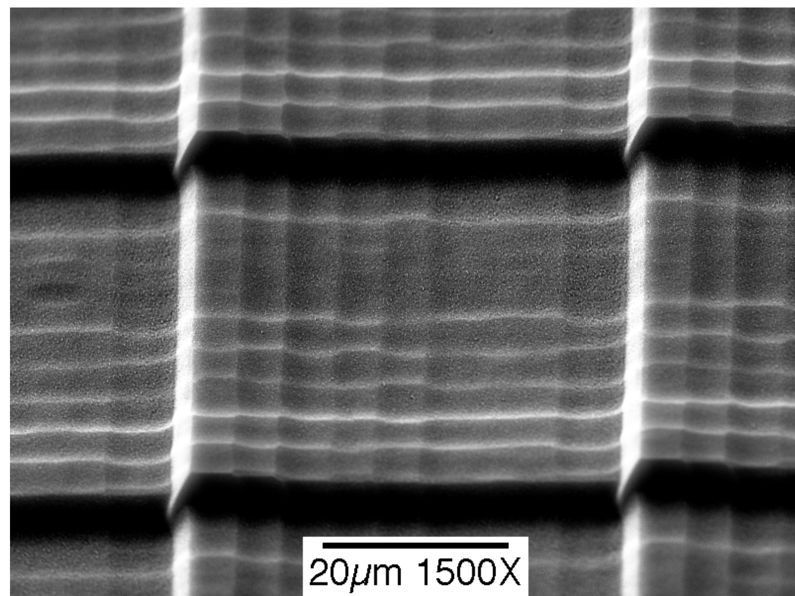

Figure 4.4 View of a corner-pixel 1-4 beamfanner with 5-micron lateral feature sizes and 64 phase levels in resist (top) and etched in silicon (bottom).

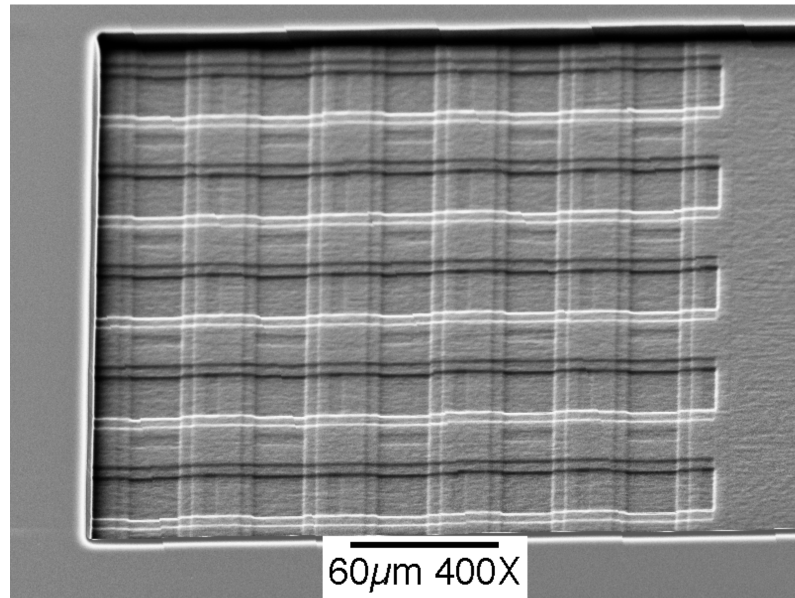

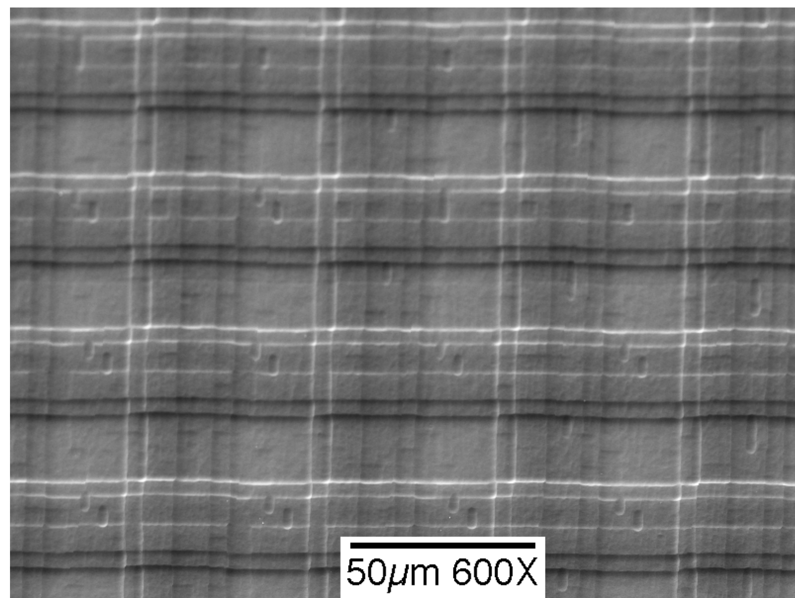

Figure 4.5 View of a center-pixel 1-4 beamfanner array with 5-micron lateral feature sizes and 64 phase levels in resist (top) and etched in silicon (bottom).

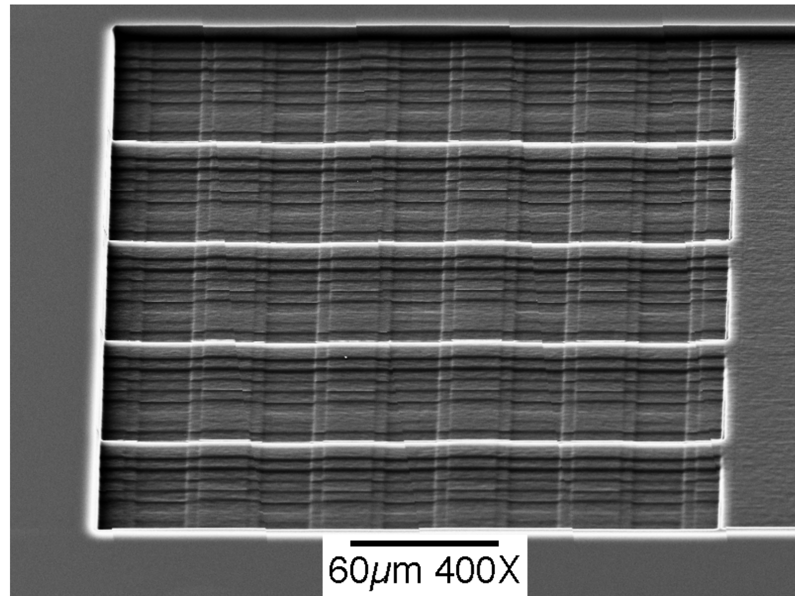

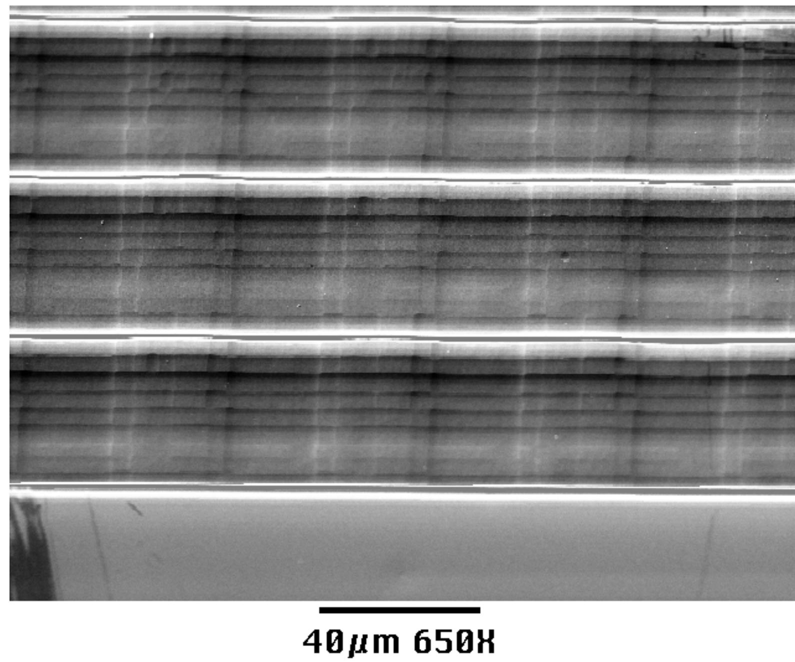

Figure 4.6 View of a side-pixel 1-4 beamfanner array with 5-micron lateral feature sizes and 64 phase levels in resist (top) and etched in silicon (bottom).

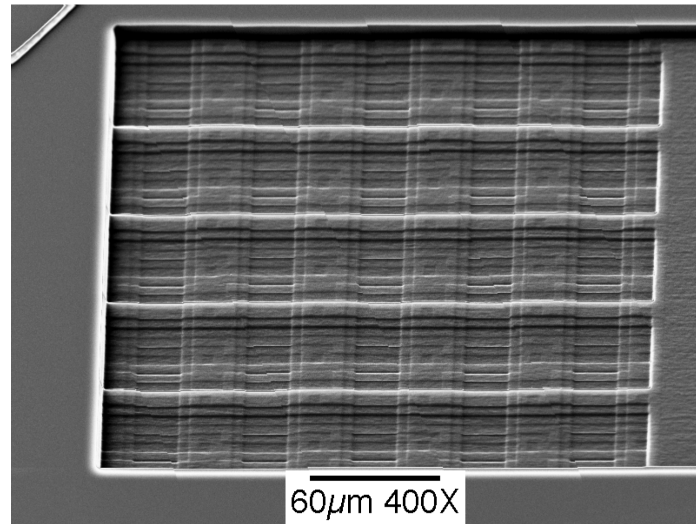

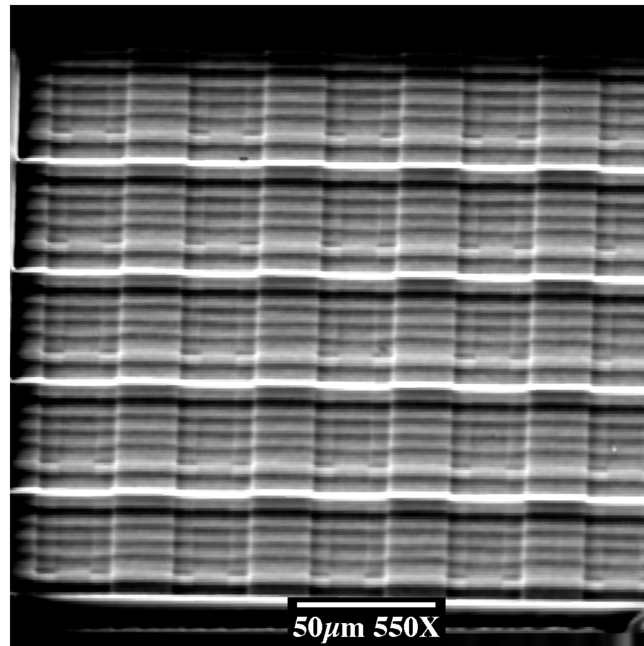

Figure 4.7 View of a middle-pixel 1-4 beamfanner array with 5-micron lateral feature sizes and 64 phase levels in resist (top) and etched in silicon (bottom).

Profilometer measurements yield etch-depths to a high degree of accuracy, and these are presented in the next chapter. Suffice it to say at this point that MEMS-Optical succeeded in providing photolithography where the features were within one percent of requested depth/feature height. SEM imaging allows a qualitative look at such matters as feature fidelity, where straight sidewalls, minimal surface roughness, and feature shape and sharpness are important. As a general observation, the MEMS-Optical photolithographic feature fidelity was acceptable.

4.2.2 UAH array RIE etch

As mentioned in the last section, it was necessary to continue the etch calibration process after MEMS-Optical had begun supplying completed photolithographic wafers. A total of 50 wafers were requested, and it took 13 of them to finally settle on an etch process. This 135 minute etch process called for a gas flow rate ratio of 15.3/19.0 sccm of oxygen/sulfur hexafluoride. The RF power was set at 50 Watts, and the RIE chamber pressure was maintained at 10 mT. The cathode temperature was set at 22 degrees Centigrade, and any deviation from this cathode temperature had a profound effect on etch selectivity. If the cathode was five degrees cooler, 17 degrees Centigrade, the selectivity dropped from 1.3 to 1.0.

Unfortunately, the prevailing chamber conditions were altered by intervening tasks, and the original etch recipe had to be modified again. The final process, which was used to produce 14 beamfanner arrays for both the repeatability study and performance testing, was of lesser merit than the preceding process on account of pitting of the silicon. This pitting was especially evident for features etched deeper than 3 microns. The recipe called for a 95 minute etch with a flow rate ratio of 16.2/16.1 sccm sulfur hexafluoride/oxygen, 16 mT pressure, 56 Watts RF power, and 22 degree centigrade cathode temperature.

Chapter 5

ANALYSIS OF ETCH SELECTIVITY AND REPEATABILITY

This chapter presents specifics of the experimental procedure and statistical analysis of selectivity, etch-depth, and feature position data garnered from this procedure. In order to achieve a reliable experimental procedure, careful controls had to be imposed on both etching procedure and the measurement of the etch-depths.

When placing samples in the RIE chamber, it was necessary to position the samples in the same spot and at the same angular orientation each and every time. It was also necessary to keep environmental conditions in the chamber as constant as possible throughout the process. This required an uninterrupted, two-week span of time where no other etch chemistries were used save for the specific chemistry necessary for the second beamfanner array series project.

Each individual beamfanner array has the same set of features, and this permits an important experimental procedure known as blocking [47]. Blocking allows a large set of parameters, in this case all feature etch-depths and selectivities in question, to be affected by the same etch process and, hence, the same chamber conditions at the same time. Each individual etch process represents a block in this study, while all individual feature depths and selectivities within a block represent treatments affected simultaneously by a single etch process.

For the purpose of this study, the variation between individual etch processes will define the merit of process repeatability. Separation of the between-process variation from the variation of individual features within each process, and in turn, the separation of these two variations from the residual error, is achieved using a statistical blocking method presented in the next section.

This statistical blocking method will enable an analysis of a possible relationship between feature selectivity and feature etch-depth.

There are 14 etch-process blocks of 40 individual features per block, and this required a total of 560 individual feature measurements of both feature photolith-depth and etch-depth. Each etch-depth was divided by each corresponding photolith-depth to yield the individual feature selectivities. This arrangement permits the experiment and subsequent statistical analysis to correlate any drift in one set of feature attributes, such as selectivities or etch-depths, with the drift in a different set or sets of feature attributes over a multiple number of etches. For example, one can determine, averaging over a series of 14 etches, if a planned 2-micron deep feature's selectivity has the same variance and standard deviation as a planned 3-micron deep feature's selectivity. Analysis of selectivity will be the main focus of the repeatability study, since a highly repeatable etch process should yield selectivity values that are nearly the same for corresponding features in each block.

In order to make an effective statistical analysis of the fabrication process, it has to be remembered that only a small number of data points per individual etch process can be used. Furthermore, there exists no large body of data from which a population mean, population variance, or population standard deviation for any parameter can be compared to the sample values obtained in the experiment. For the purpose of comparing pairs of parameter variance sets, the F-test method is employed [47]. The F-test has the advantage of not relying on a large body of pre-existing data, but it requires the ratio of two variances and the assumptions of random sampling and normal distribution of residuals about zero. It is a simple matter to check graphically for the normal distribution of residuals, and as will be demonstrated in the following section, this is a safe assumption for this study. The random sampling assumption is based on the fact that each set of features is etched at the same time within a single block and are hence interchangeable in position over the region of the wafer being etched. Any possible exceptions to this assumption must be carefully sought, observed, and noted. After careful inspection, the

belief of this author is that while feature attributes may vary with etch-depth, they do not vary with substrate position and can be considered interchangeable. The evidence will be presented graphically in the following sections of this chapter.

All measurements were taken with a Tencor P-10 Surface Profiler (Serial # 11980440). The stylus of this profilometer has a 3-micron radius, and it transpired that accurate feature depth measurements could only be taken from the 10-micron lateral feature 1-2 beamfanners. Beamfanners with smaller lateral feature sizes, however, proved unreliable for measurement, since the size of the stylus was comparable to the size of the features. A cross-sectional scan of every 10-micron lateral feature size 1-2 beamfanner, located at the center of each 1×5 1-2 array, was taken 50 microns from the top of each array. As mentioned previously, this yielded 40 data points per sample, for a total of 560 data points over 14 etch processes. Actual feature depth data was measured from the lateral midpoint of the highest feature to the lateral midpoint of the other features in each of 12 beamfanners examined per sample, as shown in Figure 5.1.

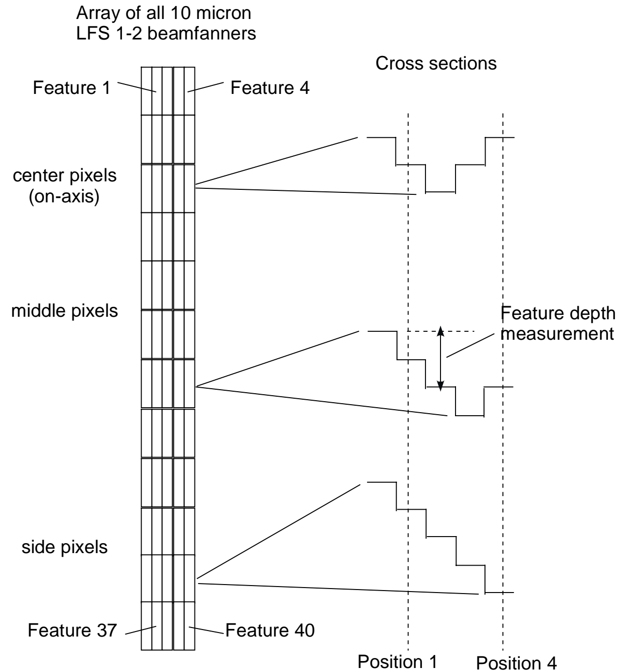

Figure 5.1 Column of 10-micron lateral feature size 1-2 beamfanners (corresponds to array p5 in Chapter 3, Figure 3.10) measured with a profilometer for each of 14 samples. Profilometry was conducted over cross-sections similar to those shown to the right of the array in the diagram.

This yielded 4 measurements per middle off-axis and side off-axis beamfanner, but just two measurements per central on-axis beamfanner, due to its symmetric construction.

All necessary computation for the following analysis was performed using the Matlab program, Selectivitya, given in Appendix B, developed by the author.

5.1 Photolithography/etch/selectivity analysis

The MEMS photolithographic patterns were supposed to be designed for a selectivity of 1.3. The average selectivity necessary to obtain the design specification turned out, upon measurement, to be between 1.13-1.2, depending on individual feature depths. As mentioned before, circumstances prevented a more refined calibration curve from being developed, so all 40

individual photoresist feature depths, averaged over 14 MEMS-Optical photolithographic samples, were on the order of 0.8-0.91 the depth of the design feature etch specifications.

In Tables 5.1, 5.2, and 5.3 presented below, selectivities, photoresist depths, etch-depths, and their respective standard deviations, as well as design etch-depth specifications and the percentage difference between measured etch-depths and design specifications are given as averages over the 14 etch processes.

Table 5.1 Center -Pixel Data

Average feature photolith-depth (μ)	Average feature etch - depth (μ)	Selectivity	Standard deviation photolith-depth (μ)	Standard deviation etch-depth (μ)	Standard deviation selectivity	Desired feature etch - depth (μ)	% difference between average and desired feature etch-depth
0.65	0.74	1.15	+/-0.03	+/-0.06	+/-0.10	0.73	1.37
0.90	1.04	1.16	+/-0.03	+/-0.07	+/-0.08	1.02	1.96
0.65	0.74	1.13	+/-0.02	+/-0.07	+/-0.11	0.73	1.37
0.90	1.03	1.15	+/-0.03	+/-0.08	+/-0.10	1.02	0.98
0.63	0.72	1.16	+/-0.02	+/-0.08	+/-0.13	0.73	-1.37
0.89	1.04	1.16	+/-0.02	+/-0.09	+/-0.10	1.02	1.96
0.64	0.73	1.14	+/-0.01	+/-0.07	+/-0.11	0.72	1.39
0.89	1.04	1.17	+/-0.02	+/-0.07	+/-0.08	1.02	1.96

Table 5.2 Middle-Pixel Data

Average feature photolith-depth (μ)	Average feature etch - depth (μ)	Selectivity	Standard deviation photolith-depth(μ)	Standard deviation etch-depth (μ)	Standard deviation selectivity	Desired feature etch-depth (μ)	% difference between average and desired feature etch-depth
1.10	1.28	1.17	+/-0.03	+/-0.10	+/-0.09	1.26	1.59
1.59	1.85	1.17	+/-0.04	+/-0.12	+/-0.07	1.85	0.00
1.84	2.16	1.17	+/-0.05	+/-0.13	+/-0.07	2.16	0.00
1.61	1.89	1.18	+/-0.06	+/-0.11	+/-0.07	1.85	2.16
1.03	1.16	1.13	+/-0.03	+/-0.09	+/-0.08	1.15	0.87
1.74	2.01	1.16	+/-0.04	+/-0.14	+/-0.07	2.02	-0.50
1.81	2.11	1.17	+/-0.04	+/-0.14	+/-0.07	2.16	-2.31
1.60	1.87	1.17	+/-0.03	+/-0.13	+/-0.07	1.88	-0.53
1.03	1.16	1.13	+/-0.05	+/-0.10	+/-0.07	1.19	-2.52
1.77	2.04	1.15	+/-0.04	+/-0.13	+/-0.06	1.95	4.62
1.87	2.16	1.16	+/-0.05	+/-0.14	+/-0.05	2.16	0.00
1.80	2.09	1.16	+/-0.05	+/-0.14	+/-0.06	1.95	7.18
1.01	1.16	1.15	+/-0.03	+/-0.11	+/-0.10	1.17	-0.85
1.76	2.06	1.17	+/-0.04	+/-0.15	+/-0.07	1.96	5.10
1.85	2.17	1.17	+/-0.05	+/-0.15	+/-0.06	2.16	0.46
1.78	2.09	1.17	+/-0.06	+/-0.15	+/-0.06	1.95	7.18

Table 5.3 Side-Pixel Data

Average feature photolith-depth (μ)	Average feature etch-depth (μ)	Selectivity	Standard deviation photolith-depth (μ)	Standard deviation etch-depth (μ)	Standard deviation selectivity	Desired feature etch-depth (μ)	% difference between average and desired feature etch-depth
1.46	1.69	1.16	+/-0.04	+/-0.14	+/-0.08	1.65	2.42
2.23	2.61	1.17	+/-0.06	+/-0.19	+/-0.07	2.74	-4.74
2.66	3.13	1.17	+/-0.07	+/-0.22	+/-0.06	3.29	-4.86
3.16	3.72	1.18	+/-0.09	+/-0.26	+/-0.06	3.84	-3.13
1.30	1.47	1.13	+/-0.04	+/-0.13	+/-0.08	1.53	-3.92
2.42	2.82	1.16	+/-0.07	+/-0.21	+/-0.06	2.82	0.00
2.94	3.43	1.17	+/-0.09	+/-0.25	+/-0.06	3.59	-4.46
3.15	3.70	1.17	+/-0.09	+/-0.27	+/-0.06	3.84	-3.65
1.29	1.51	1.17	+/-0.06	+/-0.13	+/-0.09	1.61	-6.20
2.39	2.81	1.17	+/-0.08	+/-0.20	+/-0.06	2.85	-1.40
2.91	3.45	1.18	+/-0.09	+/-0.25	+/-0.06	3.59	-3.90
3.15	3.71	1.18	+/-0.10	+/-0.27	+/-0.06	3.84	-3.39
1.25	1.46	1.17	+/-0.03	+/-0.11	+/-0.08	1.59	-8.18
2.39	2.80	1.17	+/-0.07	+/-0.20	+/-0.06	2.81	-0.36
2.92	3.45	1.18	+/-0.08	+/-0.24	+/-0.06	3.54	-2.54
3.20	3.75	1.17	+/-0.09	+/-0.27	+/-0.06	3.84	-2.34

There was some error in the photolithography, as the individual photolith features had standard deviations ranging from +/- 0.01-+/-0.10 microns. The center/on-axis beamfanners' average feature etch-depth is within 0-2 percent of design specification, but the middle and side off-axis cases were as much as 8 percent off the specifications for some features. Many of the features with etch-depths in the range of 1.5-3 microns deviated over 4 percent different from the design specifications. It is also possible to infer that a relationship exists between selectivity and etch- depth, for in many cases the selectivity increases with increasing etch-depth. However, due to the rather large variance of the data, it is not prudent to demand a quantitative functional

relationship, such as one that could be gained through a curve fit, between these parameters. The large variance of the measured etch-depths also yields a situation where a relatively small number of individual beamfanners is close enough to design specifications to consider testing.

The next section will provide a detailed analysis of the selectivity variance and a discussion of what this variance means for process repeatability and possible trends relating to selectivity, etch-depth, process order, and cross-sectional substrate position.

5.2 Process repeatability and trends based on analysis of selectivity as a function of etch process and individual feature attributes

The first step in this analysis, and the step most critical to establish a merit of repeatability, consists of examining the ratio of the variance between the average selectivities of the 14 etch processes and the within-etch variance between the individual feature selectivities. This comparison establishes whether or not the variance of the selectivities of the 14 etch processes is significantly greater than that of the between-feature selectivity variance. If it is not significantly greater, then the process can be deemed repeatable allowing for the variations between the selectivities of individual features within each etch. If it is significantly greater, however, the etch process is characterized with a lower degree of repeatability.

Variance, s^2, is defined as the sum of squares of n residuals, indexed individually as $(y_i - \bar{y})$, divided by the number of degrees of freedom permitted for that group of residuals. The variable $\bar{y}$, in this case, is the average of the n quantities, y_i. The appropriate expression is given in Equation (5.1).

$$s^2 = \frac{\sum_{i=1}^{n}(y_i - \bar{y})^2}{n-1}. \tag{5.1}$$

The quantity in the denominator, $n-1$, which is the number of degrees of freedom, arises, since the sum of all residuals must equal zero. This means that only $n-1$ quantities can be arbitrarily varied. Standard deviation, which is the square root of the variance, $+/- s$, is also a useful quantity to characterize the spread in the data.

The measured selectivity data was arranged in array form with i indexing the 40 rows representing the forty features examined per etch process and t indexing the 14 columns representing the 14 etch processes. The measured selectivity of the i th feature within the t th etch process, y_{ti} (560 degrees of freedom), can be decomposed into a mean, η, a between-etch process error, τ_t, and a within-etch process error, ε_{ti}, as shown in Equation (5.2).

$$y_{ti} = \eta + \tau_t + \varepsilon_{ti} . \tag{5.2}$$

This can be further considered as the expression in Equation (5.3), where $\overline{y}$ is a grand average (1 degree of freedom) of all individual selectivity measurements, and $\overline{y}_t$ (14 degrees of freedom) is the average selectivity value of the t th etch process averaged over the 40 features.

$$y_{ti} = \overline{y} + \left(\overline{y}_t - \overline{y}\right) + \left(y_{ti} - \overline{y}_t\right) . \tag{5.3}$$

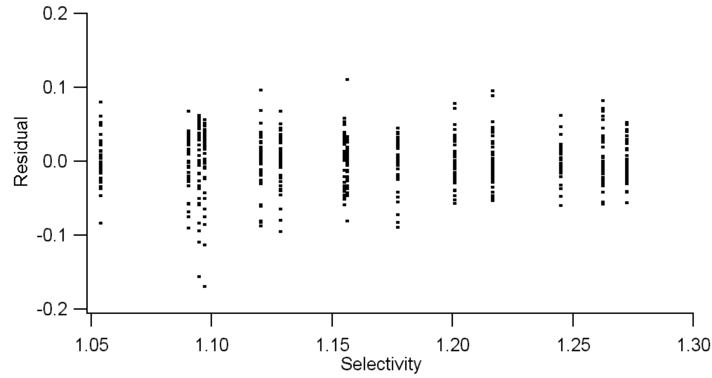

Figure 5.2 Plot of residual selectivity error vs. expected selectivity values for the 14 processes.

In Figure 5.2, the within-etch process residuals, $y_{ti} - \overline{y}_t$, are plotted as a function of the expected values of the selectivies, $\overline{y} + (\overline{y}_t - \overline{y})$. The residuals have a fairly normal distribution about zero for all 14 etch processes, with most residual values within the range of +/- 0.05. This and the random sampling assumption, as previously noted, encourage the use of an F-test to compare the between-etch variance to the within-etch variance by taking a ratio of these variances.

The general expression for an F-distribution [48], valid for all x>0, is given by Equation (5.4),

$$f(x) = \left\{ \frac{\Gamma\left(\frac{n_1 + n_2}{2}\right)}{\Gamma\left(\frac{n_1}{2}\right)\Gamma\left(\frac{n_2}{2}\right)} \times \left(\frac{n_1}{n_2}\right)^{(n_1/2)} x^{(n_1/2)-1} \left(1 + \frac{n_1}{n_2} x\right)^{-(1/2)(n_1+n_2)} \right. . \tag{5.4}$$

The gamma function is given by the relation, $\Gamma(n)=\int_0^\infty t^{n-1}e^{-t}dt$ for n>0. The parameters n_1 and n_2 represent the number of degrees of freedom for each variance, and the ratio of two compared variances will equal an x value corresponding to a lower bound on the remaining area under the curve defined by $f(x)$. An x value yielding a significance level of 5%, for example, means that the area under the curve defined by $f(x)$ for all values greater than x is 5% of the total area under the curve. For this analysis, any significance level lower than 5% will imply that the first variance (numerator) is significantly greater than the second variance (denominator). This in turn implies that the first variance cannot be attributed to factors bringing about the second variance. Tabulated significance level values for F-distributions as a function of x, n_1, and n_2 can be found in [47].

The variances, as noted before, are the sum of squares of each set of residuals divided by the number of degrees of freedom for each set of residuals. The ratio of the between-etch process variance to the within-etch process variance, which is given by Equation (5.5),

$$s_{bt}^2 \big/ s_{wt}^2 = \sum_{t=1}^{14}(40)(\bar{y}_t-\bar{y})^2/13 \Big/ \sum_{t=1}^{14}\sum_{i=1}^{40}(y_{ti}-\bar{y}_t)^2/546, \tag{5.5}$$

is equal to 146. This value, when plotted against the appropriate F-distribution, with n_1 = 13 and n_2 = 546, has a significance level below 0.1%. It can therefore be stated that the spread in the selectivity between the 14 processes is much larger than the spread in the selectivity within those processes. This implies a low level of process repeatability. The standard deviation for between-etch process selectivities, s_{bt}, is +/- 0.07, and the standard deviation between individual feature selectivities within the etch processes, s_{wt}, is +/- 0.015. The only plausible explanation that can be offered for the large spread in selectivities between the 14 etch processes is that the RIE DC

bias voltage fluctuated approximately +/- 2% during each etch. No other possible contributing factor was observed, but, as mentioned previously, the etch process can be very sensitive to small parametric variations.

Though the level of process repeatability is not has high as desired, there are other issues worth investigating which can be examined with a more refined analysis. One issue, mentioned previously, is the relationship between the selectivities and etch-depths of the individual features. Another is the relationship between feature selectivities and feature position on the array. In order to examine these issues effectively, the separate etch processes are treated as blocks, and the individual features within each block are considered to be treatments. This allows the variation due to the separate etch processes to be separated from the variation due to the differences in selectivity between the 40 features within each etch process. It also allows a residual error to be separated from these two sets of varying selectivities. Equation (5.6) shows each individual selectivity, y_{fi}, represented as the sum of an average selectivity, η, plus an etch process selectivity error, or block, error, β_i, plus an individual feature selectivity error, τ_f, plus a residual error, ε_{fi}.

$$y_{fi} = \eta + \beta_i + \tau_f + \varepsilon_{fi}. \qquad (5.6)$$

The f indexes the 40 individual features in each block, and the i indexes the 14 separate blocks, or etch processes. Note that τ, which represented average selectivities for individual processes in the preceding examination of process repeatability, now represents individual feature selectivities averaged over the 14 processes. This formulation makes it possible to separate individual feature selectivity variance from block variance and compare the individual feature selectivity variance to the variance of the residual error. If the former is significantly greater than the latter, a real difference between individual feature selectivities, not attributable to the residual

error, is implied. If the significance of such a difference can be established, it becomes sensible to investigate its relationship to the other parameters, etch-depth and position, already mentioned.

$$y_{fi} = \overline{y} + (\overline{y}_i - \overline{y}) + (\overline{y}_f - \overline{y}) + (y_{fi} - \overline{y}_i - \overline{y}_f + \overline{y}) . \tag{5.7}$$

Equation (5.7), above, shows the decomposition of the data analogous to Equation (5.6). y_{fi} (560 degrees of freedom) represents the measured selectivity of the f th feature in the i th etch process, $\overline{y}$ (1 degree of freedom) is the grand average of all measured selectivities, $(\overline{y}_f - \overline{y})$ (13 degrees of freedom) is the deviation of the f th feature average over the 14 individual etch process selectivities from the grand average, and $(\overline{y}_i - \overline{y})$ (39 degrees of freedom) is the deviation of the i th etch process selectivity average over the 40 individual feature selectivities from the grand average. $(\overline{y}_{fi} - \overline{y}_i - \overline{y}_f + \overline{y})$ (507 degrees of freedom) is the residual error for the f th feature selectivity in the i th etch process.

Of interest are plots of the residual errors against the expected values of selectivity, array position, and etch-depth. Figure 5.3 shows a plot of residual selectivity error, $(\overline{y}_{fi} - \overline{y}_i - \overline{y}_f + \overline{y})$ as a function of the expected value of the selectivity, $\overline{y} + (\overline{y}_i - \overline{y}) + (\overline{y}_f - \overline{y})$.

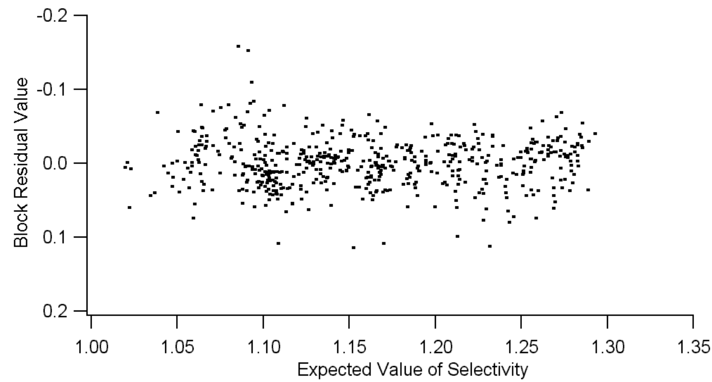

Figure 5.3 Plot of block residual selectivity error vs. expected selectivity values.

It can clearly be seen that the residual selectivity error is distributed in a normal, random fashion about zero for the full range of expected selectivities. This implies that experimental error is not a function of selectivity.

Figure 5.4 shows a plot of the residual selectivity error vs. the time order, 1-14, in which the processes were performed.

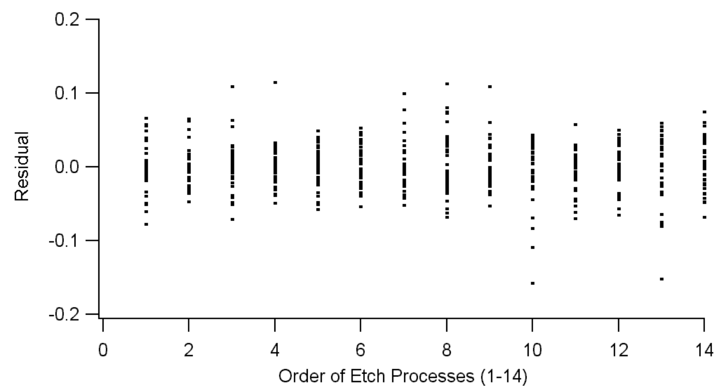

Figure 5.4 Plot of block residual selectivity error vs. the order in which the processes were performed.

This plot shows no real trend in the spread of the residual selectivity error over the 14 processes. This simplifies the analysis by eliminating the possibility that the author's experimental technique was altered over the time period that the selectivity measurements were obtained.

Figure 5.5 shows a plot of residual selectivity error vs. for the 40 features' etch-depths averaged over the 14 etch processes.

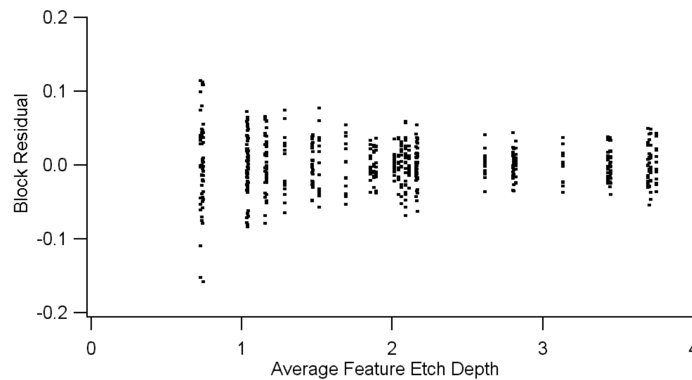

Figure 5.5 Plot of block residual selectivity error vs. average feature etch-depth in microns.

The residuals are plotted in a distribution that is close to normal about zero, but the spread of the residuals about zero is larger, as much as +/- .15, for the feature depths under 2 microns than the ones between 2.0-3.7 microns, which are closer to +/- .07. This appears to be due to greater variability in the surface relief of the higher features. This is likely due to a slightly melted, uneven photoresist profile being etched into the surface of the silicon. This, as discussed before, is a common problem with the features covered by thicker coats of resist.

Figure 5.6 shows a plot of the residual selectivity error vs. the lateral position, 4 features/40 microns wide.

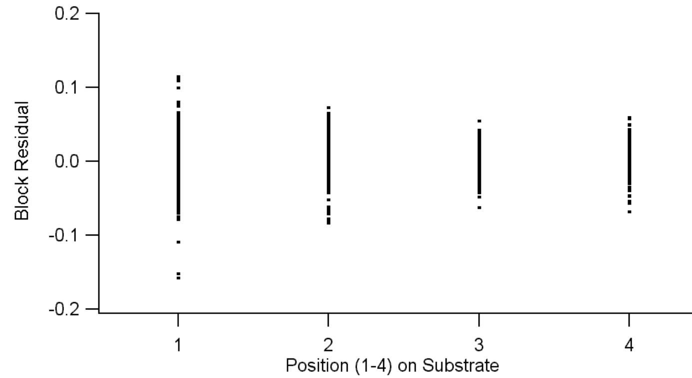

Figure 5.6 Plot of block residual error vs. lateral position on the substrate.

Again, the distribution of residuals is normal about zero in appearance. The first feature (position #1), shows a significantly greater spread, +/-0.1, than the other 3, which are on the order of +/-0.05. Since the first position also corresponds to the smallest etch-depths, it is again not surprising that its spread is greater than the others.

It is this spread in the residual error data that makes an attempt at relating selectivity and etch-depth somewhat problematic. In spite of this, the F-test comparing the variance of the 40 individual feature selectivities from the grand average, s_f^2, to the residual selectivity error, s_r^2, is performed. The variance ratio is given in Equation (5.8).

$$s_f^2 \big/ s_r^2 = \sum_{f=1}^{40}(14)\left(\bar{y}_f - \bar{y}\right)^2 / 39 \Bigg/ \sum_{i=1}^{14}\sum_{f=1}^{40}\left(y_{fi} - \bar{y}_i - \bar{y}_f + \bar{y}\right)^2 / 507\,. \tag{5.8}$$

This ratio equals 2.48, and the F table makes this result significant between the 1% and the 0.1% level. This indicates that there is a variation in selectivity between the 40 features that isn't attributable to the residual selectivity error. With this information, it is reasonable to check if there is a relationship between selectivity and etch-depth or feature position on the substrate.

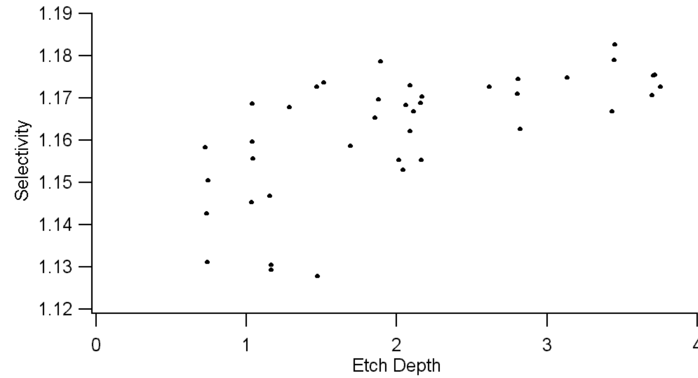

Figure 5.7 Plot of selectivity vs. mean feature etch-depth.

Figure 5.7 shows the 40 feature selectivities, averaged over the 14 etch processes, as a function of etch-depth, also averaged over the 14 etch processes. Note that the lower etch-depths, 0.7-2.0 microns, exhibit a larger spread in selectivity, 1.13-1.18, than the deeper etch-depths, 2.0-3.7 microns, which vary from 1.14-1.18. The spread of the selectivity data at the lower etch-depths is predicted by the spread in residual selectivity error examined previously. Selectivity appears to increase with etch-depth, but there is a larger spread in the data for the lower selectivities than the higher selectivities.

A final detail is presented in Figure 5.8, where the average selectivity, taken over the 14 processes, is plotted as a function of lateral feature position.

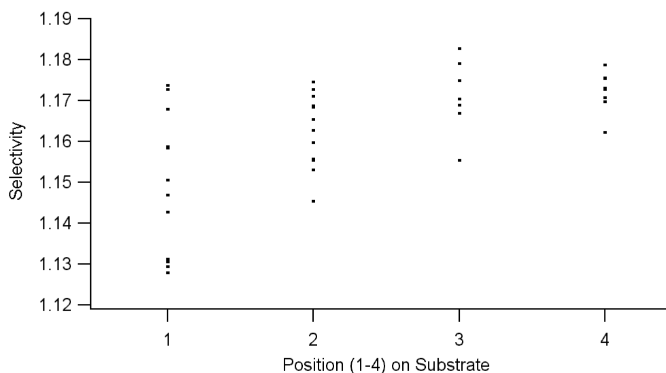

Figure 5.8 Plot of mean selectivity of each of 40 features vs. lateral position on substrate.

Selectivity appears to increase as a function of lateral position, but it is hard to imagine RIE chamber conditions deviating so drastically over a linear range of 40 microns, which is the center-to-center distance between the side features of each beamfanner examined. With this in mind, selectivity is likely not a function of lateral feature position. It is most probable that Figure 5.8 mirrors the trend of Figure 5.7, since etch-depth, in general, increases with lateral position.

Concluding this chapter, it is clear that process repeatability is poor, though average feature etch-depths on a few of the samples were within two or three percent of the design specification. Though selectivity and etch-depth appear to be increasing functions of each other, the variation in the data obscures a safe attempt at a quantitative correlation. The fact that the shallower etches tended to be more rounded than the deeper etches explains the spread in the selectivity data for the shallower etch-depths. This is because rounding gives rise to more uncertainty in profilomiter measurements. Figure 5.9, at the end of this chapter, shows that the higher features are rounded for both the resist profiles and the silicon profiles. This may also be responsible for the apparent selectivity/etch-depth relationship, since the higher features tend to become even more rounded in the silicon post etch.

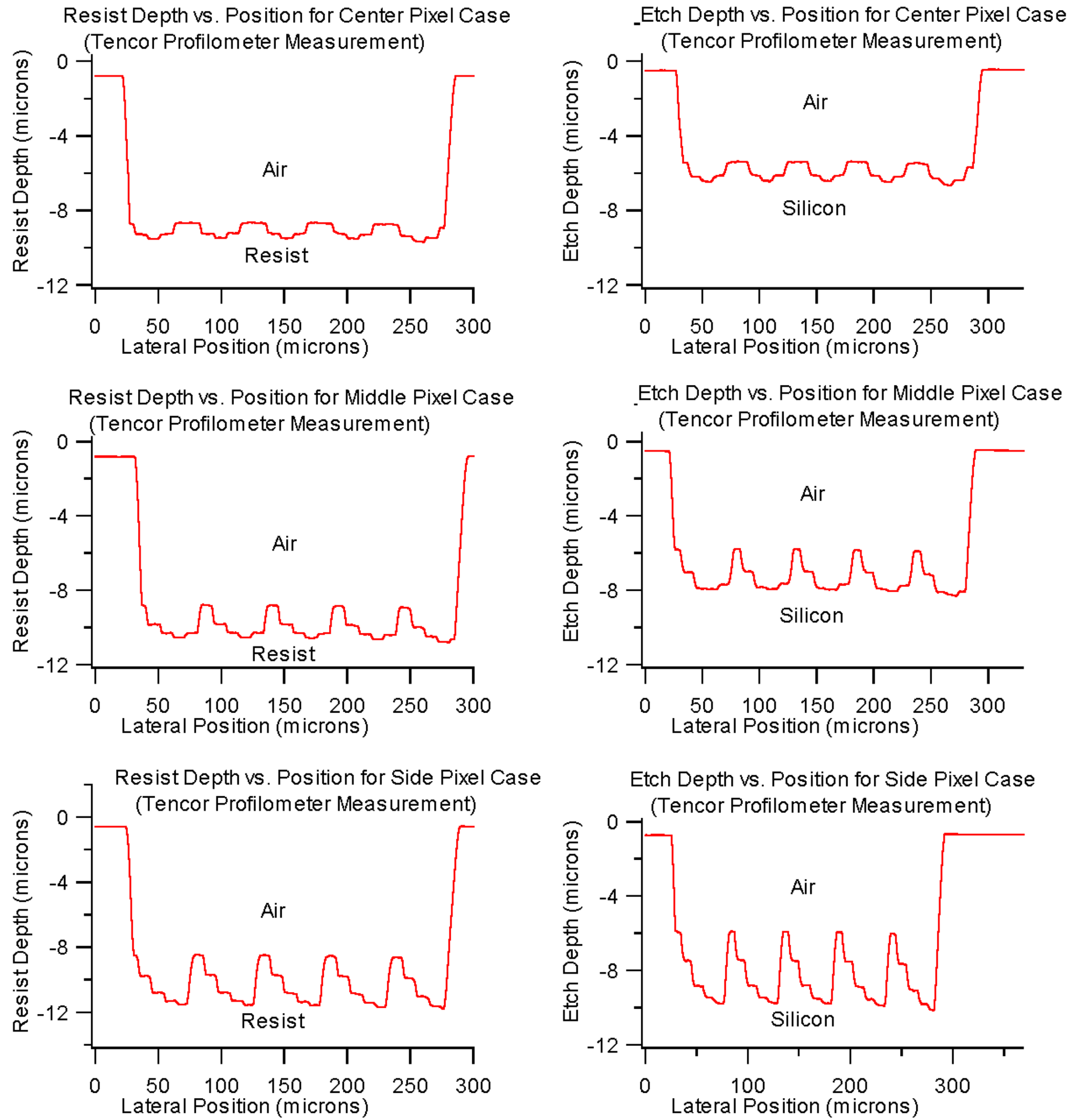

Figure 5.9 Profilometer measurement plots of cross-sections of 5 adjacent 1-2 beamfanners for center-pixel (top), middle-pixel (center), and side-pixel (bottom) cases for resist profiles (left column) and etch profiles (right column).

Chapter 6

TESTING OF DEVICES

Beamfanner testing addresses the optical performance of both the 1-4 beamfanner arrays and the 1-2 beamfanner arrays. The 1-4 arrays are examined using an IR microscope provided by CSC/Nichols Research Corporation, and the 1-2 arrays are examined using a cylindrical lens system purchased by UAH along with the IR camera provided by Nichols.

The alignment procedure necessary to prepare the beamfanner arrays for testing is outlined in Section 6.1. Alignment of the MEMS-Optical photolithography to the silicon wafers and the alignment of the finite apertures to the 1-2 beamfanner arrays are covered.

The testing results of the 1-4 arrays, originally intended to be part of the integrated focal plane array (FPA) described at the beginning of Chapter 1, are discussed in Section 6.2. The testing results of the 1-2 arrays are discussed in Section 6.3. Section 6.4 examines the attempt to fabricate a fully integrated FPA.

6.1 Alignment procedure for finite apertures and MEMS-Optical photolithography

An alignment procedure is necessary for the proper positioning of the photoresist pattern with respect to the substrate as well as the finite apertures with respect to the 1-2 beamfanners. Figure 6.1 shows one such finite aperture positioned over a 1-2 beamfanner array.

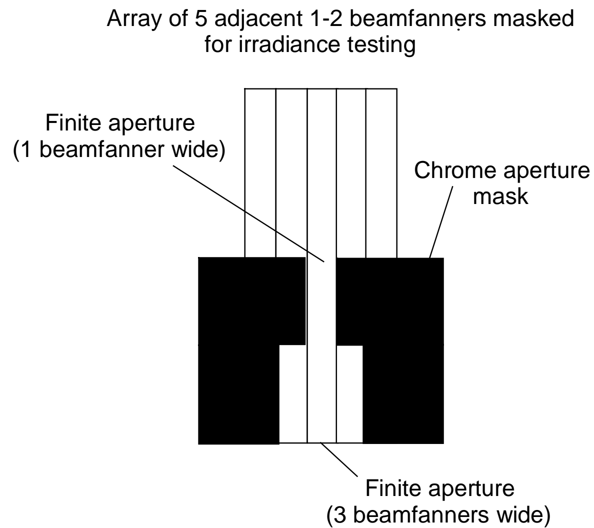

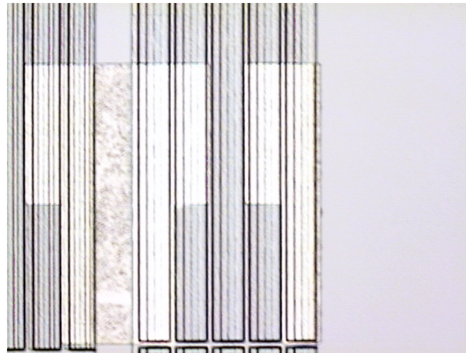

Figure 6.1 Finite aperture masks oriented to an array of 5 adjacent 1-2 beamfanners. A microscope image is shown at the bottom.

Figure 6.1 shows a 1×5 array of 1-2 beamfanners that is masked by a chrome aperture for one half of its length. This aperture is actually a dual aperture, for part of it shields all but the center beamfanner, and part keeps the three adjacent central beamfanners exposed. This scheme allows a comparison between the output of a single beamfanner and a beamfanner with cross-talk

contribution from its two nearest neighbors. Each chrome pad is 375 microns long, and there are 60 of them positioned in such a way to cover all of the 1-2 beamfanner arrays.

The photomasks used in the alignment of these pads to the beamfanner arrays are standard chrome-on-quartz and are produced by Photosciences, Inc. of Torrance, California. The masks were designed with cad software called L-Edit. They are dark field, binary chrome-on - quartz masks, with light areas corresponding to the beamfanner apertures and various alignment marks. The finite apertures are transferred to the beamfanner arrays using a photomask called Focpadfront, which must be aligned to a pattern in the silicon created by a photomask called Aligncross.

The Aligncross pattern is transferred to a silicon wafer coated with Shipley 1805 photoresist. After exposure and development, a SF_6 etch followed by an oxygen descum leaves the Aligncross pattern imprinted in the silicon wafer. For the FPA described in Section 6.4, the grids on the Aligncross mask must be aligned to a set of grids on the opposite side of a wave plate/polarizer array. Aligncross also transfers another set of marks, a pair crosses with 5-micron thick arms spaced +/- 3 mm along the horizontal through the main 1-4 beamfanner array, to which MEMS-Optical aligns its photolithography.

Chrome pads that serve as the finite apertures are deposited in a process commenced by UV exposure of a beamfanner array coated with photoresist through the finite aperture mask, Focpadfront. Focpadfront is aligned to the array with a set of 80-micron square alignment grids centered on a second set of 90-micron square grids already imprinted in the silicon with Aligncross.

Development of the resist leaves areas of bare silicon where the apertures are to be located. An RF sputterer is used to deposit chrome over the resist and aperture regions. A lift-off is then performed, where the chrome coated sample is placed in an ultrasonically agitated photoresist solvent called 1165 Remover, produced by Shipley. The photoresist under the chrome dissolves, and the only chrome that doesn't slip off of the sample is located in the regions

where it is in contact with silicon, i.e., the aperture pads shown in Figure 6.1. Figure 6.2 shows the alignment scheme.

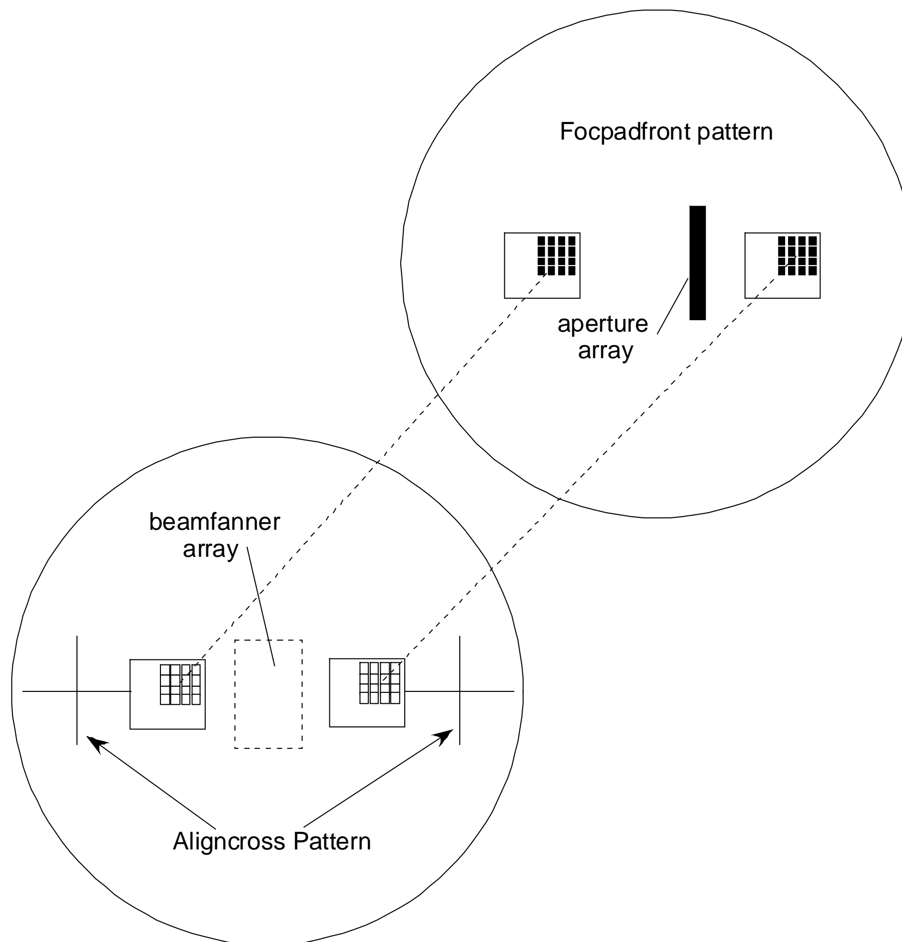

Figure 6.2 A not-to-scale view of the alignment patterns used to place the finite apertures on the beamfanner array. The Aligncross pattern also aligns to the back-side of the integrated waveplate-polarizer array.

6.2 IR microscopy testing of the 1-4 beamfanner arrays (Nichols Research)

Nichols Research Corporation allowed the author to borrow an IR microscope to test the 1-4 beamfanner arrays. This microscope consists of a collimating lens and a focusing lens, plus an IR camera to view the light transferred through the system. As shown in Figure 6.3, a heat lamp serving as an IR source is mounted before a 5-micron filter and an aperture in the focal plane of the first lens. Light is collimated by the first lens and propagated to the second lens, which is then focused onto the beamfanner array. The silicon wafer with the etched beamfanner array is mounted on a vacuum chuck. The IR camera is positioned beyond the sample to view the output light and is connected by cable to a video output. By opening the aperture to allow off-axis illumination, it was possible to illuminate the entire main 1-4 beamfanner array.

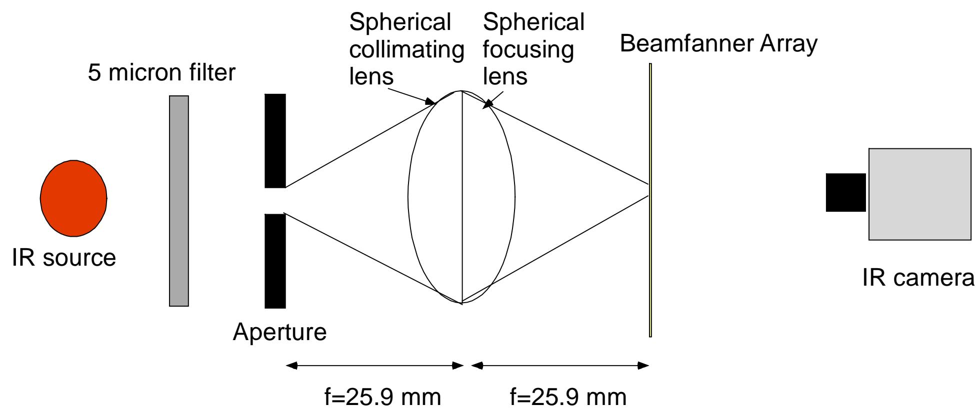

Figure 6.3 Configuration for optical testing of beamfanners. The lens system for the 1-4 beamfanner illumination was provided by Nichols/CSC.

Limited testing performed on the 5×5 1-4 arrays showed that the 6-micron lateral feature size, 8 phase level case demonstrating some 1-4 splitting. This particular device had final beamfanners close enough to design specifications, which is with feature depths within 2% of

design etch-depth, to consider testing the main 1-4 beamfanner FPA. Apparent 1-4 splitting was observed with this sample, but the splitting was not seen in the plane 340 microns from the input side of the beamfanner array. It was seen, rather, approximately 100 microns from the input side. Figure 6.4 shows the diffraction pattern of a 1-4 beamfanner. This particular beamfanner is located in the upper left hand corner of the FPA. The large lobes, separated by 50 microns, correspond to the corners of the beamfanner, while the smaller central lobes, separated by 25 microns, are similar to the desired 1-4 split beam pattern.

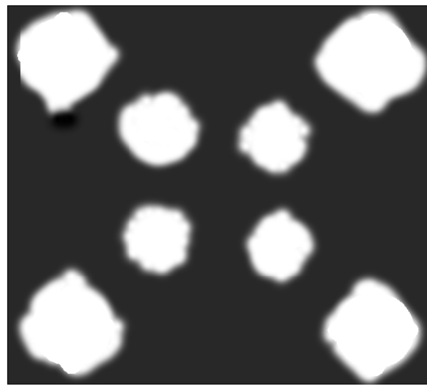

Figure 6.4 A drawing of the diffraction pattern of a 1-4 beamfanner.

6.3 Comparison of observed beamfanner performance with predicted (BEM) performance for the 1-2 beamfanner arrays

It was hoped that testing of the 1-2 beamfanners would yield performance similar to that predicted by BEM as presented in Chapter 3. The configuration of testing equipment is the same as for the 1-4 beamfanners, Figure 6.3, with the exception that two cylindrical lenses are substituted for the lens system supplied by Nichols, and rather than a circular aperture, a slit is

used to illuminate the system. The cylindrical lenses are f/2 with a focal length of 25.9 mm. They are plano-convex lenses and, as shown in Figure 6.5, are placed back-to-back in the optical system to simplify alignment. The middle and side-pixel 1-2 beamfanner illumination is achieved by tilting the beamfanner array at angles of 7 and 14 degrees respectively, simulating the necessary off-axis illumination for which they are designed.

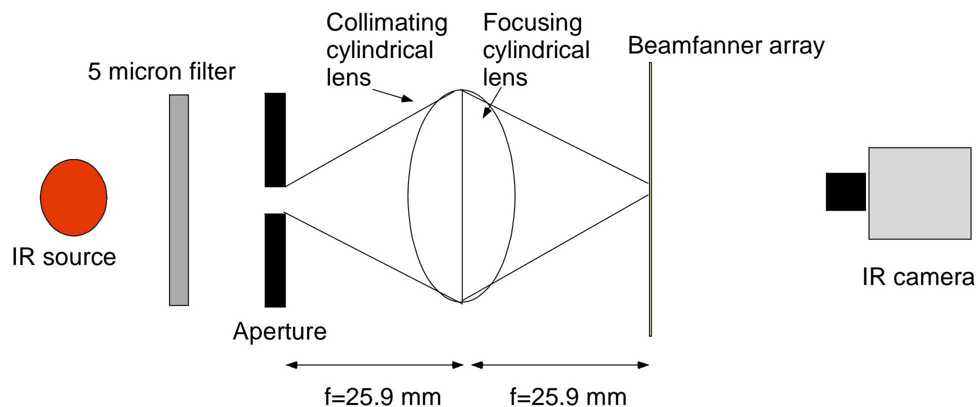

Figure 6.5 Optical testing scheme for the 1-2 beamfanners.

Unfortunately, no cases of 1-2 beamsplitting were observed. Feature rounding was originally considered as an obstacle to the beamfanners' optical performance. Sub-micron pitting, shown in Figure 6.6, was also originally thought to be a possible detractor from the performance of these beamfanners.

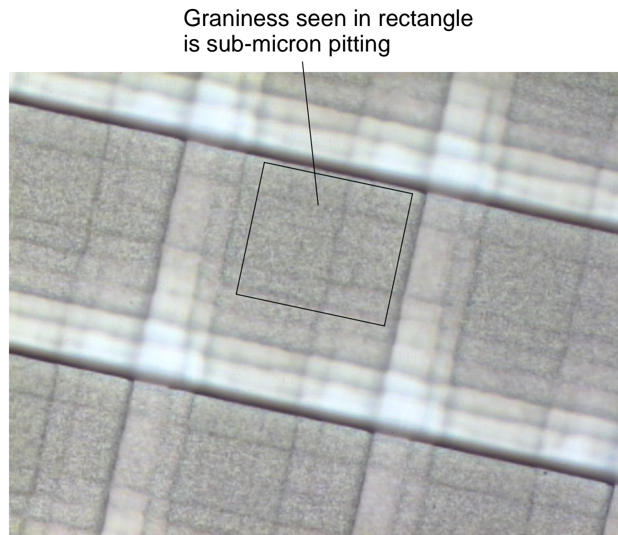

Figure 6.6 Sub-micron pitting in silicon surface of 1-4 beamfanners.

A BEM simulation of a 1-2 beamfanner with on-axis cylindrical illumination, Figure 6.6 on the next page, shows that typical 1-micron surface roughness and sidewall rounding may not degrade performance, however.

While further refinements in the testing procedure might yield cases of effective beamfanner performance, as predicted in Figure 6.7, it would have been preferable to achieve a process that yielded etch levels within 2-3% of design specifications without sub-micron pitting. Further refinements to the fabrication process could possibly be developed given more time, experimentation, and study.

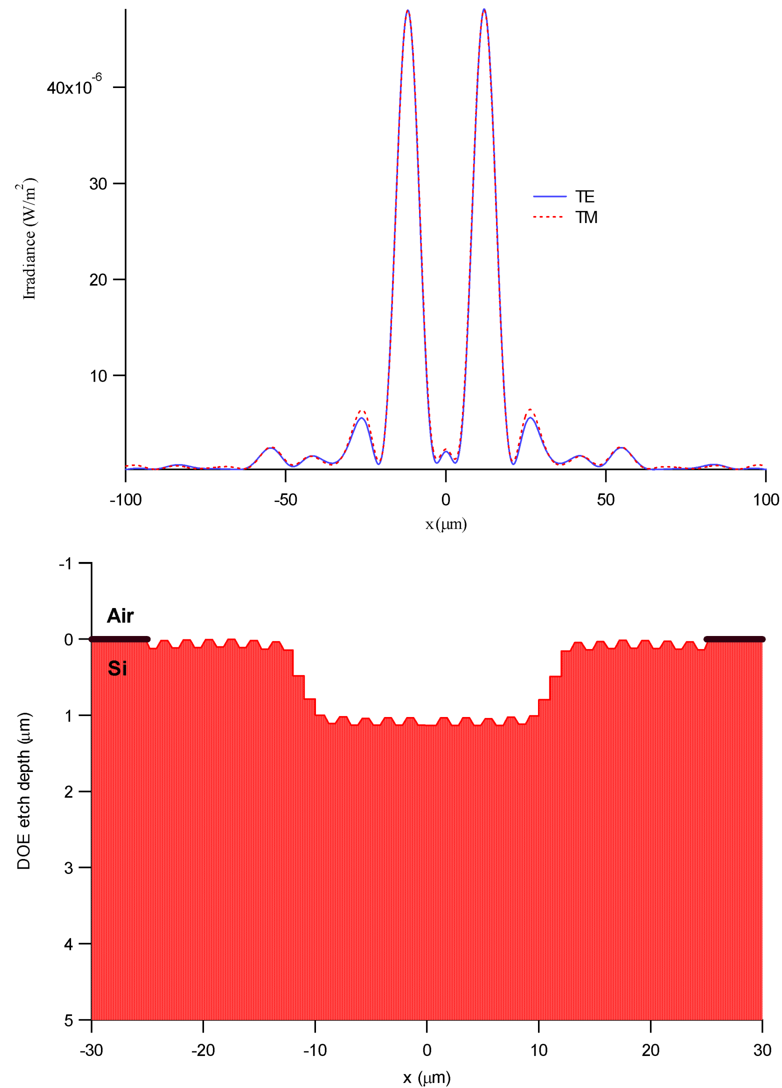

Figure 6.7 Simulated performance of on-axis 1-2 beamfanner with roughness and sidewall rounding.

6.4 Fabrication of integrated focal plane array

Two fully integrated focal plane arrays have been produced. They are well off design specifications due to a resist coating that was too thin for effective use of the etch parameters, described at the end of Chapter 4, that were used in the final 14 fabrication processes. Due to an

alignment error, the beamfanners are 593 microns misaligned in the horizontal and vertical directions with respect to the wave plate/polarizer array. This, unfortunately, renders them useless.

Chapter 7

CONCLUSION

This dissertation was started with the plan to fabricate a working 1-4 beamfanner array for the focal plane of an imaging polarimeter, but this goal proved to be too ambitious for the scope of this work. It did prove feasible to fabricate some smaller 1-2 and 1-4 beamfanner arrays within 2% of the design specifications, but the etch process was not repeatable to a degree that allowed for consistent, quality reproduction. As was discussed in Chapter 5, the between-process variance in selectivity was significantly larger than the variance in selectivity of the features within the processes. Sub-micron pitting and feature rounding further degrade the quality of the beamfanner arrays.

If the fabrication development had to be done over again, it would be worthwhile to investigate the effect of adding an inert gas, such as Argon, to the SF_6 and O_2 gas mixture used in the etch process for the UAH array. An inert gas would produce a highly directional mechanical etching effect similar to that of an ion mill. Time and material did not permit such a study, but it would be interesting to see if such an approach could reduce surface roughness and pitting in the silicon as well as help eliminate feature rounding.

It would also have been prudent to fabricate a plane wave on-axis beamfanner of the type shown in Figure 3.12, except with larger feature sizes. Plane wave illumination of the beamfanners is easier to achieve on the optical bench than the cylindrical illumination described in Chapter 6. This may have had a better chance of acting as a good test of concept for the 1-2 beamfanners.

From the standpoint of design, it would be prudent to develop a 3-dimensional code to simulate the irradiance of 1-4 beamfanners as accurately as possible. Perhaps a smooth-curved surface, rather than the small step profile typical of the beamfanners in this study, could be designed and fabricated using new techniques that form-mold the resist by melting it in a controlled fashion. If such a smooth contour could be produced to adequately approximate a DOE design, highly efficient DOE's could be fabricated.

APPENDIX A

DOE Fabrication and BEM Analysis Codes

This appendix contains Doe_fab, the code used in the design of the beamfanners, and BEM_off_axis, the code used in the performance analysis of the beamfanners.

Below is the DOE_fab code.

```
% This program prepares the data for the format for
% the 1-4 beamsplitter design
%-------------------------------------------------------------
% This program calculates the incident spherical field on a
% DOE and compensates for its tilt and curvature.  This is done
% BEFORE any beamsplitting function is performed.
%-------------------------------------------------------------
% This is for directory access
%d0='BigSpace240:Users:Mellin:DOE_Fab_stuff:Steve_ob107';
%Plevels=64;
%d0=RowPad(d0,Plevels);
%d1='JJJunk_dat';d1=RowPad(d1,Plevels);d1a='.txt';d1a=RowPad(d1a,Plevels
);
%d2=num2str((0:Plevels-1).');
%d3=find(isspace(d2)==1);
%d4=num2str(zeros(length(d3),1));
%d2(d3)=d4;
%dat_name=[d1,d2,d1a];
%------------------------------------------------------------------------
------------------
clear S S2  % clear variables that may involve other programs
% CALL the off-axis subroutine
%off_axis2;       NO LONGER NECESSARY--- INCORPORATED IN THIS PROGRAM
!!!!!!!!!!!!!!!!!!!
%------------------------------------------------------------------------
---
% This program is used to calculate the angles of tilt for DOE pixels in
% the 1-4 beamsplitter design.
%------------------------------------------------------------------------
---
lam=5.0;                                  % illuminating wavelength
n1=1.0;                                   % index in air
n2=index_dist(lam);                       % index in silicon
y1=0.527*(25.4);                    % size of aperture stop
L=50*10^(-3);                             % size of individual DOE
pixels [in mm]
y0max=(256/2)*L;%*sqrt(2);          % furthest position in image plane
y0=(L/2:L:y0max).';
y0=[flipud(y0);y0];                 % center pixel positions
last=length(y0);                    % furthest sampled position
d=1.035*(25.4);                           % distance from stop to image
plane
%------------------------------------------------------------------------
---
Theta =atan2(y0,d);                                   % Tilt angle
ang1=atan2(y0+y1/2,d);
ang2=atan2(y0-y1/2,d);
Ang_mid=(ang1+ang2)/2;
Dtheta=abs(ang1-ang2);              % Angular deviation
```

```
Alph1=atan2(n1*sin(Theta),n2-n1*cos(Theta));    % Angle in Si (from
Snell's Law)
%-----------------------------------------------------------------------
---
% For plotting, convert to degrees.
Tc=Theta*180/pi;
t1=ang1*180/pi;
t2=ang2*180/pi;
dt=Dtheta*180/pi;
a1=Alph1*180/pi;
%-----------------------------------------------------------------------
---
% Finding the variations in the REFRACTED angle
dta1=atan2(n1*sin(ang1),n2-n1*cos(ang1));
dta2=atan2(n1*sin(ang2),n2-n1*cos(ang2));
Dalph=abs(dta1-dta2);
DA=Dalph*180/pi;
%-----------------------------------------------------------------------
------------------

% Open a file containing the data from the scalar theory analysis.
%fid = fopen('doe_peaks025A.txt');
%       data_file = fscanf(fid,'%g %g',[2 inf]); % Data has two rows
now.
%       data_file = data_file';
      % Must be transposed.
%       fclose(fid); % closes file
P=50;                                                      % Number of
partitions of DOE profile
%-----------------------------------------------------------------------
-------------------------------
% Extract DOE thicknesses and corresponding locations in object plane
% CALL "Profile_Sc" subroutine to put the data in an appropriate form
for BEM .
%Xdat=data_file(:,1);                          % object positions
%Tdat=data_file(:,2);                          % thickness profile
[Xdat,Tdat]=reading_files('doe_peaks025A.txt');
L=50.0;                      % size of DOE [microns]
%[X,T]=Profile_Sc(Xdat,Tdat,L,P);   % Put the data in an appropriate
form for BEM
X=flipud(Xdat);T=flipud(Tdat);

Y=y0(1);                % location of pixel w.r.t. optical axis [mm]

%Etch_tot=9.3;    % Maximum etch depth [microns]
Etch_min=0.0;     % Minimum etch depth [microns]
phase_steps=256;%256;   % Total number of etch levels ***CHANGED AS OF
8/17/98 !!!
siz=length(y0);
%-----------------------------------------------------------------------
------------------
% Determine other parameters for DOE fabrication
nCol=P*siz;                                                      % #of
columns
nRow=P*siz;                                                      % #of
rows
```

```
Xwid=abs(X(1)-X(2))*1000;                                   % width of
pixel [nanometers]
Yhe=Xwid;                                                           %
height of pixel [nanometers]
%depth_increm=1000*(Etch_tot-Etch_min)/(phase_steps-1); % QUESTION ABOUT
DEPTH !!!!!!
prelim_file=[phase_steps;nCol;nRow;Xwid;Yhe];   % File format
%-----------------------------------------------------------------------
------------------
% For 256 levels, have 256 file levels
%d1='dat';d1=RowPad(d1,Plevels);d1a='.txt';d1a=RowPad(d1a,Plevels);
%d2=num2str((0:Plevels-1).');
%d3=find(isspace(d2)==1);
%d4=num2str(zeros(length(d3),1));
%d2(d3)=d4;
%d5=[d1,d2,d1a];


%filename='t_096.txt';
%THIS PORTION SAVES SOME OF THE INITIAL PARAMETERS----- 7/2/98
%a2='* 1-4 beamsplitter design September 14, 1998';
%fid = fopen(filename,'W');
      %fprintf(fid,'%0.0f\n',a1.');
        %fprintf(fid,'%0.0f %0.0f\n',[a1.';a2.']);
%       fprintf(fid,'%12.52s\n',a2.');
%       fclose(fid);
%---------------------
%a3='* Number of gray levels in file:';
%a4='* number of columns, number of rows.';
%a5='* width, height of each pixel. Units in nanometers.';
%a6='* raster scan of all gray levels.';
%fid = fopen(filename,'A');
      %fprintf(fid,'%0.0f\n',a1.');
        %fprintf(fid,'%0.0f %0.0f\n',[a1.';a2.']);
%       fprintf(fid,'%12.52s\n',a3.');
%       fprintf(fid,'%0.0f\n',(phase_steps).');
%       fprintf(fid,'%12.52s\n',a4.');
%       fprintf(fid,'%0.0f %0.0f\n',[6144;6144]);
%       fprintf(fid,'%12.52s\n',a5.');
%       fprintf(fid,'%0.0f %0.0f\n',[Xwid.';Yhe.']);
%       fprintf(fid,'%12.52s\n',a6.');
%     fclose(fid);
%---------------------
%for iter=1:256,              % CHANGED FROM 256!!!!!% endpoints 1:siz
-- typically siz=256
%     Y=y0(iter);

      D=1.035*25.4;           % distance from A.S. to image plane [mm]
      x=X;                    % DOE positions [microns]
      dn=n2-n1;
      Nx=length(x);%ze=zeros(Nx,1);
      %[g,F,fx,fz]=Efield2(Y,x,ze,lam);
      %phase=unwrap(angle(g));
      %d=-phase*lam/(2*pi*dn);
      %d=d-min(d);
      %-------------------------------------------------------------
      % CHECK UNITS i.e., mm and microns
```

```
      % CHECK ARBITRARY UNITS IN PHASE CALCULATIONS
      % CHECK ENDPOINTS X=+/- 25 MICRONS AND
X=FX...........................
      % careful with min and max for dz/dx calculations.
      the=mean(Dtheta);       % Avg angular spread of beam
      s=.5*L/tan(.5*the);                            %Y=0;
      yi=Y*(1+s/(D*1000))*1000;
      fx=yi-Y*1000;

      %k0=2*pi/lam;
      K=n1*s;                 % Constant phase profile
      C1=fx-x;
      %k1=n1*k0;
      %k2=n2*k0;
      % Quadratric Formula ( for dz/dx = 0 )
      A=n2^2-n1^2;
      B=2*(s*n1^2-n2*K);
      C=K^2-n1^2*s^2-n1^2*C1.^2;
      soln3=(-B-sqrt(B.^2-4.*A.*C))./(2.*A);
      % Quadratric Formula ( for z=0 and x=25 microns )
      epsilon1=10^(-9);                  % Introduce a small error
parameter
      Lmax=x(1)+epsilon1;Lmin=x(Nx)-epsilon1;               % Max and
min sampled points
      K=n1*sqrt((Lmax-fx).^2+s.^2);
      B=2*(s*n1^2-n2*K);
      C=K^2-n1^2*s^2-n1^2*C1.^2;
      soln1=(-B-sqrt(B.^2-4.*A.*C))./(2.*A);
      % Quadratric Formula ( for z=0 and x=-25 microns )
      K=n1*sqrt((Lmin-fx).^2+s.^2);
      B=2*(s*n1^2-n2*K);
      C=K^2-n1^2*s^2-n1^2*C1.^2;
      soln2=(-B-sqrt(B.^2-4.*A.*C))./(2.*A);
      % Now test which are viable solutions
      j1=soln1>=0;
      j2=soln2>=0;
      j3=soln3>=0;
      jtest=all([j1,j2,j3]);
      b1=[soln1,soln2,soln3];
      b2=b1(:,jtest==1);
      soln=b2(:,1);
      %-----------------------------------------------------------------
------
      % Now add the DOE ETCH DEPTH PROFILE to the existing profile;
      Tadj=T+soln;Tadj=Tadj-min(Tadj);

Tadj=Tadj-min(Tadj);

dont=0;
if dont==1,

      x=flipud(X);
%     S(:,iter)=flipud(Tadj);
%end
```

```
S=flatten(S);
S=S-min(S);
%S=quantize([Etot;S],phase_steps);S(1)=[];
leng_S=length(S);       %Sholud be the same as nCol and nRow
%S=S(round(leng_S/2)+1:leng_S);
S2=S;%flipud(S);
S_raster=[];
Etch_tot=2*max(S);
Time_start=cputime;
iterprint=50;
count=(1:leng_S);
element=zeros(256,1);

%*********************************************************************
****************
directory='BigSpace240:Users:Arthur:TestStuffTemp:';
filename2='TESTING123.txt';

cd(directory);


%THIS PORTION SAVES SOME OF THE INITIAL PARAMETERS----- 7/2/98
a2='* 1-4 beamsplitter design January 7, 2000';
fid = fopen(filename2,'W');
        fprintf(fid,'%12.52s\n',a2.');
       fclose(fid);
%---------------------
a3='* Number of gray levels in file:';
a4='* number of columns, number of rows.';
a5='* width, height of each pixel. Units in nanometers.';
a6='* raster scan of all gray levels.';
fid = fopen(filename2,'A');

        fprintf(fid,'%12.52s\n',a3.');
        fprintf(fid,'%0.0f\n',(phase_steps).');
        fprintf(fid,'%12.52s\n',a4.');
        fprintf(fid,'%0.0f %0.0f\n',[P*256;P*256]);
        fprintf(fid,'%12.52s\n',a5.');
        fprintf(fid,'%0.0f %0.0f\n',[Xwid.';Yhe.']);
        fprintf(fid,'%12.52s\n',a6.');
     fclose(fid);



%*********************************************************************
****************

% Raster scan
for iter2=1:P*256,%leng_S,               % endpoint leng_S  --
typically =2560
      snew=S+S2(iter2);
snew=[Etch_tot;Etch_min;snew]/Etch_tot*(phase_steps-1);
      snew=quantize(snew,phase_steps);
      snew(2)=[];snew(1)=[];

%*********************************************************************
****************
```

```
fid = fopen(filename2,'A');
        fprintf(fid,'%0.0f\n',snew);
     fclose(fid);

%*******************************************************************
****************
                  if
floor(iter2/iterprint)==iter2/iterprint|((iter2==leng_S)|(iter2==1)),

      fprintf(['\n\t',num2str(iter2),'\t\t',num2str((cputime-
Time_start)/60),' \n']);; % During final run, this should be siz * P =
12800
                  end
end % ending raster scan

Time_done=cputime-Time_start

end;  %See don't
```

This is the BEM_off_axis code.

```
%*******************************************************************
******
% BOUNDARY ELEMENT METHOD (BEM)           Latest revision:  11/18/98
% This program is used to calculate the diffracted intensity pattern
% generated by a DOE using a Boundary Element Method (BEM).  This
modified
% version restructures the DOE to suit the geometry of a 1-2
beamsplitter.
%
%     Reference:  Prather, Mirotznik, Mait. Boundary integral methods
applied
%                         to the analysis of diffractive optical elements.
%                         J. Opt. Soc. Am. A/Vol.14, No.1 (January 1997).
%*******************************************************************
******

doe_fab4A; % DO THIS FIRST !!!!!

clear FILENAMES FILES_OUT     % used later
parameters='SPLITTER_file01A.txt';        % file containing the inputs
% Opens file containing the following input parameters :
%-------------------------------------------------------------------
------
%     lam         = incident wavelength
%     n1          = index of refraction of medium 1 (air)
%     n2          = index of refraction of DOE (silicon)
%     P           = Number of partitions of DOE profile (if there is re-
sampling)
%     Q           = Number of quantized DOE levels (0 means no
quantization)
%     aper_max= max value of "sampled" aperture [microns]
```

```
%     aper_min= min value of "sampled" aperture [microns]
%     samp1       = number of samples along DOE contour per transverse
feature
%     IntPts      = # of points to take in the interpolation in finding
Y & Z matrices
%     Uamp  = magnitude of incident field
%     Uang  = ccw angle k vector makes with positive x axis [radians]
%     xUmax = largest  position of field incident on DOE [microns]
%     xUmin = smallest position of field incident on DOE [microns]
%     bess  = number of interpolation points in Hankel function
approximation
%     yzpart      = number of partitions in Y & Z matrix calc. (memory
considerations)
%     Zint  = distance to an intermediate plane [microns]
%     Zfar  = distance to the image plane [microns]
%     x0_max      = max position in image plane [microns]

%     x0_min      = min position in image plane [microns]

%     dx0         = spacing in image plane [microns]
%     filename= file containing the scalar data.
%-----------------------------------------------------------------------
------
fid = fopen(parameters,'r');
for k=1:5,fgets(fid);end;
for k=1:24,temp = fscanf(fid,'%s',1);a(k)=fscanf(fid,'%g\n',1);end;
fgets(fid);temp=fscanf(fid,'%s',1);
geomtype=fscanf(fid,'%s\n',1);            % 'opened' or 'closed'
geometric boundary contour
temp=fscanf(fid,'%s',1);
data_save=fscanf(fid,'%s\n',1);           % Save computed data? (Y/N)
temp=fscanf(fid,'%s',1);                  % type of field
transformation:
xform=fscanf(fid,'%s\n',1);               % 'angularspectrum',
'fresnel', or 'fraunhoffer'.
temp=fscanf(fid,'%s',1);                  % units of image plane
positions:
x0units=fscanf(fid,'%s\n',1);       % 'microns', 'centimeters', or
'millimeters'
temp=fscanf(fid,'%s',1);
filenumber=fscanf(fid,'%g\n',1);    % # of files
for casenumber=1:filenumber,
temp=fscanf(fid,'%s',1);
FILENAMES(casenumber,:)=fscanf(fid,'%s',1);           % file containing
scalar data
FILES_OUT(casenumber,:) =fscanf(fid,'%s\n',1);  % partial names assigned
to output
end

fclose(fid);
lam                     = a(1);
n1                      = a(2);
n2                      = a(3);
P                       = a(4);
Q                       = a(5);
aper_max          = a(6);
aper_min          = a(7);
```

```
samp1                  = a(8);
IntPts                 = a(9);
Uamp             = a(10);
Uang             = a(11);
xUmax            = a(12);
xUmin            = a(13);
gauss_order      = a(14);    % order of super_gaussian modelling the
incident field
bess             = a(15);
yzpart                 = a(16);
Zint             = a(17);    % distance to intermediate plane
Zfar             = a(18);    % distance to image plane
x0_max                 = a(19);
x0_min                 = a(20);
dx0                    = a(21);
FFTpower         = a(22);
d_AS             = a(23);    % distance from aperture stop to image
plane [mm]
AS                     = a(24);    % diameter of aperture stop [mm]

clear a fid temp

time1=cputime;          % For timing the program runs
for casenumber=1:filenumber,        % Loop for batch mode
      filename=FILENAMES(casenumber,:);
      file_out=FILES_OUT(casenumber,:);

%-----------------------------------------------------------------------
----------------
% Open a file containing scalar data.
fid = fopen(filename);
            data_file = fscanf(fid,'%g %g',[2 inf]); % Data has two
rows.
            data_file = data_file'; % Must be transposed-> 2 columns.
fclose(fid); % closes file
%-----------------------------------------------------------------------
----------------
% Extract DOE thicknesses and corresponding locations in object plane.
Xdat=data_file(:,1);    % object positions (in ascending order & equally
spaced)
Tdat=data_file(:,2);    % thickness profile


Tdat=Tdat+flipud(soln);             % THIS IS OBTAINED FROM DOE_FAB
SCRIPT FILE !!!!!!!!


% Adjust profile if there is re-sampling (also flips data for ccw BEM
format)
if P==0,P=length(Xdat);end                          % default case (no
re-sampling)
width=max(Xdat)-min(Xdat)+abs(Xdat(2)-Xdat(1));       % lateral width of
DOE [microns]
X = mean(Xdat)+(linspace(1,-1,P)*(P-1)/P).'*width/2;% positions now in
descending order
d = rect((RowPad(Xdat.',P)-ColPad(X,length(Xdat)))*P/width); %
intermediate variable
```

```
T = sum(RowPad(Tdat.',P).*d,2)./sum(d,2); clear d

Treset=find(abs(T)==min(abs(T)));Treset=T(Treset(1));
T = T-Treset;     % This is the adjusted thickness profile with re-
sampling and reset
%------------------------------------------------------------------------
----------------
% Quantize etch depth levels (note: if Q=0 -> no quantization)
T=quantize(T,Q);              % quantization is done after re-sampling
%------------------------------------------------------------------------
----------------
% Put scalar data in appropriate form for BEM
% NOTE: DOE contour follows a ccw direction (i.e. positions in
descending order)
mfs=abs(X(2)-X(1));     % This is the minimum feature size of the DOE
dx1=mfs/samp1;          % size of transverse sample
% Consider the boundary outside aperture.
xright=fliplr((max(X)+mfs:mfs: aper_max));
      tright=zeros(size(xright));
xleft =(min(X)-mfs:-mfs:aper_min);                    tleft
=zeros(size(xleft));

X1=[xright,X.',xleft];
T1=[tright,T.',tleft];
L1=length(X1);                                  % Length of appended
data file

X2=RowPad(X1,samp1+1)+ColPad(linspace(1,-1,samp1+1).',L1)*mfs/2;
T2=RowPad(T1,samp1+1);                    % Matrix containing all
samples per feature

m=abs((T1(2:L1)-T1(1:L1-1))/dx1);   % Decide how well to sample edges

Ns=(m<1)+(m>=1).*(round(m)+1);            % Ns is the number of samples
on edge

xdoe=X2(1,1);                                   % initialize with first
values
tdoe=T2(1,1);                                   % from right-most DOE
position
for ii=1:L1-1,
      if Ns(ii)==1,     % considering edge effects
            tadd=0.5*(T2(samp1+1,ii)      +T2(1,ii+1));% just take
midpoints for given edge
      else              % otherwise sample edge
            tadd=linspace(T2(samp1+1,ii),T2(1,ii+1),Ns(ii)).';
      end
      xdoe=[xdoe;X2((2:samp1),ii);(X1(ii)-mfs/2)*ones(Ns(ii),1)];
      tdoe=[tdoe;T2((2:samp1),ii);tadd];% append values for top surfaces
& edges
end
xdoe=[xdoe;X2((2:samp1+1),L1)];     % append final values after last
edge
tdoe=[tdoe;T2((2:samp1+1),L1)];                 % FINAL DOE PROFILE

clear X1 T1 X2 T2 xright tright xleft tleft % save computer memory
Nsize=length(xdoe);                 % number of samples on DOE surface
```

```
%-----------------------------------------------------------------------
----------------
% Find the shifted values for the DOE positions and thickness profile.
% NOTE: it is assumed at edges that thickness does not change (unlike
for "closed" contours).
x_plus=[xdoe(2:Nsize);xdoe(Nsize)-dx1];
x_minus=[xdoe(1)+dx1;xdoe(1:Nsize-1)];
t_plus=[tdoe(2:Nsize);tdoe(Nsize)];
t_minus=[tdoe(1);tdoe(1:Nsize-1)];
% Find the differential line segments for contour integration
diffLP=sqrt((x_plus-xdoe).^2+(t_plus-tdoe).^2);
diffLM=sqrt((x_minus-xdoe).^2+(t_minus-tdoe).^2);

% Find the exterior angles of a DOE profile for BEM.
% NOTE: normal vectors point outward from region 2.

a1=atan2(t_minus-tdoe,x_minus-xdoe);      % ccw angle w.r.t positive x
axis
a2=atan2(t_plus-tdoe,x_plus-xdoe);

theta=mod(a1-a2,2*pi);                          % exterior angles
theta=theta.*(theta<1.99*pi);             % checks for round-off error
normal_ang=mod(a2+theta/2,2*pi);          % This is the angle of the
normal vector
ang_plus=mod(a2+pi/2,2*pi);                     % gives the Nth normal
angle for THE EDGES
ang_minus=mod(a1-pi/2,2*pi);                    % gives the (N-1)th
normal angle for THE EDGES
%-----------------------------------------------------------------------
----------------
% Display run statistics to Command window.
fprintf(['---------------------------------------------------------------
------------------------\n']);
fprintf(['\n\nRunning BEM for file:\t',filename,'\t\t']);
fprintf([datestr(now,8),'\t',datestr(now,1),'\t',datestr(now,16),'\n\n\n
']);
fprintf(['Number of boundary sample points:\t\t',num2str(Nsize),'\n']);
fprintf(['DOE minimum feature size (microns):\t\t',num2str(mfs),'\n']);
fprintf(['Transverse spacing increment(microns):\t',num2str(dx1),'\n']);
fprintf(['Quantization of thickness levels: \t\t',num2str(Q),' \n']);
fprintf(['\nTiming program blocks (units in seconds):\n']);
%***********************************************************************
****************
% FIND Y AND Z MATRICES THAT DESCRIBE BOUNDARY POINT COUPLING

                  tz2=cputime;
Z2 =diag(1-
theta/(2*pi))+YZcoupling01A(xdoe,tdoe,lam/n2,'z',IntPts,bess,yzpart);
                  fprintf(['\n\nz2 time:\t\t\t',num2str(cputime-
tz2),'\n']);

                  tz1=cputime;
Z1 =diag(theta/(2*pi))-
YZcoupling01A(xdoe,tdoe,lam/n1,'z',IntPts,bess,yzpart);
                  fprintf(['z1 time:\t\t\t',num2str(cputime-tz1),'\n'])

                  ty2=cputime;
```

```
Y2 = YZcoupling01A(xdoe,tdoe,lam/n2,'y',IntPts,bess,yzpart);
                  fprintf(['y2 time:\t\t\t',num2str(cputime-ty2),'\n'])

                  ty1=cputime;
Y1 = YZcoupling01A(xdoe,tdoe,lam/n1,'y',IntPts,bess,yzpart);
                  fprintf(['y1 time:\t\t\t',num2str(cputime-ty1),'\n']);
%*************************************************************************
****************
% Introduce incident fields -> uses exp(-jkz) notation
%k1=2*pi*n1/lam;
%Uinc=Uamp*super_gaussian(xdoe,xUmax-xUmin,gauss_order).*exp(-
j*k1*(sin(Uang)*tdoe+cos(Uang)*xdoe));
%Un=-j*k1.*Uinc.*(sin(Uang)*sin(normal_ang)+cos(Uang)*cos(normal_ang));
                                                % Normal derivative of
incident field   PLANE WAVE STUFF !!!!
%-------------------------------------------------------------------------
----------------
% CONSIDERING GEOMETRY OF INFRARED CAMERA SYSTEM
!!!!!!!!!!!!!!!!!!!!!!!!!!!!!!!!!
a01=((Y-width/2/1000)+(AS/2))/d_AS;            b01=((Y+width/2/1000)-
(AS/2))/d_AS;
ft=width./(a01-b01);                                 fx=b01*ft+width/2;
r01=sqrt((ft-tdoe).^2+(fx-xdoe).^2);                 clear a01 b01 fx
ft
Uinc=exp(j*(2*pi*n1/lam)*r01)./r01;                  clear r01  %
without finite aperture
% CALCULATE INCIDENT FIELD !!!! (note that it's a sperical wave)
Uinc=Uinc.*rect(xdoe/width);  % Impose finite aperture
%Uinc=rect(x_doe/width).*exp(-j*2*pi*n1*t_doe/lam*cos(a1)).*exp(-
j*2*pi*n1*x_doe/lam*sin(a1)); FOR PLANE WAVES !
Ux=0;Uz=0;
Un=cos(normal_ang).*Ux+sin(normal_ang).*Uz;     % THIS IS EFFECTIVELY
SET TO ZERO FOR OPEN CONTOURS !!!

%-------------------------------------------------------------------------
----------------
% Find scattered fields and normal derivatives using LU decomposition

                              ts=cputime; % TE case
[Esc_te,Qsc_te]=Scattered_field01A(Z1,Y1,Z2,Y2,geomtype,Uinc,Un);
                              fprintf(['TE
inversion:\t\t',num2str(cputime-ts),'\n']);

                              ts=cputime; % TM case
[Esc_tm,Qsc_tm]=Scattered_field01A(Z1,Y1*n1^2,Z2,Y2*n2^2,geomtype,Uinc,U
n);
                              fprintf(['TM
inversion:\t\t',num2str(cputime-ts),'\n'])

clear Y1 Y2 Z1 Z2       % save computer memory
%-------------------------------------------------------------------------
----------------
% Find total field in the image plane

x0_bem = (x0_min:dx0:x0_max).';           % positions in image plane
[microns]
```

```
                                    tfin=cputime;     % TE case
E=Total_Field01A(xdoe,tdoe,lam/n2,Zint,x0_bem,Esc_te,Qsc_te,bess,yzpart)
;
                                    fprintf(['TE field
calc:\t\t',num2str(cputime-tfin),'\n']);

                                    tfin=cputime;     % TM case
H=Total_Field01A(xdoe,tdoe,lam/n2,Zint,x0_bem,Esc_tm,n2^2*Qsc_tm,bess,yz
part);
                                    fprintf(['TM field
calc:\t\t',num2str(cputime-tfin),'\n']);
%-----------------------------------------------------------------------
----------------
% Propagate to image plane via scalar field transformation
Zint=max([Zint;tdoe]);  % Safeguard for field evaluation in an
intermediate plane
if (Zint<Zfar)&(Zint>max(tdoe)),                    tfin=cputime;


      lx0=length(x0_bem);
      DFTsize=power(2,FFTpower);
      x0_bem=[(0:DFTsize/2-1),(-DFTsize/2:-1)].'*dx0+mean(x0_bem);
      % object plane positions [microns]

      E=[E;zeros(DFTsize-lx0,1)];
      E=shiftud(E,-floor(lx0/2),1);

      H=[H;zeros(DFTsize-lx0,1)];
      H=shiftud(H,-floor(lx0/2),1);

      [E,x0]=scalar_analysis1(E,x0_bem,Zfar-Zint,lam/n2,xform);
      [H,x0]=scalar_analysis1(H,x0_bem,Zfar-Zint,lam/n2,xform);

      x0_bem=fftshift(x0);
      E=fftshift(E);
      H=fftshift(H);
                              fprintf([xform,'
xform:\t\t',num2str(cputime-tfin),'\n']);
end
%-----------------------------------------------------------------------
----------------
% Proper scaling of H field
H=n1/n2*H;
TEI=abs(E).^2;
TMI=abs(H).^2;
x0_bem1=pick(x0_bem,x0_bem,-100,100);
TEI1=pick(TEI,x0_bem,-100,100);
TMI1=pick(TMI,x0_bem,-100,100);
%-----------------------------------------------------------------------
----------------
% Units of x0 positions (µm is the default unit)
if lower(x0units(1:5))=='milli',x0_bem=x0_bem/1000;end;
if lower(x0units(1:5))=='centi',x0_bem=x0_bem/10000;end;
%-----------------------------------------------------------------------
----------------
X_temp=['XBEM',file_out];                  % assign variable names to
output
```

```
E_temp=['EBEM',file_out];
H_temp=['HBEM',file_out];
assignin('base',X_temp,x0_bem);           % x0 positions
assignin('base',E_temp,abs(E));           % E field values
assignin('base',H_temp,abs(H));           % H field values

            if upper(data_save(1))=='Y',  % save data? NOT PROPERLY
WORKING YET !!!!
                        fid = fopen([file_out,'.txt'],'w');
                        fprintf(fid,'%12.8f
%12.8f\n',[eval(X_temp).';eval(E_temp).';eval(H_temp).']);
                        fclose(fid);
            end
%------------------------------------------------------------------------
----------------
end   % Closing batch mode

cd('BigSpace240:Users:Arthur:No Resampling')
fid=fopen('Esp.txt','w');
fprintf(fid,'%12.8f\n',TEI1);
fclose(fid);
fid=fopen('Hsp.txt','w');
fprintf(fid,'%12.8f\n',TMI1);
fclose(fid);
%fid=fopen('Xbm.txt','w');
%fprintf(fid,'%12.8f\n',x0_bem1);
%fclose(fid);
fid=fopen('Xdoesp.txt','w');
fprintf(fid,'%12.8f\n',xdoe);
fclose(fid);
fid=fopen('Tdoesp.txt','w');
fprintf(fid,'%12.8f\n',tdoe);
fclose(fid);
clear FILENAMES FILES_OUT
time2=cputime-time1;    % Time it takes to run program
fprintf(['\nrun time = ',num2str(floor(time2/60)),' min.
',num2str(rem(time2,60)),' seconds\n']);
fprintf(['----------------------------------------------------------------
------------------------\n']);
```

APPENDIX B

Statistical Analysis Code used in Chapter 5

Below is the code, Selectivitya.

```
% Designed to handle the statistical anlysis of grayscale photolith/etch
data
% Note, seperate etches are considered blocks, so block and treatment
must be interchanged
%   for blocked studies.

% Raw Photlith data
PL11=[.64,.66,.60,.65,.64,.65,.69,.64,.60,.69,.63,.67,.65,.66];
PL12=[.88,.90,.87,.90,.87,.91,.93,.89,.84,.94,.91,.95,.90,.90];
PL21=[.62,.66,.64,.65,.68,.66,.67,.64,.61,.65,.65,.67,.67,.65];
PL22=[.89,.88,.93,.91,.89,.92,.89,.88,.85,.93,.88,.95,.91,.91];
PL31=[.63,.64,.62,.60,.62,.63,.61,.63,.61,.62,.61,.66,.65,.63];
PL32=[.89,.88,.88,.86,.89,.90,.89,.91,.87,.91,.87,.95,.91,.89];
PL41=[.63,.64,.65,.64,.63,.64,.66,.65,.62,.62,.64,.66,.66,.64];
PL42=[.88,.88,.86,.88,.90,.90,.89,.88,.86,.89,.89,.94,.89,.87];
PL51=[1.09,1.09,1.06,1.12,1.14,1.08,1.15,1.11,1.06,1.07,1.10,1.16,1.11,1
.05];
PL52=[1.55,1.58,1.55,1.63,1.63,1.58,1.63,1.62,1.51,1.57,1.57,1.67,1.62,1
.55];
PL53=[1.80,1.84,1.81,1.90,1.86,1.83,1.88,1.85,1.78,1.78,1.80,1.96,1.89,1
.84];
PL54=[1.55,1.58,1.53,1.65,1.64,1.57,1.64,1.60,1.52,1.60,1.60,1.73,1.67,1
.60];
PL61=[1.00,1.03,1.02,1.09,1.05,1.02,1.03,1.05,1.01,1.01,1.00,1.06,1.04,1
.01];
PL62=[1.66,1.76,1.75,1.78,1.75,1.76,1.77,1.76,1.68,1.70,1.72,1.83,1.76,1
.70];
PL63=[1.77,1.82,1.80,1.86,1.83,1.82,1.83,1.82,1.73,1.76,1.79,1.89,1.84,1
.75];
PL64=[1.55,1.61,1.59,1.65,1.62,1.60,1.60,1.61,1.55,1.60,1.58,1.67,1.63,1
.57];
PL71=[.99,1.04,1.07,1.07,1.06,1.03,1.08,1.09,.96,.96,.96,1.04,1.03,.98];
PL72=[1.73,1.76,1.79,1.81,1.79,1.78,1.80,1.80,1.71,1.70,1.74,1.84,1.79,1
.72,];
PL73=[1.83,1.87,1.86,1.90,1.89,1.91,1.91,1.90,1.81,1.81,1.81,1.96,1.90,1
.79,];
PL74=[1.80,1.78,1.77,1.85,1.80,1.83,1.84,1.85,1.73,1.76,1.72,1.89,1.82,1
.71,];
PL81=[.95,1.03,.99,1.01,.99,1.00,1.04,1.03,.99,.96,1.02,1.04,1.06,.99];
PL82=[1.70,1.78,1.76,1.79,1.76,1.78,1.82,1.81,1.72,1.71,1.72,1.79,1.81,1
.72];
PL83=[1.79,1.88,1.83,1.87,1.86,1.86,1.88,1.93,1.81,1.80,1.80,1.92,1.88,1
.77];
PL84=[1.68,1.84,1.74,1.79,1.76,1.81,1.81,1.86,1.73,1.76,1.71,1.84,1.82,1
.73];
PL91=[1.40,1.48,1.40,1.50,1.46,1.44,1.49,1.52,1.46,1.43,1.46,1.49,1.47,1
.40];
PL92=[2.19,2.24,2.23,2.28,2.26,2.24,2.28,2.27,2.16,2.15,2.20,2.32,2.26,2
.11];
PL93=[2.62,2.70,2.65,2.74,2.68,2.68,2.71,2.72,2.61,2.60,2.60,2.78,2.69,2
.51];
PL94=[3.12,3.19,3.13,3.25,3.19,3.18,3.21,3.23,3.06,3.06,3.09,3.32,3.20,3
.00];
```

```
PL101=[1.28,1.35,1.34,1.31,1.33,1.33,1.32,1.30,1.30,1.25,1.27,1.32,1.32,
1.21];
PL102=[2.38,2.46,2.44,2.48,2.49,2.43,2.48,2.47,2.37,2.33,2.37,2.50,2.46,
2.27];
PL103=[2.90,2.99,2.96,3.00,3.00,2.96,3.01,2.98,2.88,2.79,2.89,3.04,2.99,
2.74];
PL104=[3.13,3.21,3.16,3.24,3.21,3.20,3.23,3.20,3.07,3.02,3.09,3.24,3.21,
2.94];
PL111=[1.32,1.34,1.34,1.29,1.26,1.35,1.31,1.27,1.21,1.26,1.24,1.37,1.32,
1.17];
PL112=[2.38,2.43,2.44,2.42,2.39,2.45,2.43,2.40,2.29,2.30,2.32,2.51,2.46,
2.21];
PL113=[2.88,2.95,2.95,2.97,2.92,2.97,2.97,2.94,2.81,2.81,2.87,3.08,2.96,
2.71];
PL114=[3.16,3.22,3.21,3.19,3.14,3.24,3.20,3.15,3.01,3.04,3.08,3.32,3.20,
2.94];
PL121=[1.21,1.30,1.29,1.27,1.25,1.25,1.26,1.25,1.20,1.19,1.22,1.28,1.27,
1.24];
PL122=[2.35,2.42,2.43,2.46,2.41,2.41,2.46,2.45,2.29,2.29,2.34,2.46,2.44,
2.26];
PL123=[2.88,2.96,2.94,3.00,2.96,2.97,2.99,2.96,2.85,2.76,2.86,3.02,2.97,
2.77];
PL124=[3.16,3.21,3.21,3.29,3.24,3.24,3.28,3.26,3.07,3.07,3.13,3.32,3.25,
3.05];

%Raw Etch data

E11=[.75,.79,.73,.75,.77,.81,.83,.82,.74,.64,.65,.76,.69,.69];
E12=[1.03,1.11,.98,1.04,1.05,1.13,1.12,1.15,1.00,.96,.93,1.10,.98,.96];
E21=[.65,.80,.70,.73,.74,.85,.78,.86,.78,.68,.66,.75,.66,.67];
E22=[.92,1.10,.96,1.03,1.05,1.16,1.12,1.16,1.03,.98,.93,1.07,.95,.98];
E31=[.67,.82,.71,.76,.75,.82,.80,.84,.73,.61,.63,.73,.61,.66];
E32=[1.00,1.15,.96,1.02,1.05,1.19,1.10,1.18,1.01,.92,.96,1.06,.92,.97];
E41=[.69,.81,.69,.71,.76,.83,.79,.86,.75,.64,.64,.74,.66,.69];
E42=[.99,1.11,.95,1.04,1.05,1.14,1.13,1.17,1.01,1.00,.95,1.03,.96,.97];
E51=[1.18,1.38,1.26,1.33,1.32,1.42,1.38,1.43,1.31,1.15,1.17,1.30,1.15,1.
19];
E52=[1.74,1.96,1.76,1.83,1.89,2.05,1.98,2.03,1.86,1.72,1.73,1.93,1.77,1.
69];
E53=[2.03,2.31,2.04,2.17,2.23,2.36,2.22,2.32,2.13,2.04,2.02,2.27,2.11,1.
93];
E54=[1.75,1.97,1.77,1.93,1.90,2.08,1.96,2.05,1.89,1.76,1.81,2.01,1.83,1.
77];
E61=[1.09,1.30,1.06,1.21,1.16,1.24,1.28,1.32,1.16,1.10,1.07,1.17,1.10,1.
03];
E62=[1.92,2.18,1.91,2.02,2.06,2.21,2.16,2.20,1.99,1.86,1.86,2.09,1.94,1.
78];
E63=[2.02,2.26,2.01,2.10,2.15,2.31,2.23,2.28,2.13,1.96,1.94,2.23,2.07,1.
85];
E64=[1.80,1.99,1.78,1.87,1.95,2.09,1.96,2.02,1.87,1.74,1.71,1.97,1.84,1.
65];
E71=[1.09,1.28,1.11,1.15,1.16,1.31,1.26,1.33,1.16,1.05,1.02,1.15,1.11,1.
06];
E72=[1.94,2.18,1.96,2.07,2.02,2.24,2.18,2.22,2.01,1.91,1.87,2.13,2.01,1.
82];
E73=[2.03,2.32,2.06,2.15,2.12,2.35,2.29,2.35,2.16,2.04,1.99,2.27,2.17,1.
93];
```

```
E74=[1.96,2.24,2.01,2.07,2.08,2.31,2.19,2.23,2.10,1.99,1.92,2.20,2.10,1.
84];
E81=[1.12,1.33,1.09,1.18,1.19,1.30,1.21,1.30,1.15,1.03,1.11,1.14,1.06,.9
6];
E82=[1.96,2.25,1.98,2.09,2.12,2.27,2.13,2.24,2.03,1.91,1.93,2.13,2.05,1.
75];
E83=[2.10,2.32,2.07,2.22,2.23,2.41,2.24,2.33,2.12,2.01,2.03,2.24,2.14,1.
85];
E84=[2.01,2.26,1.96,2.13,2.15,2.33,2.15,2.24,2.03,1.97,1.98,2.15,2.08,1.
76];
E91=[1.63,1.87,1.64,1.67,1.72,1.89,1.85,1.87,1.67,1.57,1.56,1.69,1.61,1.
41];
E92=[2.51,2.84,2.54,2.64,2.68,2.85,2.78,2.85,2.59,2.47,2.42,2.71,2.55,2.
17];
E93=[2.99,3.39,3.04,3.21,3.20,3.38,3.33,3.39,3.07,2.96,2.91,3.28,3.08,2.
62];
E94=[3.53,4.00,3.63,3.78,3.83,4.02,3.94,3.97,3.65,3.53,3.45,3.91,3.70,3.
09];
E101=[1.45,1.60,1.42,1.51,1.51,1.67,1.55,1.65,1.50,1.29,1.35,1.47,1.37,1
.24];
E102=[2.69,3.05,2.74,2.88,2.87,3.11,2.96,3.06,2.81,2.58,2.64,2.97,2.73,2
.39];
E103=[3.28,3.69,3.35,3.52,3.53,3.75,3.62,3.71,3.40,3.18,3.19,3.63,3.34,2
.85];
E104=[3.56,3.97,3.65,3.77,3.76,4.03,3.87,3.97,3.63,3.43,3.42,3.93,3.70,3
.05];
E111=[1.46,1.64,1.46,1.53,1.53,1.68,1.71,1.66,1.54,1.38,1.37,1.52,1.41,1
.29];
E112=[2.70,2.99,2.73,2.84,2.86,3.06,3.04,3.03,2.80,2.58,2.61,2.96,2.73,2
.36];
E113=[3.32,3.68,3.36,3.49,3.53,3.72,3.73,3.70,3.41,3.19,3.22,3.65,3.40,2
.88];
E114=[3.59,3.96,3.61,3.74,3.77,3.99,3.97,3.99,3.68,3.48,3.43,3.93,3.68,3
.05];
E121=[1.38,1.57,1.43,1.49,1.52,1.60,1.59,1.62,1.50,1.35,1.33,1.49,1.37,1
.26];
E122=[2.65,3.00,2.74,2.83,2.85,3.05,2.97,3.03,2.81,2.56,2.61,2.97,2.75,2
.40];
E123=[3.29,3.69,3.40,3.51,3.54,3.74,3.62,3.72,3.42,3.17,3.20,3.65,3.40,2
.90];
E124=[3.54,4.01,3.70,3.85,3.82,4.07,4.00,4.03,3.69,3.46,3.48,4.00,3.73,3
.17];

% Selectivities

S11=seldiv(E11,PL11);
S12=seldiv(E12,PL12);
S21=seldiv(E21,PL21);
S22=seldiv(E22,PL22);
S31=seldiv(E31,PL31);
S32=seldiv(E32,PL32);
S41=seldiv(E41,PL41);
S42=seldiv(E42,PL42);
S51=seldiv(E51,PL51);
S52=seldiv(E52,PL52);
S53=seldiv(E53,PL53);
S54=seldiv(E54,PL54);
```

```
S61=seldiv(E61,PL61);
S62=seldiv(E62,PL62);
S63=seldiv(E63,PL63);
S64=seldiv(E64,PL64);
S71=seldiv(E71,PL71);
S72=seldiv(E72,PL72);
S73=seldiv(E73,PL73);
S74=seldiv(E74,PL74);
S81=seldiv(E81,PL81);
S82=seldiv(E82,PL82);
S83=seldiv(E83,PL83);
S84=seldiv(E84,PL84);
S91=seldiv(E91,PL91);
S92=seldiv(E92,PL92);
S93=seldiv(E93,PL93);
S94=seldiv(E94,PL94);
S101=seldiv(E101,PL101);
S102=seldiv(E102,PL102);
S103=seldiv(E103,PL103);
S104=seldiv(E104,PL104);
S111=seldiv(E111,PL111);
S112=seldiv(E112,PL112);
S113=seldiv(E113,PL113);
S114=seldiv(E114,PL114);
S121=seldiv(E121,PL121);
S122=seldiv(E122,PL122);
S123=seldiv(E123,PL123);
S124=seldiv(E124,PL124);




% Observation Matrix for Selectivities

OBSMAT=[S11;S12;S21;S22;S31;S32;S41;S42;S51;S52;S53;S54;S61;S62;S63;S64;
S71;S72;S73;S74;S81;S82;S83;S84;S91;S92;
   S93;S94;S101;S102;S103;S104;S111;S112;S113;S114;S121;S122;S123;S124];

% Observation Matrix for Photolith

OBSMATP=[PL11;PL12;PL21;PL22;PL31;PL32;PL41;PL42;PL51;PL52;PL53;PL54;PL6
1;PL62;PL63;
   PL64;PL71;PL72;PL73;PL74;PL81;PL82;PL83;PL84;PL91;PL92;

PL93;PL94;PL101;PL102;PL103;PL104;PL111;PL112;PL113;PL114;PL121;PL122;PL
123;PL124];

% Observation Matrix for Etch

OBSMATE=[E11;E12;E21;E22;E31;E32;E41;E42;E51;E52;E53;E54;E61;E62;E63;E64
;E71;E72;E73;E74;E81;E82;E83;E84;E91;E92;
   E93;E94;E101;E102;E103;E104;E111;E112;E113;E114;E121;E122;E123;E124];

% Find Variance and Standard Deviation over the 14 processes for each
feature
```

```
AVSEL=(sum(sum(OBSMAT)))/560;
AVSELP=(sum(sum(OBSMATP)))/560;
AVSELE=(sum(sum(OBSMATE)))/560;

% Grand Average matrices for selectivities, photoliths, etches

for i=1:40
   for j=1:14
      GRANDAV(i,j)=AVSEL;
      GRANDAVP(i,j)=AVSELP;
      GRANDAVE(i,j)=AVSELE;
      j=j+1;
   end;
   i=i+1;
   end;




%Treatment mean vectors

TREMEAN=(sum(OBSMAT))/40;
TREMEANP=(sum(OBSMATP))/40;
TREMEANE=(sum(OBSMATE))/40;

%Treatment mean matrices

TREMEANMAT=[TREMEAN;TREMEAN;TREMEAN;TREMEAN;TREMEAN;TREMEAN;TREMEAN;TREM
EAN;TREMEAN;TREMEAN;

TREMEAN;TREMEAN;TREMEAN;TREMEAN;TREMEAN;TREMEAN;TREMEAN;TREMEAN;TREMEAN;
TREMEAN;

TREMEAN;TREMEAN;TREMEAN;TREMEAN;TREMEAN;TREMEAN;TREMEAN;TREMEAN;TREMEAN;
TREMEAN;

TREMEAN;TREMEAN;TREMEAN;TREMEAN;TREMEAN;TREMEAN;TREMEAN;TREMEAN;TREMEAN;
TREMEAN];

TREMEANMATP=[TREMEANP;TREMEANP;TREMEANP;TREMEANP;TREMEANP;TREMEANP;TREME
ANP;TREMEANP;TREMEANP;TREMEANP;

TREMEANP;TREMEANP;TREMEANP;TREMEANP;TREMEANP;TREMEANP;TREMEANP;TREMEANP;
TREMEANP;TREMEANP;

TREMEANP;TREMEANP;TREMEANP;TREMEANP;TREMEANP;TREMEANP;TREMEANP;TREMEANP;
TREMEANP;TREMEANP;

TREMEANP;TREMEANP;TREMEANP;TREMEANP;TREMEANP;TREMEANP;TREMEANP;TREMEANP;
TREMEANP;TREMEANP];

TREMEANMATE=[TREMEANE;TREMEANE;TREMEANE;TREMEANE;TREMEANE;TREMEANE;TREME
ANE;TREMEANE;TREMEANE;TREMEANE;
```

```
TREMEANE;TREMEANE;TREMEANE;TREMEANE;TREMEANE;TREMEANE;TREMEANE;TREMEANE;
TREMEANE;TREMEANE;

TREMEANE;TREMEANE;TREMEANE;TREMEANE;TREMEANE;TREMEANE;TREMEANE;TREMEANE;
TREMEANE;TREMEANE;

TREMEANE;TREMEANE;TREMEANE;TREMEANE;TREMEANE;TREMEANE;TREMEANE;TREMEANE;
TREMEANE;TREMEANE];



%Block mean vectors

BLOCKMEAN=(sum(OBSMAT'))/14;
BLOCKMEANP=(sum(OBSMATP'))/14;
BLOCKMEANE=(sum(OBSMATE'))/14;

%Block mean matrix

BLOCKMEANMATA=[BLOCKMEAN;BLOCKMEAN;BLOCKMEAN;BLOCKMEAN;BLOCKMEAN;BLOCKME
AN;BLOCKMEAN;

BLOCKMEAN;BLOCKMEAN;BLOCKMEAN;BLOCKMEAN;BLOCKMEAN;BLOCKMEAN;BLOCKMEAN];

BLOCKMEANMATAP=[BLOCKMEANP;BLOCKMEANP;BLOCKMEANP;BLOCKMEANP;BLOCKMEANP;B
LOCKMEANP;BLOCKMEANP;

BLOCKMEANP;BLOCKMEANP;BLOCKMEANP;BLOCKMEANP;BLOCKMEANP;BLOCKMEANP;BLOCKM
EANP];

BLOCKMEANMATAE=[BLOCKMEANE;BLOCKMEANE;BLOCKMEANE;BLOCKMEANE;BLOCKMEANE;B
LOCKMEANE;BLOCKMEANE;

BLOCKMEANE;BLOCKMEANE;BLOCKMEANE;BLOCKMEANE;BLOCKMEANE;BLOCKMEANE;BLOCKM
EANE];


BLOCKMEANMAT=BLOCKMEANMATA';
BLOCKMEANMATP=BLOCKMEANMATAP';
BLOCKMEANMATE=BLOCKMEANMATAE';

%Decomposition Matrices, and std over 14 runs for each of 40 features

B=BLOCKMEANMAT-GRANDAV;
T=TREMEANMAT-GRANDAV;
R=OBSMAT-BLOCKMEANMAT-TREMEANMAT+GRANDAV;
BLOCKEXVAL=BLOCKMEANMAT+TREMEANMAT-GRANDAV;
T1=OBSMAT-TREMEANMAT;
T2=OBSMAT-BLOCKMEANMAT;
for i=1:40
   for j=1:14
      OBSV(i,j)=T2(i,j)^2;
      j=j+1;
   end;
   i=i+1;
end;
```

```
selvar=(sum(OBSV')/13)';
for i=1:40
   stdsel(i,1)=sqrt(selvar(i,1));
   i=i+1;
   end;


BP=BLOCKMEANMATP-GRANDAVP;
TP=TREMEANMATP-GRANDAVP;
RP=OBSMATP-BLOCKMEANMATP-TREMEANMATP+GRANDAVP;
T2P=OBSMATP-BLOCKMEANMATP;
for i=1:40
   for j=1:14
      OBSVP(i,j)=T2P(i,j)^2;
      j=j+1;
   end;
   i=i+1;
end;
pvar=(sum(OBSVP')/13)';
for i=1:40
   stdp(i,1)=sqrt(pvar(i,1));
   i=i+1;
   end;


BE=BLOCKMEANMATE-GRANDAVE;
TE=TREMEANMATE-GRANDAVE;
RE=OBSMATE-BLOCKMEANMATE-TREMEANMATE+GRANDAVE;
T2E=OBSMATE-BLOCKMEANMATE;
for i=1:40
   for j=1:14
      OBSVE(i,j)=T2E(i,j)^2;
      j=j+1;
   end;
   i=i+1;
end;
evar=(sum(OBSVE')/13)';
for i=1:40
   stde(i,1)=sqrt(evar(i,1));
   i=i+1;
   end;



% Construct Position on Substrate Vectors

   for i=1:40
      for j=1:14
         POSVEC(i,j)=i;
      end;
   end;

   for i=1:2
      for j=1:14
         P1L(i,j)=1;
      end;
   end;
```

```
for i=1:2
   for j=1:14
      P2L(i,j)=2;
   end;
end;

for i=1:2
   for j=1:14
      P3L(i,j)=3;
   end;
end;

for i=1:2
   for j=1:14
      P4L(i,j)=4;
   end;
end;

for i=1:4
   for j=1:14
      P5L(i,j)=5;
   end;
end;

for i=1:4
   for j=1:14
      P6L(i,j)=6;
   end;
end;

for i=1:4
   for j=1:14
      P7L(i,j)=7;
   end;
end;

for i=1:4
   for j=1:14
      P8L(i,j)=8;
   end;
end;

for i=1:4
   for j=1:14
      P9L(i,j)=9;
   end;
end;

for i=1:4
   for j=1:14
      P10L(i,j)=10;
   end;
end;

for i=1:4
   for j=1:14
```

```
         P11L(i,j)=11;
      end;
   end;

   for i=1:4
      for j=1:14
         P12L(i,j)=12;
      end;
   end;

   POSVECL=[P1L;P2L;P3L;P4L;P5L;P6L;P7L;P8L;P9L;P10L;P11L;P12L];

   for i=1:2
      for j=1:14
         P1S(i,j)=i;
      end;
   end;

   for i=1:4
      for j=1:14
         P2S(i,j)=i;
      end;
   end;

   POSVECS=[P1S;P1S;P1S;P1S;P2S;P2S;P2S;P2S;P2S;P2S;P2S;P2S];

   for i=1:40
      for j=1:14
         TIMEVEC(i,j)=j;
      end;
      end;
```

```
% Construct vectors of squared values and residuals

for i=1:40
   for j=1:14
      squOBSMAT(1,14*i-(14-j))=OBSMAT(i,j)^2;
      squOBSMATP(1,14*i-(14-j))=OBSMATP(i,j)^2;
      squOBSMATE(1,14*i-(14-j))=OBSMATE(i,j)^2;
      squGRANDAV(1,14*i-(14-j))=GRANDAV(i,j)^2;
      squGRANDAVP(1,14*i-(14-j))=GRANDAVP(i,j)^2;
      squGRANDAVE(1,14*i-(14-j))=GRANDAVE(i,j)^2;
      squTREMEANMAT(1,14*i-(14-j))=TREMEANMAT(i,j)^2;
      squTREMEANMATP(1,14*i-(14-j))=TREMEANMATP(i,j)^2;
      squTREMEANMATE(1,14*i-(14-j))=TREMEANMATE(i,j)^2;
      squBLOCKMEANMAT(1,14*i-(14-j))=BLOCKMEANMAT(i,j)^2;
```

```
      squBLOCKMEANMATP(1,14*i-(14-j))=BLOCKMEANMATP(i,j)^2;
      squBLOCKMEANMATE(1,14*i-(14-j))=BLOCKMEANMATE(i,j)^2;
      squB(1,14*i-(14-j))=B(i,j)^2;
      squT(1,14*i-(14-j))=T(i,j)^2;
      squR(1,14*i-(14-j))=R(i,j)^2;
      squBP(1,14*i-(14-j))=BP(i,j)^2;
      squTP(1,14*i-(14-j))=TP(i,j)^2;
      squRP(1,14*i-(14-j))=RP(i,j)^2;
      squBE(1,14*i-(14-j))=BE(i,j)^2;
      squTE(1,14*i-(14-j))=TE(i,j)^2;
      squRE(1,14*i-(14-j))=RE(i,j)^2;
      squT1(1,14*i-(14-j))=T1(i,j)^2;
      squT2(1,14*i-(14-j))=T2(i,j)^2;
      end;
   end;

   %Construct vectors of matrices

   for i=1:40
   for j=1:14
      linOBSMAT(1,14*i-(14-j))=OBSMAT(i,j);
      linOBSMATP(1,14*i-(14-j))=OBSMATP(i,j);
      linOBSMATE(1,14*i-(14-j))=OBSMATE(i,j);
      linGRANDAV(1,14*i-(14-j))=GRANDAV(i,j);
      linGRANDAVP(1,14*i-(14-j))=GRANDAVP(i,j);
      linGRANDAVE(1,14*i-(14-j))=GRANDAVE(i,j);
      linTREMEANMAT(1,14*i-(14-j))=TREMEANMAT(i,j);
      linTREMEANMATP(1,14*i-(14-j))=TREMEANMATP(i,j);
      linTREMEANMATE(1,14*i-(14-j))=TREMEANMATE(i,j);
      linBLOCKMEANMAT(1,14*i-(14-j))=BLOCKMEANMAT(i,j);
      linBLOCKMEANMATP(1,14*i-(14-j))=BLOCKMEANMATP(i,j);
      linBLOCKMEANMATE(1,14*i-(14-j))=BLOCKMEANMATE(i,j);
      linB(1,14*i-(14-j))=B(i,j);
      linT(1,14*i-(14-j))=T(i,j);
      linR(1,14*i-(14-j))=R(i,j);
      linBP(1,14*i-(14-j))=BP(i,j);
      linTP(1,14*i-(14-j))=TP(i,j);
      linRP(1,14*i-(14-j))=RP(i,j);
      linBE(1,14*i-(14-j))=BE(i,j);
      linTE(1,14*i-(14-j))=TE(i,j);
      linRE(1,14*i-(14-j))=RE(i,j);
      linT1(1,14*i-(14-j))=T1(i,j);
      linBLOCKEXVAL(1,14*i-(14-j))=BLOCKEXVAL(i,j);
      linPOSVEC(1,14*i-(14-j))=POSVEC(i,j);
      linPOSVECL(1,14*i-(14-j))=POSVECL(i,j);
      linPOSVECS(1,14*i-(14-j))=POSVECS(i,j);
      linTIMEVEC(1,14*i-(14-j))=TIMEVEC(i,j);
      end;
   end;


% Analysis where separate runs in RIE were not blocked but considered
treatments

  STREAT=sum(squT1)/546; % Within treatment sum of squares
  SBTREAT=sum(squT)/13;  % Between treatment sum of squares
```

```
  RSSB=SBTREAT/STREAT;  % Ratio of above, ratio is 146, so clearly, by F
test, the process was not repeatable
                        %to within the range of individual feature
etches, i.e. the variation of the runs over
                        %shadows the variation between features within
the runs.
  SBTREATP=sum(squTP)/13;
  SBTREATE=sum(squTE)/13;

% Analysis where seperate features are not blocked but considered
treatments

STREAT1=sum(squT2)/520;
SBTREAT1=sum(squB)/39;
RSSB1=SBTREAT1/STREAT1; %This equals .5193, which, by F test, says that
the variations of the
                       % Individual features are not significantly
different than the variation from run to run.

% Analysis where separate runs in RIE were blocked and each feature
selectivity is considered
% a treatment
  SBLOCK=sum(squB)/39; %Block deviation from grand average sum of
squares
  SRES=sum(squR)/507;  %Block residuals sum of squares
  RBR=SBLOCK/SRES;      %Ratio of Block deviations sos to Block residual
sos
  RTR=SBTREAT/SRES;     %Ratio of Treatment deviations sos to Block
residual sos
                        %RBR (treatment(feature/res) ratio is 2.67, RTR
(block(run)/res) ratio is 174.. by F test both discredit the hypothesis
                        %That residual error is more important than the
block and treatment errors, especially the block.
                        % Both the treatment variance and and block
variance overshadow the residual error, and the block
                        %variance massively overshadowing the treatment
variance.  Discounting block error, it may be productive
                        %to locate a functional relationship between
selectivity and feature etch depth.

  %  Write vectors to files for purpose of graphing, etc.

  %cd('C:\Users\Arthur\dissertation\statsdata')

  %fid = fopen('sqobs.txt', 'w');  %Array of Squares for Observed
Selectivity Values
  %fprintf(fid,'%5.4f\n',squOBSMAT);
  %fclose(fid);
  %fid = fopen('sqobsp.txt', 'w'); %Array of Squares for Observed
Photolith Values
  %fprintf(fid,'%5.4f\n',squOBSMATP);
  %fclose(fid);
  %fid = fopen('sqobse.txt', 'w');  %Array of Squares for Observed Etch
Values
  %fprintf(fid,'%5.4f\n',squOBSMATE);
  %fclose(fid);
```

```
  %fid = fopen('sqgrav.txt', 'w');  %Array of Squares for Grand Average
Selectivity Values
  %fprintf(fid,'%5.4f\n',squGRANDAV);
  %fclose(fid);
  %fid = fopen('sqgravp.txt', 'w'); %Array of Squares for Grand Average
Photolith Values
  %fprintf(fid,'%5.4f\n',squGRANDAVP);
  %fclose(fid);
  %fid = fopen('sqgrave.txt', 'w');  %Array of Squares for Grand Average
Etch Values
  %fprintf(fid,'%5.4f\n',squGRANDAVE);
  %fclose(fid);
  %fid = fopen('sqtr.txt', 'w'); %Array of Squares for Treatment mean
selectivity Values
  %fprintf(fid,'%5.4f\n',squTREMEANMAT);
  %fclose(fid);
  %fid = fopen('sqtrp.txt', 'w'); %Array of Squares for Treatment mean
photolith Values
  %fprintf(fid,'%5.4f\n',squTREMEANMATP);
  %fclose(fid);
  %fid = fopen('sqtre.txt', 'w'); %Array of Squares for Treatment mean
Etch Values
  %fprintf(fid,'%5.4f\n',squTREMEANMATE);
  %fclose(fid);
  %fid = fopen('sqb.txt', 'w'); %Array of Squares for Block mean
selectivity Values
  %fprintf(fid,'%5.4f\n',squBLOCKMEANMAT);
  %fclose(fid);
  %fid = fopen('sqbp.txt', 'w'); %Array of Squares for Block mean
photolith Values
  %fprintf(fid,'%5.4f\n',squBLOCKMEANMATP);
  %fclose(fid);
  %fid = fopen('sqbe.txt', 'w'); %Array of Squares for Block mean Etch
Values
  %fprintf(fid,'%5.4f\n',squBLOCKMEANMATE);
  %fclose(fid);
  %fid = fopen('sqbB.txt', 'w'); %Array of Squares for Block mean minus
Grand Average selectivity Values
  %fprintf(fid,'%5.4f\n',squB);
  %fclose(fid);
  %fid = fopen('sqT.txt', 'w'); %Array of Squares for Treatment mean
minus Grand Average selectivity Values
  %fprintf(fid,'%5.4f\n',squT);
  %fclose(fid);
  %fid = fopen('sqR.txt', 'w'); %Array of Squares for Total Residual
selectivity Values (Block technique)
  %fprintf(fid,'%5.4f\n',squR);
  %fclose(fid);
  %fid = fopen('sqbBP.txt', 'w'); %Array of Squares for Block mean minus
Grand Average Photolith Values
  %fprintf(fid,'%5.4f\n',squBP);
  %fclose(fid);
  %fid = fopen('sqTP.txt', 'w'); %Array of Squares for Treatment mean
minus Grand Average Photolith Values
  %fprintf(fid,'%5.4f\n',squTP);
  %fclose(fid);
```

```
  %fid = fopen('sqRP.txt', 'w'); %Array of Squares for Total Residual
Photolith Values (Block technique)
  %fprintf(fid,'%5.4f\n',squRP);
  %fclose(fid);
  %fid = fopen('sqbBE.txt', 'w'); %Array of Squares for Block mean minus
Grand Average Etch Values
  %fprintf(fid,'%5.4f\n',squBE);
  %fclose(fid);
  %fid = fopen('sqTE.txt', 'w'); %Array of Squares for Treatment mean
minus Grand Average Etch Values
  %fprintf(fid,'%5.4f\n',squTE);
  %fclose(fid);
  %fid = fopen('sqRE.txt', 'w'); %Array of Squares for Total Residual
Etch Values (Block technique)
  %fprintf(fid,'%5.4f\n',squRE);
  %fclose(fid);

  %fid = fopen('lobs.txt', 'w');  % Linear Array of Observed Selectivity
Values
  %fprintf(fid,'%5.4f\n',linOBSMAT);
  %fclose(fid);
  %fid = fopen('lobsp.txt', 'w'); %Linear Array of Observed Photolith
Values
  %fprintf(fid,'%5.4f\n',linOBSMATP);
  %fclose(fid);
  %fid = fopen('lobse.txt', 'w');  %Linear Array of Observed Etch Values
  %fprintf(fid,'%5.4f\n',linOBSMATE);
  %fclose(fid);
  %fid = fopen('lgrav.txt', 'w');  %Linear Array of Grand Average
Selectivity Values
  %fprintf(fid,'%5.4f\n',linGRANDAV);
  %fclose(fid);
  %fid = fopen('lgravp.txt', 'w'); %Linear Array of Grand Average
Photolith Values
  %fprintf(fid,'%5.4f\n',linGRANDAVP);
  %fclose(fid);
  %fid = fopen('lgrave.txt', 'w');  %Linear Array of Grand Average Etch
Values
  %fprintf(fid,'%5.4f\n',linGRANDAVE);
  %fclose(fid);
  %fid = fopen('ltr.txt', 'w'); %Linear Array of Treatment mean
selectivity Values
  %fprintf(fid,'%5.4f\n',linTREMEANMAT);
  %fclose(fid);
  %fid = fopen('ltrp.txt', 'w'); %Linear Array of Treatment mean
photolith Values
  %fprintf(fid,'%5.4f\n',linTREMEANMATP);
  %fclose(fid);
  %fid = fopen('ltre.txt', 'w'); %Linear Array of Treatment mean Etch
Values
  %fprintf(fid,'%5.4f\n',linTREMEANMATE);
  %fclose(fid);
  %fid = fopen('lb.txt', 'w'); %Linear Array of Block mean selectivity
Values
  %fprintf(fid,'%5.4f\n',linBLOCKMEANMAT);
  %fclose(fid);
```

```
  %fid = fopen('lbp.txt', 'w'); %Linear Array of Block mean photolith
Values
  %fprintf(fid,'%5.4f\n',linBLOCKMEANMATP);
  %fclose(fid);
  %fid = fopen('lbe.txt', 'w'); %Linear Array of Block mean Etch Values
  %fprintf(fid,'%5.4f\n',linBLOCKMEANMATE);
  %fclose(fid);
  %fid = fopen('lbB.txt', 'w'); %Linear Array of Block mean minus Grand
Average selectivity Values
  %fprintf(fid,'%5.4f\n',linB);
  %fclose(fid);
  %fid = fopen('lT.txt', 'w'); %Linear Array of Treatment mean minus
Grand Average selectivity Values
  %fprintf(fid,'%5.4f\n',linT);
  %fclose(fid);
  %fid = fopen('lR.txt', 'w'); %Linear Array of Total Residual
selectivity Values (Block technique)
  %fprintf(fid,'%5.4f\n',linR);
  %fclose(fid);
  %fid = fopen('lbBP.txt', 'w'); %Linear Array of Block mean minus Grand
Average Photolith Values
  %fprintf(fid,'%5.4f\n',linBP);
  %fclose(fid);
  %fid = fopen('lTP.txt', 'w'); %Linear Array of Treatment mean minus
Grand Average Photolith Values
  %fprintf(fid,'%5.4f\n',linTP);
  %fclose(fid);
  %fid = fopen('lRP.txt', 'w'); %Linear Array of Total Residual
Photolith Values (Block technique)
  %fprintf(fid,'%5.4f\n',linRP);
  %fclose(fid);
  %fid = fopen('lbBE.txt', 'w'); %Linear Array of Block mean minus Grand
Average Etch Values
  %fprintf(fid,'%5.4f\n',linBE);
  %fclose(fid);
  %fid = fopen('lTE.txt', 'w'); %Linear Array of Treatment mean minus
Grand Average Etch Values
  %fprintf(fid,'%5.4f\n',linTE);
  %fclose(fid);
  %fid = fopen('lRE.txt', 'w'); %Linear Array of Total Residual Etch
Values (Block technique)
  %fprintf(fid,'%5.4f\n',linRE);
  %fclose(fid);
  %fid = fopen('Tone.txt', 'w'); %Linear Array of Between Treatment
Residual Etch Values (Non-Block technique)
  %fprintf(fid,'%5.4f\n',linT1);
  %fclose(fid);
  %fid = fopen('Bval.txt', 'w'); %Linear Array of Total Residual Etch
Values (Non-Block technique)
  %fprintf(fid,'%5.4f\n',linBLOCKEXVAL);
  %fclose(fid);
  %fid = fopen('Bmn.txt', 'w'); %Linear Array of Block average
selectivity values
  %fprintf(fid,'%5.4f\n',BLOCKMEAN);
  %fclose(fid);
  %fid = fopen('Bmne.txt', 'w'); %Linear Array of Block average Etch
Values
```

```
  %fprintf(fid,'%5.4f\n',BLOCKMEANE);
  %fclose(fid);
  %fid = fopen('Tonea.txt', 'w'); % Random Within Treatment Residuals
  %fprintf(fid,'%5.4f\n',linT1A);
  %fclose(fid);
  %fid = fopen('Psvec.txt', 'w'); %Linear Array Substrate Position (1-
40) Values
  %fprintf(fid,'%5.4f\n',linPOSVEC);
  %fclose(fid);
  %fid = fopen('Psvecl.txt', 'w'); %Linear Array Substrate Position (1-
12) Values
  %fprintf(fid,'%5.4f\n',linPOSVECL);
  %fclose(fid);
  %fid = fopen('Psvecs.txt', 'w'); %Linear Array Substrate Position (1-
4) Values
  %fprintf(fid,'%5.4f\n',linPOSVECS);
  %fclose(fid);
  %fid = fopen('Tmvec.txt', 'w'); %Linear Array Substrate Position (1-4)
Values
  %fprintf(fid,'%5.4f\n',linTIMEVEC);
  %fclose(fid);
```

REFERENCES

[1] G. P. Nordin and P.C. Deguzman, "Broadband form birefringent quarter-wave plate for the mid-infrared wavelength region," Optics Express, Vol. **5**, No. 8, 163-168 (1999).

[2] G.P. Nordin, J.T. Meier, P.C. Deguzman, and M.W. Jones, "Diffractive optical element for Stokes vector measurement with a focal plane array," SPIE Annual Meeting, 1999.

[3] G.P. Nordin, J.T.Meier, P.C. Deguzman, and M.W. Jones, "Micropolarizer array for infrared imaging polarimetry," J. Opt. Soc. Am., **16**, 1168-1174 (1999).

[4] K.S. Yee, "Numerical solution of initial boundary value problems involving Maxwell's equations in isotropic media," IEEE Trans. Antennas Propagat., **AP-14**, 302-307 (1966).

[5] A. Taflove, *Computational Electrodynamics, The Finite-Difference Time-Domain Method*, (Artech House, Norwood, 1995).

[6] W.F. Ames, *Numerical Methods for Partial Differential Equations*, 2nd Edition, (Academic Press, New York, 1977).

[7] A. Taflove and M.E. Brodwin, "Numerical solution of steady-state electromagnetic scattering problems use the time-dependent Maxwell's equations," IEEE Trans. Microwave Theory and Techniques, **23**, 623-630, (1975).

[8] G. Mur, "Absorbing boundary conditions for the finite-difference approximation of the time-domain electromagnetic field equations," IEEE Trans. Electromagnetic Compatibility, **23**, 377-382 (1981).

[9] M.A. Jensen and G.P. Nordin, "Finite-aperture wire grid polarizers," J. Opt. Soc. Am. A., **17**, No. 12, 2191-2198 (2000).

[10] B.A. Barbour, H.B.Barnes, C.P.Lewis, P.E.A. Lindquist, M.W. Jones, and N. Mohon, "Imaging polarimetry: Applications for generating images where contrast is small," Opt. & Photonics News, 44-48, Aug. 1998.

[11] S.D. Mellin and G.P. Nordin, "Limits of scalar diffraction theory and an iterative angular spectrum algorithm for finite aperture diffractive optical element design," Draft (2000).

[12] D. Prather, M. Mirotznik, and J. Mait, "Boundary integral methods applied to the analysis of diffractive optical elements," J. Opt. Soc. Am. A., **14**, No. 1, 34-43 (1997).

[13] D. Prather, M. Mirotznik, and J. Mait, "Boundary element method for vector modelling diffractive optical elements," SPIE, **2404**, 28-39 (1996).

[14] T.J. Suleski, B. Bagget,, W.F. Delaney, and A.D. Kathman, "Emerging fabrication methods for diffractive optical elements," SPIE Conference on Diffractive and Holographic Technologies, Systems, and Spatial Light Modulators VI, San Jose, 1999.

[15] D.W. Prather, D. Pustai, and S. Shi, "Performance of multilevel diffractive lenses as a function of f-number," Appl. Opt., **40**, No. 2, 207-210 (2001).

[16] G.T.Borek and D.R. Brown, "High performance diffractive optics for beam shaping," SPIE Conference on Diffractive and Holographic Technologies, Systems, and Spatial Light Modulators VI, San Jose, 1999.

[17] W. Daschner, P. Long, R. Stein, C. Wu, and S.H. Lee, "Cost-effective mass fabrication of multilevel diffractive optical elements by use of a single optical exposure with a grayscale mask on high-energy beam-sensitive glass," Appl. Opt., **36**, No. 20, 4675-4680 (1997).

[18] C. Gimkiewicz, D. Hagedorn, J. Jahns, E-B. Kley, and F. Thoma, "Fabrication of microprisms for planar optical interconnections by use of analog gray-scale lithography with high-energy-beam-sensitive glass," Appl. Opt., **38**, No. 14, 2986-2990 (1999).

[19] E-B. Kley, F. Thoma, U.D. Zeitner, L. Wittig, and H. Aagedal, "Fabrication of micro optical surface profiles by using gray scale masks," SPIE, **3276**, 254-262 (1997).

[20] D.M. Brown, D.R. Brown, and J.D. Brown, "High performance analog profile diffractive elements," SPIE Conference on Diffractive and Holographic Technologies, Systems, and Spatial Light Modulators VI, San Jose, 1999.

[21] "HEBS-glass photomask blanks, user's manual," Canyon Materials, Inc., (1996).

[22] E.-B. Kley, M. Cumme, and L. Wittig, "Adapting existing e-beam writers to write HEBS-glass gray scale masks," SPIE Conference on Diffractive and Holographic Technologies, Systems, and Spatial Light Modulators VI, San Jose, 1999.

[23] Y. Oppliger, P. Sixt, J.M. Stauffer, J.M. Mayor, P. Regnault, and G. Voirin, "One-step 3D shaping using a gray-tone mask for optical and microelectronic applications," Microelectronic Engineering, **23**, 449-454 (1994).

[24] W. Daschner, P. Long, M. Larsson, and S.H. Lee, "Fabrication of diffractive optical elements using a single optical exposure with a gray level mask," J. Vac. Sci. Technol. B, **13**, No. 6, 2729-2731 (1995).

[25] W. Daschner, P. Long, R. Stein, C. Wu, and S.H. Lee, "General aspheric refractive micro-optics fabricated by optical lithography using a high energy beam sensitive glass gray-level mask," J. Vac. Sci. Technol. B, **14**, No. 6, 3730-3733 (1996).

[26] V.P. Korolkov, A.I. Malyshev, V.G. Nikitin, A.G. Poleshchuk, A.A. Kharissov, V.V. Cherkashin, and C. Wu, "Application of gray-scale LDW glass masks for fabrication of high-efficiency DOEs," SPIE Conference on Diffractive and Holographic Technologies, Systems, and Spatial Light Modulators VI, San Jose, 1999.

[27] K. Reimer, U. Hofmann, M. Jurss, W. Pilz, H.J. Quenzer, and B. Wagner, "Fabrication of microrelief surfaces using a one-step lithography process," SPIE, **3226**, 1996.

[28] A. Schilling, P. Nussbaum, C. Ossmann, S. Traut, M. Rossi, H. Schift, and H.P. Herzig, "Miniaturized, focusing fan-out elements, design, fabrication and characterization," J. Opt. A, **1**, No. 2, 244-248 (1999).

[29] R. W. Gerchberg and W. O. Saxton, "A practical algorithm for the determination of phase from image and diffraction plane picutures," Optik., **35**, No. 2, 237-246 (1971).

[30] F. Wyrowski, "Iterative Fourier-transform algorithm applied to computer holography," J. Opt. Soc. Am. A, **5**, 1058-1065 (1988).

[31] D.A. Pommet, M.G. Moharam, and E.B. Grann, "Limits of scalar diffraction theory for diffractive phase elements," Optics Letters, **11**, No.6, 1827-1834 (1995).

[32] J. N. Mait, "Understanding diffractive optic design in the scalar domain," J. Opt. Soc. Am. A, **12**, 2145-2158 (1995).

[33] M. Mirotznik, D. Prather, and J.N. Mait, "A hybrid finite element-boundary element method for the analysis of diffractive elements," J. Mod. Optics., **43**, No. 7, 1309-1321 (1996).

[34] M.V. Klein and T.E. Furtak, *Optics*, (John Wiley and Sons, New York, 1986).

[35] M. Born and E. Wolf, *Principles of Optics*, (Pergamon Press Ltd., Oxford, 1964).

[36] J.D. Jackson, *Classical Electrodynamics*, (John Wiley and Sons, New York, 1975).

[37] C.A. Balanis, *Advanced Engineering Electromagnetics*, (John Wiley and Sons, New York, 1989).

[38] D.W. Prather, Analysis and synthesis of finite aperiodic diffractive optical elements using rigorous electromagnetic models, (Ph.D. dissertation, University of Maryland, 1997).

[39] S.D. Mellin, Design and analysis of finite aperture diffractive optical elements, (Ph.D. dissertation, University of Alabama in Huntsville, 2001).

[40] J.W. Goodman, *Introduction to Fourier Optics*, (McGraw-Hill, Inc., New York, 1968).

[41] S.D. Mellin, "Derivation of the Fresnel approximation from the angular spectrum approach," (Personal notes, 2001).

[42] V.A. Yunkin, D. Fischer, and E. Voges, "Highly anisotropic selective reactive ion etching of deep trenches in silicon," Microelectronic Engineering, **23**, 373-376 (1994).

[43] R.D. Mansano, P. Verdonck, and H.S. Maciel, "Deep trench etching in silicon with fluorine containing plasmas," Appl. Surface Sci., **100**/**101**, 583-586 (1996).

[44] F.L. Pedrotti and L.S. Pedrotti, *Introduction to Optics*, (Prentice-Hall, Inc., New Jersey, 1987).

[45] H. Jansen, M. de Boer, R. Legtenberg, and M. Elwenspoek, "The black silicon method: A universal method for determining the parameter setting of a fluorine-based reactive ion etcher in deep silicon trench etching with profile control," Proc. Micro Mechanics, Pisa, 1994.

[46] H. Jansen, M. de Boer, R. Legtenberg, and M. Elwenspoek, "The black silicon method II: The effect of mask material and loading on the reactive ion etching of deep silicon trenches," Microelectronic Engineering, **27**, 475-480 (1995).

[47] G.E.P. Box, W.G. Hunter, and J.S. Hunter, *Statistics for Experimenters*, (John Wiley and Sons, New York, 1978).

[48] P.T. Strait, *Probability and Statistics with Applications*, (Harcourt Brace Jovanovich, Inc., New York, 1983).